EXTREME WIND AND WAVE CONDITIONS IN TROPICAL CYCLONES OBSERVED FROM SYNTHETIC APERTURE RADAR IMAGES

Dissertation

zur Erlangung des Doktorgrades

der Naturwissenschaften im Fachbereich

Geowissenschaften

der Universität Hamburg

vorgelegt von:

Antonio Reppucci

aus

Napoli, Italien

Hamburg

2012

Als Dissertation angenommen vom Fachbereich Geowissenschaften der Universität Hamburg

Auf Grund der Gutachten von Prof. Hartmut Graßl

und Dr. Susanne Lenher

Tag der mündlichen Prüfung 23.10.2012

Hamburg, Mai 2012

Prof. Dr. Dir Gajewski

Vorsitzender des Fach-Promotionsausschusses

Abstract

Tropical cyclone is a generic term which comprises hurricanes in the Atlantic Ocean and Northeast Pacific Ocean, typhoons in the Northwest Pacific Ocean, and cyclones in the Indian Ocean and Southwest Pacific ocean.

Tropical cyclones account for a significant fraction of damage, injury and loss of life. Current models are still not able to provide robust quantitative forecasts on track and intensity changes, mainly due to the lack of reliable measurements of the initial state conditions. There are still a lot of aspects in the physics of tropical cyclones, which are not well understood. Of particular importance are processes taking place at the air sea interface, which is a key component in the heat flux driving the cyclone. Due to the relatively small amount of in situ data available within cyclones remote sensing techniques play an important role in the retrieval of geophysical information. Because of their all weather capability and wide swath coverage space borne active microwave sensors like the Synthetic Aperture Radar are of particular interest in this context

Several studies have demonstrated that SAR images of the ocean surface contain information on sea state and wind field. Different techniques can be used to retrieve the propagation direction of ocean waves, the surface wind speed and direction to identify and analyze mesoscale surface features.

The study presented hereafter focuses on the use of Synthetic Aperture Radar (SAR) data for the retrieval of the tropical cyclones characteristic parameters. It is part of the EXTROP project (Investigation of Tropical and Extratropical Cyclones using Satellite data), which concentrates also on the study of the evolution of tropical cyclones and on their transition to extratropical cyclones that can affect Europe. Six PhD candidates have been funded by the EXTROP project; two focusing on numerical modeling of cyclones, two investigating the cyclones' characterization using passive remote sensing. The two last PhD topics considered the use of active remote sensing (radar, altimeters) for wind field retrieval; the present work is dedicated to the development of techniques for tropical cyclone analysis using SAR (Synthetic Aperture Radar) data.

The first part of the thesis consists of an overview of the state of the art in the field of tropical cyclone characterization. An extensive bibliographic study has been performed in order to reassess the basic principles of the SAR imaging of sea surfaces and to highlight the advantages and drawbacks of the methodologies and techniques applied for tropical cyclone analysis.

The second part of the thesis is then dedicated to the presentation of the algorithms developed in the framework of the PhD for the retrieval of tropical cyclone intensity, based on the use of SAR image intensity and of numerical model.

A new technique to derive the maximum wind speed and the hurricane strength from SAR images is then proposed. The problem of saturation in tropical cyclone wind regime is overcome basing the technique on the combined use of SAR measurements for areas of wind speed of 20 m/s or less and a parametric model for tropical cyclone wind speed. The radius of maximum wind speed required as input for the model is measured from the SAR image using a technique based on wavelet transform. Wind directions have been computed from the SAR image using spectral analysis to detect the area containing feature associated with the wind flow and an interpolation technique. The procedure has been applied to five images of tropical cyclones showing agreement with in situ measurements. Maximum wind speed up to70 m/s can be determined with an RMS error of 3.9 m/s.

TABLE OF CONTENTS

ABBREVIATIONS AND ACCRONYMS

2D	2-Dimensional
ADC	Analog Digital Converter
ADP	Altimeter Data Processing System
AMI	Active Microwave Instrument
ASAR	Advanced Synthetic Aperture Radar
DFD	German Remote Sensing Data Centre
DLR	Deutsches Zentrum für Luft und Raumfahrt
DN	Digital Number
DSD	Drop Size Distribution
ECMWF	European Centre for Medium-Range Weather Forecast
ENL	Effective (or Equivalent) Number of Looks
ENVISAT	ENVIronment SATellite
ERS	ESA Remote Sensing satellite
ESA	European Space Agency
FFT	Fast Fourier Transform
F-PAF	French Processing and Archiving Facility
GFDL	Geophysical Fluid Dynamics Laboratory
GFZ	GeoForschungsZentrum Potsdam
GMF	Geophysical Model Function
HRD	Hurricane Research Division
IMF	DLR Institute für Methodik der Fernerkundung
JAXA	Japan Aerospace Exploration Agency
JMA	Japan Meteorological Agency
NHC	National Hurricane Centre
NOAA	National Oceanic and Atmospheric Administration
NRCS	Normalized Radar Cross Section
NWP	Numerical Weather Prediction
RADARSAT	RADAR SATellite
RMS	Root Mean Squared
RSMC	Regional Specialized Meteorological Centre
SAR	Synthetic Aperture Radar
TCWC	Tropical Cyclone Warning Centre
TRMM	Tropical Rainfall Measuring Mission
TUTT	Tropical Upper Tropospheric Troughs
UTC	Coordinated Universal Time
UWA	SAR wave fast delivery product. Wave spectra
WAM	Wave Analysis Model

LIST OF FIGURES

LIST OF TABLES

1 Introduction

1.1 State of the art

Tropical cyclone is a generic term that designs an intense storm characterized by a large low pressure centre and numerous thunderstorms. Depending on the ocean basin where they develop, they are named differently. In the Northern Atlantic and Northeast Pacific Ocean tropical cyclones are called Hurricanes after the Caribe god of evil, 'Hurican'. In the Northwest Pacific Ocean the term "Typhoon" from the Cantonese 'strong wind' is employed and in the Indian Ocean and Southwest Pacific Ocean they are called Cyclones.

Whatever the regions they affect tropical cyclones are among the most destructive of natural disasters. Due to the population growth and economic infrastructure of coastal areas these storms are causing increasing amounts of material damages. Most deaths are flood-related. Torrential rains from decaying hurricanes and tropical storms can produce extensive urban and river flooding. In addition, hurricanes can spawn tornadoes, which add to the destructiveness of the storm.

A mean of fifty tropical cyclones develop each year in the tropical area worldwide [Emanuel, 1991]. Moreover Strong North Atlantic storms, which often have their origin in tropical cyclones, lead to high impact weather events in Northern and Western Europe. Extra-tropical cyclones lash Europe in winter with surface winds that can gust at 80-100 mph. Examples include the Burns' Day Storm of 1990 and the 1997 Christmas Eve storm. The total insured loss from this type of storm in Europe is estimated to have been 24 billion Euros between 1985 and 2001. Although such storms are more common in winter, they can occur in summer - one coincided with the Fastnet yacht race on 14 August 1979, during which there were several fatalities.

Accurate forecast of intensity and track of tropical cyclones are of paramount importance for reducing vulnerability to storm landfall. It is in this context that the project EXTROP "Investigation of extratropical cyclones using passive and active microwave radars" was defined. Research activities, directly funded by the project, have as objective to improve the understanding and the predictability of North Atlantic cyclones. The topic of the present PhD, which focuses on the analysis of tropical cyclones using wide-swath SAR images, was defined in this framework.

Because tropical cyclones are compact long-lived weather systems, forecasts of their positions and intensities, measured in terms of maximum wind, are the first steps toward characterizing the threat. Reliable estimation of storm intensity depends almost entirely on in situ aircraft measurements and, for the last 30 years, on satellite-based techniques. Airborne reconnaissance missions were undertaken in the western North Pacific and North Atlantic regions around 1945. For the first decade or so of airborne reconnaissance, surface winds were estimated mostly by visual inspection of the sea surface. These missions continue in the North Atlantic region, but were stopped in the western North Pacific in 1987.

Techniques for estimating tropical cyclone intensity from satellite imagery and other satellite-based measurements were developed during the 1970s. In both western North Pacific and North Atlantic regions, these techniques were refined and calibrated against aircraft measurements. Today they constitute the primary means of estimating peak surface winds in all locations except the North Atlantic, where they are supplemented by reconnaissance aircraft measurements.

Currently different sensors and observational platforms are used to monitor the ocean and atmosphere around a tropical cyclone. This information, obtained by buoys, ground based radars, reconnaissance aircrafts and satellites is used together to prepare forecasts and issue warnings, and their quality and quantity is of particular importance for the skinless of the final results.

Satellite observations take a central role in the monitoring of tropical cyclones especially in area where aircraft observations are not routinely available. Remotely sensed data from satellite platform are in particular used to directly monitor position and intensity of the storms, rainfall-rate and inner-core structure analysis. Moreover these data are assimilated into numerical forecast models to obtain more accurate estimates of the initial values for the model state variables.

The most popular technique, used operationally for more than thirty years as method of monitoring tropical systems is the Dvorak Technique [Olander and Velden, 2007]. This technique is based on image pattern recognition and empirically-based rules to derive an estimate of tropical cyclone intensity using enhanced infrared and/or visible satellite imagery. The subjectivity of the Dvorak technique is well documented. Its main drawback is that the precision of the analysis and the accuracy of the cyclone intensity estimation largely depend on the skill and experience level of the satellite analyst.

Others methods are based on passive microwave data and their ability to detect changes in tropospheric warm core structure of the tropical cyclone that is related to changes of the minimum sea level pressure and so to the storm intensity. These methods are still not operational and the accuracy is of about 10 m/s [Kidder et al., 2000].

The use of SAR images gives the opportunity to obtain a high resolution wind field to be used in all the applications where the knowledge of the fine scale structure of the wind is required, e.g. wind farm optimal siting, coastal monitoring, near coastal wind field, high vulnerability.

The retrieval of high resolution wind speed map from SAR images is a well-established technique [Lehner et al., 1998] [Horstmann et al., 2003] [Monaldo et al., 2000]. In particular under tropical cyclone conditions, where numerical modelling and forecasting of ocean wind fields is still a challenge, SAR data can be used to improve the existing numerical model using assimilation techniques [Horstmann et al., 2005],[Morey et al., 2005],[Perrie et al., 2008]. Using a technique based on the inversion of a geophysical model function (GMF), SAR wind fields are retrieved in two steps. In the first step wind directions are retrieved, which are a necessary input in the second step to retrieve wind speeds.

1.2 Organization of the study

The present report is composed of two parts.

The first part is dedicated to the synthesis of the extensive bibliographic study in the domain of the tropical cyclone characterization. The basic SAR imaging mechanism and the main processing steps are reviewed in chapter two, where also the theory of the SAR imaging of ocean surfaces and wave imaging mechanisms is described.

Tropical cyclone characterization and numerical modelling techniques are investigated in the third chapter. The parametric model of Holland that has been used during the PhD for the retrieval of wind field in tropical cyclones is presented. Due to its analytical character it could be optimized and

used together with SAR wind field measurements, thereby improving the wind field in areas where the SAR measurements saturate.

Finally, the different techniques classically used for the retrieval of wind field based on SAR image analyses are reviewed in the chapter four. Different algorithms used for the wind field retrieval under tropical cyclone conditions, are presented. Advantages and drawbacks of each method are highlighted and analysed in order to stress the need for improving the existing models, especially in case of tropical cyclones where the saturation of the backscattered signal is the principal reason for the underestimation of the actual wind speed.

The second part of the report focuses on the definition and presentation of the algorithms developed during the PhD for the retrieval of tropical cyclone intensity, based on the use of SAR image intensity and of a numerical model.

In the fifth chapter the SAR datasets used for the study are described. Details on ENVISAT ASAR Wide Swath mode (ScanSAR), RADARSAT Wide Swath mode and ERS-2 Wave mode images are presented. Then a description of ERS-2 Scatterometer and altimeter data, used to validate and compare to SAR measurements, is given. The performances and limitations of each data used are assessed.

The sixth chapter presents an analysis of the features that is possible to extract from SAR images of tropical cyclones. In particular a technique based on wavelet analysis for the extraction of the storm's eye size and shape is detailed. The methodology is applied for the first time to ENVISAT ASAR Wide Swath images.

The seventh chapter presents the modelling and development of a new technique for the estimation of tropical cyclone intensity. The methodology is based on the use of SAR measurements together with the Holland numerical model. In addition the effect of heavy rain on radar backscatter and on the retrieved wind field is investigated theoretically.

Finally in the eighth chapter an analysis of tropical cyclone using a unique dataset of ERS wave mode data is presented. The study proves that the data, acquired globally over the ocean can be used for tracking tropical cyclone in the open ocean or in areas where no aircraft or buoy measurements are available.

Conclusion and outlooks are given at the end of the report.

1.3 References

Olander T. L. and Velden C. S., 2007, The Advanced Dvorak Technique: Continued Development of an Objective Scheme to Estimate Tropical Cyclone Intensity Using Geostationary Infrared Satellite Imagery. *Weather and Forecasting*, vol. 22, no 2.

Kidder S. Q., Goldberg M. D., Zehr R. M., DeMaria M., Purdom J.F.W., Velden C. S., Grody N.C. and Kusselson S. J., 2000, Satellite analysis of tropical cyclones using the advanced microwave sounding unit (AMSU), *Bull. Amer Meteor Soc*., 81, pp 1241-1259.

Lehner S., Horstmann J., Koch, W., and Rosenthal W., 1998, Mesoscale wind measurements using recalibrated ERS SAR images. *Journal of Geophys. Res*.-Oceans, no.103, pp.7847−7856.

Monaldo, F., 2000, The Alaska SAR demonstration and near-real-time synthetic 910 aperture radar winds. *Johns Hopkins Apl Technical Digest*, no.21, pp.75−79.

Horstmann J., Schiller H., Schulz-Stellenfleth J., and Lehner S., 2003, Global wind speed retrieval from SAR. *IEEE Trans. Geosc. Remote Sens*., no. 41(10), pp. 2277–2286.

Horstmann, J., Thompson, D.R., Monaldo, F., Graber, H.C. & Iris, S., 2005, Can Synthetic Aperture Radars be used to Estimate Hurricane Force Winds*? Geophysical Research Letters*, no. 32.

Morey S. L., Bourassa M. A., Davis X. J., O'Brien J. J., and Zavala-Hidalgo J., 2005, Remotely sensed winds for episodic forcing of ocean models. *Journal of Geophys. Res*., no.110 (C10).

Perrie W., He Y., and Shen H., 2006, On Determination of Wind Vectors for C-band SAR for High Wind Speeds. *Proc. SEASAR workshop*, Frascati, Italy.

Perrie, W., W. Zhang, M. Bourassa, H. Shen, and P. W. Vachon, 2008, Impact of satellite winds on marine wind simulations. *Wea. Forecasting*, no. 23, pp. 290–303.

2 SAR principles and techniques

Synthetic aperture radar (SAR) is a coherent imaging instrument based on a combination of high precision electronic hardware for the acquisition of the data and advanced theoretical principles of signal processing to convert the data into images.

In this chapter the basic SAR imaging mechanism and the main processing steps are explained. A particular emphasis is put on the theory of ocean backscattering and wave imaging mechanisms. The introduced techniques and concepts are the basis for understanding different aspects of SAR wind retrievals discussed in the subsequent chapters.

2.1 SAR imaging principles

The objective of radar imaging is to generate a two-dimensional reflectivity map of earth surface in the microwave region of the electromagnetic spectrum. A typical radar imaging sensor consists of a transmitting and receiving antenna mounted on a moving platform and oriented parallel to the flight direction (Fig. 2-1). The antenna emits consecutively electromagnetic pulses of duration τ_p to the ground, which are backscattered from different targets. The time difference Δt between the emission and the reception of the pulse is a function of the distance R between the antenna and the target:

$$\Delta t = \frac{2R}{c} \tag{2.1}$$

where c is the speed of light and the factor 2 accounts for the round-trip propagation. The sensor range resolution, i.e. the minimum spacing between two objects that can be individually detected, is:

$$\Delta r = \frac{c\tau}{2} \approx \frac{c}{2\Delta f} \tag{2.2}$$

where $\Delta f \approx 1/\tau$ is approximately the bandwidth of the pulse.

In order to achieve high resolution in range short pulses are necessary. The reduction of the pulse width leads to a high peak power for a fixed mean power operation. To circumvent this limitation long modulated pulses (chirp) are used instead of short ones. This makes a further processing step (pulse compression) necessary.

In flight or azimuth direction the radar resolution is prescribed by the size of the antenna footprint Δx_{ra}, which is dependent on the distance R between the sensor and the scene and the angular resolution of the antenna:

$$\alpha_{ra} = \frac{\lambda}{L} \tag{2.3}$$

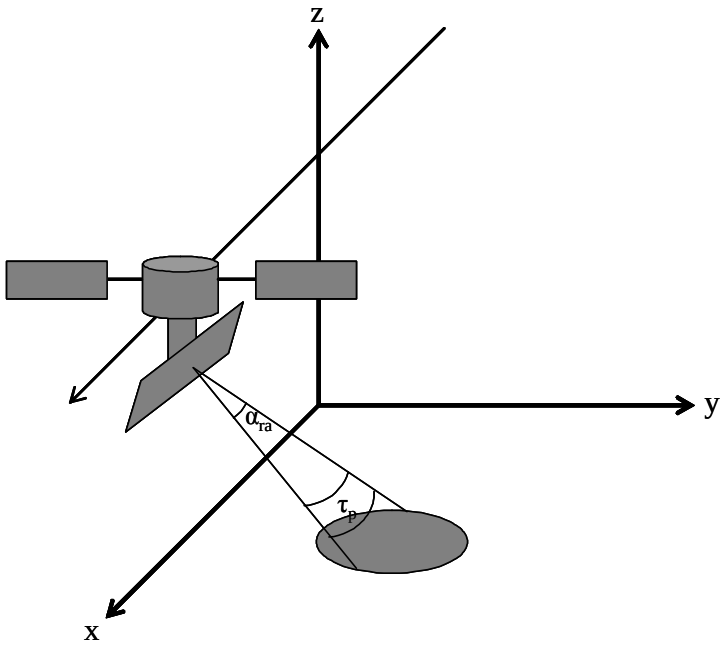

Fig. 2-1: Satellite- SAR acquisition geometry.

where λ is the wavelength of the electromagnetic pulse and L the effective antenna length.

The spatial resolution in azimuth is then given by:

$$\Delta x_{ra} = \alpha_{ra} R = R\frac{\lambda}{L} \tag{2.4}$$

To achieve high resolution in azimuth large antennas or short distances to the scene are required. As an example for the ASAR sensor on board the ENVISAT satellite that orbits at a height of 800 *Km* and has an antenna length of 10 *m* the resolution is approximately 4.5 *Km*. This resolution is too coarse for most applications.

Using a SAR these problems are overcome by implementing the synthetic antenna concept: a very large antenna is synthesized by moving a real one of limited dimension along a reference path. The synthesis is carried out by coherently combining the backscattered echoes received and recorded along the flight path.

The maximum length of the synthesized antenna L_{sa} is equal to the size of the real antenna footprint on the ground at the distance R:

$$L_{sa} = \frac{\lambda}{L} R \tag{2.5}$$

The angular resolution of the synthesized antenna is:

$$\alpha_{sa} = \frac{\lambda}{2L_{sa}} \tag{2.6}$$

The azimuth resolution of the synthetic aperture antenna is:

$$\Delta x_{sa} = \alpha_{sa} R = \frac{L}{2} \tag{2.7}$$

The achieved resolution is therefore completely independent of the range distance and is determined only by the size of the SAR antenna (see appendix A for more details).

2.2 Radar equation and normalized radar cross section

The relationship that links the radar characteristic, the observed target and the received signal is the radar equation:

$$P_r = \frac{P_t G^2 \lambda^2}{(4\pi)^3 R^4} [A_{rs} \chi \chi' G_{ts}] \tag{2.8}$$

where P_t is the power transmitted by the satellite antenna, with wavelength λ, P_r is the power received at the antenna, G is the antenna transmission gain and R is the distance between the antenna and the target.

The terms in the square brackets, associated to the target, are the target effective area A_{rs}, its impedance loss χ, its directivity χ' and the target gain in the antenna direction G_{ts}. Since it is difficult to evaluate each one separately they are expressed as one term, the "*Radar Cross Section*", which describes the extent to which a target reflects an incident electromagnetic wave.

$$\sigma = [A_{rs} \chi \chi' G_{ts}] \tag{2.9}$$

Combining eq. (2.8) and (2.9) we obtain the final form of the radar equation:

$$P_r = \frac{P_t G^2 \lambda^2}{(4\pi)^3 R^4} \sigma \tag{2.10}$$

The radar cross section is normalized by the image pixel area A_p to become the "*Normalized Radar Cross Section*" (NRCS), σ^o, which is given by (2.11) and it is independent of the pixel size in the image data. The units for NRCS are given in a logarithmic scale, the decibel (*dB*):

$$\sigma^o = \frac{\sigma}{A_p} \tag{2.11}$$

Analysis of NRCS of SAR data over ocean leads to investigate with high resolution the condition of ocean surface, which reflects various phenomena occurring at the air sea interface. Fig. 2-2 shows a SAR image acquired on Aug 28 2005 over the Gulf of Mexico by the ASAR sensor on board the ENVISAT satellite. Several features due to different atmospheric phenomena can be observed. On the top of the image the imprint of atmospheric boundary layer rolls is visible as streaky features aligned with the wind direction. In the lower part of the image there are several cellular structures associated with convective clouds and heavy rain, which produces an increase of the backscattering with respect to the background.

2.3 Theory of SAR imaging of sea surface.

Synthetic aperture radar can be used to measure high resolution wind field and ocean wave parameters.

Over the ocean the radar backscatter depends on the sea surface roughness and the radar parameters (e.g. frequency, polarization, incidence angle) [Ulaby et al., 1981].

The surface roughness of the observed area plays an important role in the backscattering of the signal. Fig. 2-3 shows the effect of increasing surface roughness on the SAR signal.

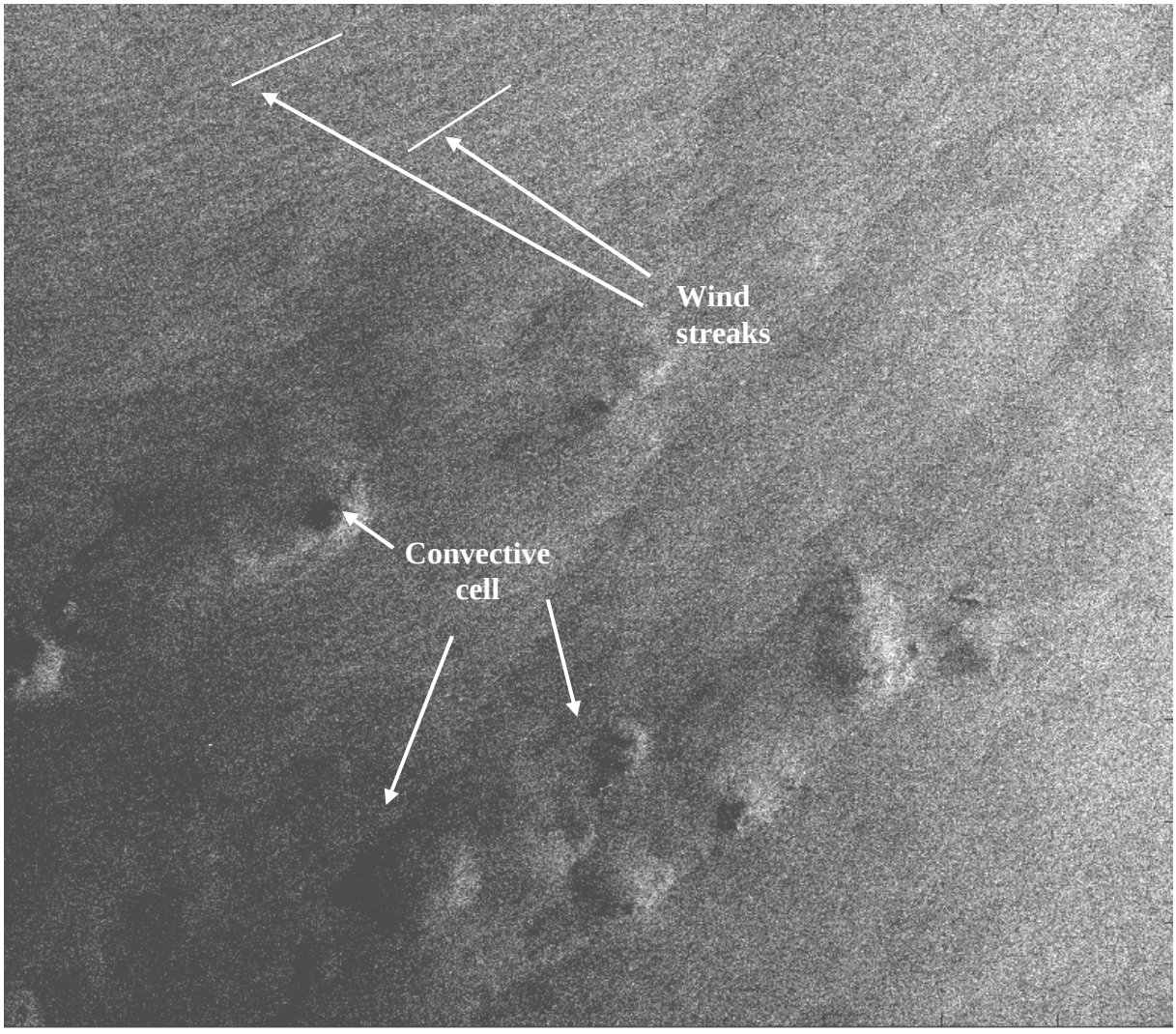

Fig. 2-2: ENVISAT ASAR Wide Swath mode scene acquired on 28-Aug-2005 over the Gulf of Mexico. The SAR image shows the imprints of atmospheric features, such as wind streaks and convective cells.

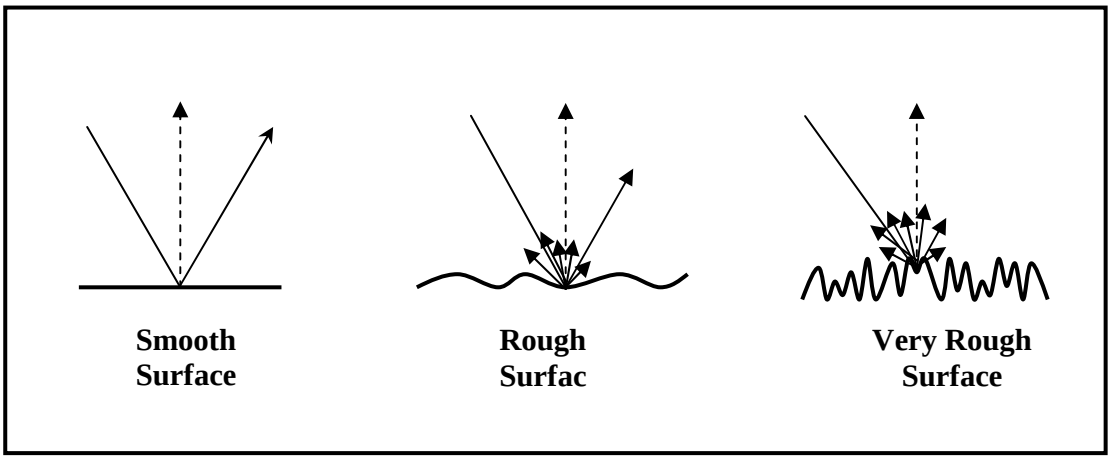

Fig. 2-3: Effect of increasing surface roughness on the radar backscattering

One can observe that increasing the surface roughness leads to an increase of the electromagnetic radiation in the direction of the radar.

The frequency of the electromagnetic wave determines the scale of the roughness detected. In general, the NRCS increases for increasing frequencies. For incidence angles between 20° and 60° the signal in VV polarization is always stronger than the one in HH.

Analysing the behaviour of the NRCS at varying incidence angles three areas can be distinguished (Fig. 2-4) [Robinson, 2004]. In the first area (a), for incidence angles less than 20°, the radar backscattering can be described using a quasi-specular scattering model. For calm sea state the NRCS decreases rapidly with increasing incidence angles. For increasing wind speed the backscattering at nadir becomes weaker and variation according to the incidence angles is less sensible.

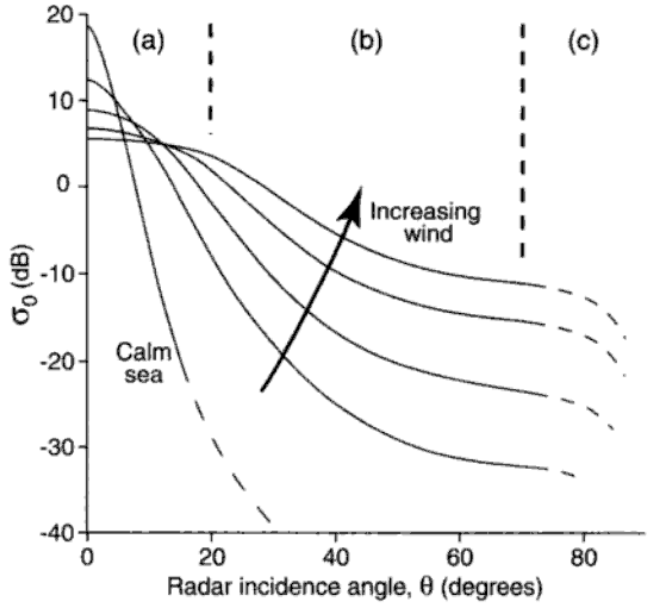

Fig. 2-4: Ocean backscattering for different incidence angles [Robinson, 2004].

In the second area (b), for incidence angles between 20° and 70°, the backscattering is due to a resonance effect (Bragg scattering) between the microwaves and the sea surface roughness. This sea surface roughness is generated by short wavelength waves formed in response to the wind stress. In this area the NRCS decrease less rapidly with increasing incidence angles. For incidence angles larger than 70° (c) the NRCS decreases again rapidly due to a shadowing effect of the long waves.

As aforementioned, over the ocean the backscattering is mainly due to centimetre surface waves (short gravity and capillary waves), which are generated and driven by the wind that blows over the sea surface. SAR NRCS measurements over the ocean can be thus used to infer the wind field. To relate the radar geometry and the NRCS measurements to the surface wind field a geophysical model function (GMF) is used. The NRCS measurement is related to the ocean surface roughness while the retrieved wind field is tuned to the wind at 10 *m* height, because such measurements represent the lowest surface layer in boundary layer models for the fitting and validation of the GMF.

Due to the high resolution at which the measurements are taken, SAR is also able to image the ocean waves. It is thus possible to measure sea state parameters like wavelength and direction, significant wave height or wave period. The SAR imaging mechanism is influenced by the modulation of the NRCS and by the wave motions (i.e., by the orbital velocity and acceleration associated with the long waves) [Alpers et al., 1981].

Due to the SAR imaging mechanism an object that has a velocity component in the radar direction will be shifted and smeared. This will cause, in the case of ocean waves, a distortion of the imaged wave field and a filtering of the high frequency waves. Therefore the integral transform that describes the mapping of ocean weave spectrum into SAR image variance spectrum, also called Modulation Transfer Function, is a non-linear function [Hasselmann and Hasselmann, 1991]. More details on the SAR Modulation Transfer Function are given in appendix A.

2.4 References

Alpers W., Ross D.B. and Rufenach C.L., 1981. On the Detectability of Ocean Surface Waves by Real and Synthetic Aperture Radar. *Journal of Geophys. Res*., vol. 86, pp. 648 1-6498.

Franceschetti G., Lanari R., 1999. Synthetic Aperture Radar Processing. *CRC Press*, Boca Raton, Fla.

Hasselmann K., Raney R.K., Plant W.J., Alpers W., Shuchman R.A., Lyzenga D.R., Rufenach C.L., Tucker M.J., 1985. Theory of Synthetic Aperture Radar Ocean Imaging: A MARSEN View. *Journal of Geophys. Res.*, vol. 90, pp. 4659-4685.

Hasselmann K. and Hasselmann S., 1991. On the nonlinear mapping of an ocean wave spectrum into a Synthetic Aperture Radar image spectrum and its inversion. *Journal of Geophys. Res.*, vol. 96, pp. 1071 3- 10729.

Robinson I. S., 2004. Measuring the Oceans from Space: The principles and methods of satellite oceanography. *Springer*.

Ulaby F.T.; Moore R. K., Fung A.K., 1986. Microwave Remote Sensing: Active and Passive, Volume II: Radar Remote Sensing and Surface Scattering and Emission Theory. *Artech House*.

3 Tropical cyclones: basic physic and modelling approaches.

Tropical cyclone wind and wave fields are of interest both scientifically for understanding wind–wave interaction physics and operationally for predicting potentially hazardous conditions for ship navigation and coastal regions.

The prediction of intensity and track of tropical cyclones, which are characterized by intense and fast varying winds are an issue for the forecast and scientific community. During the past years several model for winds fields and waves during tropical cyclones were developed for weather and storm surge predictions [Ross, 1976], [Brand et al. 1977], [Holland, 1980], [Hsu et al, 2000]. Although improvements in the prediction of tropical cyclone intensity and track have been made the errors are still too large.

As an example, Fig. 3-1 shows a plot of the National Hurricane Centre (NHC) annual average official track errors between the forecast using the CLIPER model [Aberson, 1998] and best track data at the forecast verifying time, for Atlantic basin tropical storms and hurricanes for the period 1970-2007, with least-squares trend lines superimposed.

To improve the monitoring and the forecast several techniques for estimating tropical cyclone intensity from satellite imagery have been developed [Katsaros et al., 2002], [Hawkins et al., 2001], [Quilfen et al. 1998]. Most of these methods are still not operational and the accuracy is about 10 m/s [Kidder et al., 2000].

In this chapter the basics elements of the structure and dynamics of tropical cyclones are introduced together with some models used to forecast intensity and track. Details on some of the numerical models used to compare SAR data are given.

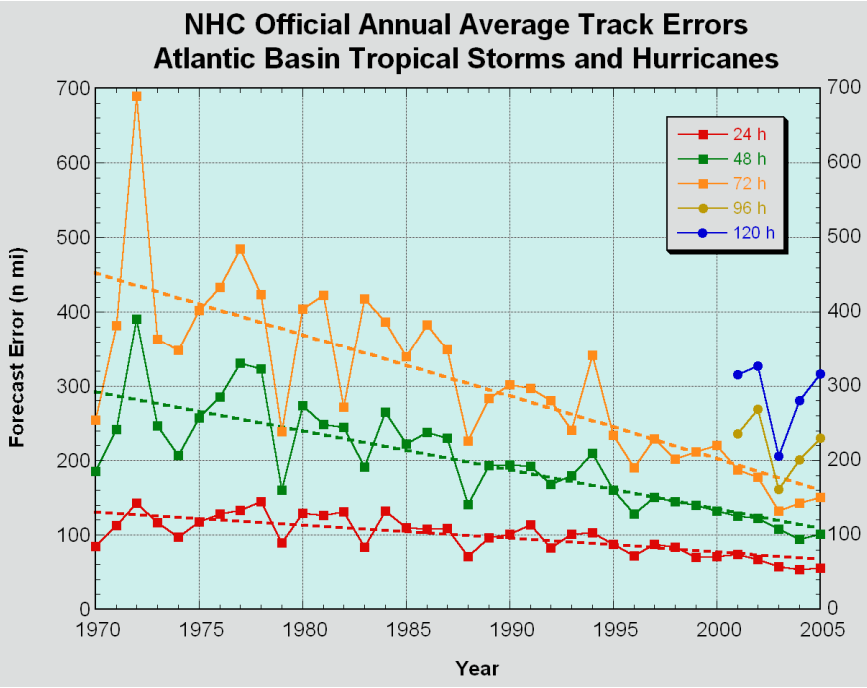

Fig. 3-1: NHC annual average official track errors for Atlantic basin tropical storms and hurricanes for the period 1970-2007, with least-squares trend lines superimposed.

Hurricane Name/Date	Estimated Insured Loss
Katrina/August 2005	43.6bn USD
Andrew/August 1992	22.9bn USD
Wilma/October 2005	10.9bn USD
Ike/September 2008	10.7bn USD
Charley/August 2004	8.2bn USD
Ivan/September 2004	7.8bn USD
Hugo/September 1989	7.0bn USD
Rita/September 2005	6.0bn USD
Frances/September 2004	5.0bn USD
Jeanne/September 2004	4.0bn USD

Tab. 3-1: Ten Costliest Hurricanes to Make Landfall in USA

3.1 Definition and dynamics of tropical cyclones.

Tropical oceans spawn approximately 80 tropical storms annually over all oceans, about two-thirds are catalogued as tropical cyclones [Emanuel, 2003]. Almost 90% of these storms form within 20° north and south of the Equator.

Tropical cyclones account each year for a significant fraction of damage, injury and loss of life. Tab. 3-1 contains the list of the 10 costliest tropical cyclones that affected the U.S. [Insurance Information Institute, 2008] to give an idea of the type of damage that these storm can cause.

By definition a tropical cyclone is a storm system characterized by a large low pressure centre and numerous thunderstorms that produce strong winds and flooding rain. The term ‘tropical’ arises from the geographic location where these storms originate, while the term cyclone refers to their cyclonic nature, with wind rotating in counter-clockwise direction in the northern hemisphere and clockwise in the southern hemisphere.

Tropical cyclone is a generic term for an intense storm which, depending on the ocean basin where it develops, can be called differently. In the Northern Atlantic and Northeast Pacific Ocean they are called Hurricanes after the Caribe god of evil, ‘Hurican’. In the Northwest Pacific Ocean tropical cyclones are termed Typhoon from the Cantonese ‘strong wind’, and in the Indian Ocean and Southwest Pacific Ocean they are called Cyclones.

A tropical cyclone goes through several stages as it develops. It starts as a tropical wave, a westward-moving area of low air pressure. As the warm, moist air over the ocean rises in the low air pressure area, cold air from above is replacing it. This produces strong gusty winds, heavy rain and thunderclouds, a ‘Tropical Disturbance’. As the air pressure drops and there are sustained winds up to 17 *m/s*, the system is called ‘Tropical Depression’. When the cyclonic winds have sustained speeds from 17 to 33 *m/s*, it becomes a ‘Tropical Storm’ (storms are given names when they turn into a Tropical Storm). The storm becomes a Tropical Cyclone when sustained winds above 33 *m/s* occur.

3. Tropical cyclones: basic physics and modelling approaches

Tropical cyclones are ranked according to their maximum wind speed or minimum pressure. In the Northern Atlantic and Northeast Pacific Ocean the Saffir-Simpson scale is used to classify tropical cyclones according to the maximum sustained wind speed (1 min average), (**¡Error! No se encuentra el origen de la referencia.**). The scale is based on the expected damage on the manmade structures due to the storm. The same scale is used to rank typhoon in the North West Pacific, but the wind speed is a 10 min average.

The Australian Bureau of Meteorology uses a similar scale called Tropical Cyclone Severity Categories, which is based on the estimated maximum wind gusts. In the following the Saffir-Simpson scale will be used as reference.

There are seven tropical cyclone "basins" where storms occur on a regular basis (Fig. 3-2): Atlantic basin, including the North Atlantic Ocean, the Gulf of Mexico, and the Caribbean Sea (1); Northeast Pacific basin from Mexico to about the dateline (2); Northwest Pacific basin from the dateline to Asia including the South China Sea (3); North Indian basin, including the Bay of Bengal and the Arabian Sea (4); Southwest Indian basin from Africa to about 100°E (5); Southeast Indian/Australian basin (100°E to 142°E) (6); Australian/Southwest Pacific basin (142°E to about 120°W) (7).

Category	Damage	Wind Speed	Storm Surge
1	Minimal	from 33 to 42 *m/s*	from 1.2 to 1.5 *m*
2	Moderate	from 43 to 49 *m/s*	from 1.8 to 2.4 *m*
3	Extensive	from 50 to 58 *m/s*	from 2.7 to 3.7 *m*
4	Extreme	from 59 to 69 *m/s*	from 4.0to 5.5 *m*
5	Catastrophic	greater than 69 *m/s*	greater 5.5 *m*

Tab. 3-2: Saffir-Simpson hurricane damage and storm surge scale.

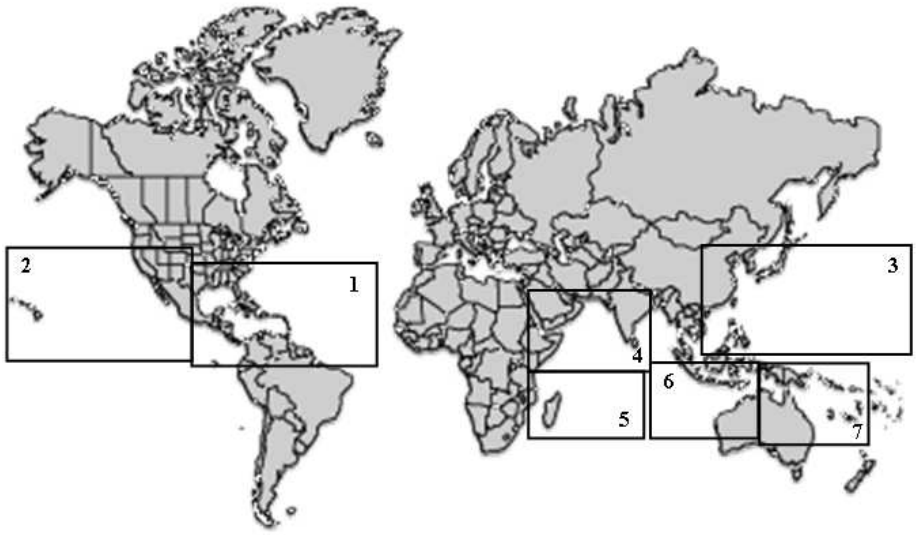

Fig. 3-2: Tropical cyclone basins

Basin	Responsible RSMC and TCWC	Web site
Atlantic	National Hurricane Centre	http://www.nhc.noaa.gov/
Northeast Pacific	Central Pacific Hurricane Centre, National Hurricane Centre	http://www.prh.noaa.gov/hnl/cphc/
Northwest Pacific	Japan Meteorological Agency	http://www.jma.go.jp/jma/indexe.html
North Indian	Indian Meteorological Department	http://www.imd.ernet.in/main_new.htm
Southwest Indian	Météo-France	http://www.meteofrance.com/
Southeast Indian/Australian	Bureau of Meteorology* (Australia)	http://www.bom.gov.au/
Australian/Southwest Pacific basin	Fiji Meteorological Service Meteorological Service of New Zealand* Papua New Guinea National Weather Service* Bureau of Meteorology* (Australia)	http://www.metservice.com/ http://www.pi-gcos.org/

Tab. 3-3: RSMC and the TCWC (*) centres.

Tropical Cyclone Basin	Tropical storm intensity Average (S.D.)	Hurricane intensity Average (S.D.)	Intense hurricane intensity Average (S.D.)
Atlantic(1944-95)	9.8 (3.0)	5.7 (2.2)	2.2(1.5)
Northeast Pacific(1970-95)	17.0 (4.4)	9.8 (3.1)	4.6 (2.5)
Northwest Pacific(1970-95)	26.9(4.1)	16.8 (3.6)	8.3 (3.2)
North Indian	5.4 (2.2)	2.2 (1.8)	0.3 (0.5)
Southwest Indian	10.3 (2.9)	4.9 (2.4)	1.8 (1.9)
Southeast Indian / Australian (1970-95) (1970-95)	6.5 (2.6)	3.3 (1.9)	1.2 (1.4)
Southwest Pacific/ /Australia (1970-95)	10.3 (3.1)	4.6 (2.4)	1.7 (1.9)
Global	86.1 (8.0)	47.3 (6.5)	20.1 (5.7)

Tab. 3-4: Annual average numbers and standard deviations over the period 1944-1995 for Atlantic Basin and 1970-95 for the other tropical cyclone basin.

Tracking, warning and advisory bulletins are issued by six Regional Specialized Meteorological Centres (RSMCs) worldwide. In addition, there are six Tropical Cyclone Warning Centres (TCWCs) that provide information to smaller regions. Tab. 3-3 lists the RSMC and the TCWC centres (marked with '*') according to their area of responsibility.

Tab. 3-4 contains the annual average and standard deviation of tropical cyclones in the various basins [Landsea, 2000]. For the Atlantic basin, thanks to a routine aircraft reconnaissance, records are available since the mid-1940s. For the remaining basins reliable estimates of tropical cyclones only exist from the beginning of the satellite era in the mid-1960s.

The Northwest Pacific Ocean is the most active basin on the planet. Annually, an average of 26.9 storms in the basin acquire tropical storm strength or greater; also, an average of 16.8 typhoons occurred each year during the 1970–1995 period. Intense tropical cyclones are most common in the Northwest and Northeast Pacific basins, making up nearly two-thirds of the average of 50 around the globe.

3.2 Cyclogenesis

Most of the tropical cyclones in the Atlantic and eastern north Pacific begin from westward travelling disturbances, known as easterly waves. On the weather maps these features appear as a 'wave' in the isobars that travel from east to west (Fig. 3-3). Given favourable conditions, an easterly wave may intensify and contract horizontally, ultimately resulting in the characteristic circulation of a tropical cyclone. In the western Pacific, large areas of upper-level low pressure help pull air from the centre of the developing disturbances and thus contribute to a drop in surface atmospheric pressure. These features, known as 'Tropical Upper Tropospheric Troughs', or TUTTs, are responsible for the larger number of tropical cyclones in the western Pacific.

Conditions necessary for the development of a tropical cyclone from a pre-existing disturbance are [NOAA HRD]:

- warm ocean temperature (at least 26.5°), needed to maintain the warm core that fuels tropical systems,
- high humidity,
- vertical wind shear less than 10 *m/s*,
- atmospheric instability,
- a distance from the equator of 500 *Km* or more to allows the Coriolis force to be enough strong.

Tropical cyclones are "warm core" storms in the sense that the air near the centre is warmer than the surrounding atmosphere.

The source of energy for tropical cyclones is the thermodynamic disequilibrium between the tropical atmosphere and the ocean [Emanuel, 1991]. The disequilibrium does not arise from difference in temperature between ocean and atmosphere that usually is less than 1°, but in the under-saturation of near-surface air with moisture [Emanuel, 1991]. The upper atmosphere at the same time has to be cool to allow the release of latent heat energy. This increases the generation of cumulonimbus which contributes to transport heat and moisture to the upper troposphere.

Once the warm air reaches the tropopause it spreads out laterally. The resultant effect of such dissipation of the vertical air column is a lowering of the near surface pressure and enhancing of

surface wind convergence. The Cyclonic circulation, initiated by the Coriolis effect, increases wind convergence and so the transport of warm air to the storm's core. The rate of heat transfer from the ocean to the atmosphere is a function of wind speed. This dependence is the principal feedback mechanism that allows tropical cyclones to develop, i.e. increasing surface winds lead to increase in heat transfer from the ocean, which leads to intensification of the winds, and so on.

3.3 Mature tropical cyclone structure

In the mature stage tropical cyclones present a well-organized structure. The air flows cyclonically (in the direction of Earth rotation) from the surface up to the top of the storm, where the direction of rotation is reversed (anticyclonic). Starting from the storm centre the wind increases rapidly, reaching the maximum intensity at a radius between 10 *km* and 100 *km*, i.e. the radius of maximum wind speed (RMW). Then the wind speed decreases more gradually with radius, following roughly an $r^{-\alpha}$ decay law, where $\alpha \approx 1/2$. Advection of the whole storm system leads to an asymmetry in the surface wind speed. The surface wind speed can be approximated by the sum of the storm-relative wind velocities around the centre and the translation velocity [Emanuel, 2003]. In the vertical direction the wind speed is maximal near the surface, at about 500 m height, decaying slowly upwards [Franklin J.L. et al., 2000]. Maximum wind shear allowed for the existence of tropical cyclones is of 10 m/s between the surface and the tropopause.

The transverse circulation, as shown in Fig. 3.4, consist of radial inflow within a boundary layer of about 1-2 *km* depth, ascent in correspondence of the eyewall and radial outflow in a thin layer at the top of the storm.

A characteristic feature of tropical cyclones is the presence of an eye, defined as a nearly cloud-free region, with little or no winds. Surrounding the eye is a wall of dense convective clouds rising about 15 *km* into the atmosphere. The eyewall is the area where the most violent winds and heaviest rainfall occur. Outside the eyewall clouds and precipitation are organized in one or more cyclonically curved spiral bands of order 10 *km* in width, extending to a height of 3 to 15 *Km* (Fig. 3-4).

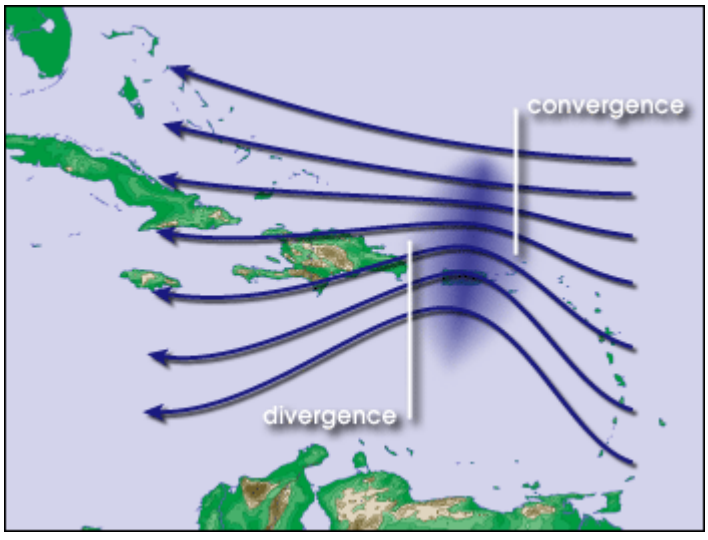

Fig. 3-3: Diagram of an easterly wave.

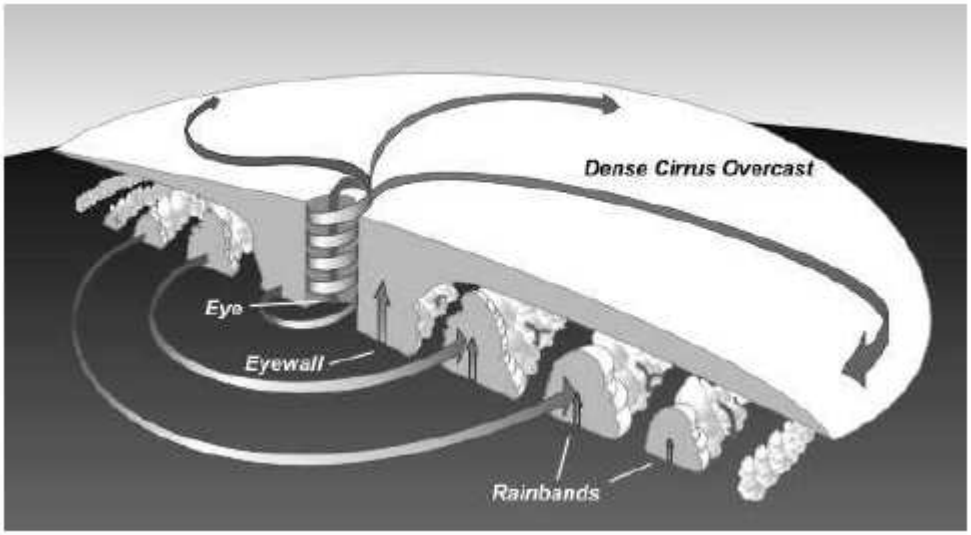

Fig. 3-4: Tropical cyclone section (Image courtesy NOAA)

In case of particularly intense storms the existence of concentric eyewall can occur, i.e. the small inner eyewall could be replaced by an outer one generated by nearly circular rain bands.

During this phase the storm tends to weaken to eventually reintensify after the replacement is completed.

In the Atlantic Ocean tropical cyclones move westward, but also drift toward the pole as a result of the Earth's rotation. Most of the Tropical cyclones that reach 70° - 80° W longitude "recurve" towards the north and eventually pass into the middle-latitude west winds that push them eastward into the high-latitude North Atlantic. There they dissipate over cold water or, after extratropical transition, eventually reach European waters as frontal cyclones.

Fig. 3-5 shows a global map of the tropical cyclones as recorded by the National Hurricane Centre and Joint Typhoon Warning Centre. The time period spans from 1860 to 2006 for National Hurricane Centre track data and from 1959 to 2006 for the Joint Typhoon Warning Centre. The tropical cyclone tracks are color-coded according to the Sapphire-Simpson scale. The image clearly shows several features associated with tropical cyclones climatology, such as the absence of storm tracks around the equator and the different basins where tropical cyclones develop. The prevalent path followed by the different storms also reveals the large scale atmospheric flows that influence the tracks of tropical cyclones. Another interesting feature that can be observed is the absence of tracks in the Southwest Pacific and South Atlantic Ocean due to the presence of strong wind shear (which disrupts cyclone formation), cool water temperatures, and a lack of weather disturbances favourable for tropical cyclone development. The records register only one exceptional tropical cyclone (Catarina) that developed in the South Atlantic off the east coast of Brazil in 2004, due to exceptionally unusual, favourable upper level winds and above average water temperatures from 24º to 26º C [McTaggart-Cowan et al. 2006].

3.4 Modelling of a tropical cyclone's wind field

Numerical models are utilized extensively to study cyclone behaviour. The early tropical cyclone wind models, of parametric type, made use of a modified Rankine vortex [Hughes, 1952], that describes the velocity profile of vortices in real, viscous fluids.

In 1954 Schleomer suggested a model that relates the wind field to the pressure field [Schleomer, 1954]. To improve the Schleomer model, that produced some errors in the estimation of the radial extent of tropical cyclone wind fields, Holland proposed a modified formulation [Holland, 1981]. Such models are of parametric type and produce as output the tropical cyclone wind speed field.

With the advent of high speed computers more sophisticated models, which solve the physical equations describing the motion of the atmosphere in both the large-scale circulation and the tropical cyclone itself, have been developed. This kind of models is able to reproduce:

- the inflow of low-level air into the hurricane's inner core region;
- the supply of the storm's energy from the release of the latent heat of water vapour evaporated at the ocean surface;
- the updraft of warm, moist air that feed thunderstorms in the core region of the storm, which helps to intensify the hurricane;
- the outflow of cooler, drier air at upper levels of the troposphere.

Some of these models, e.g. GFDL [Bender et al, 1997], [Kurihara et al., 1998], are used operationally by the National Hurricane Centre (NHC) to forecast tropical cyclone intensity and track [NOAA NHC].

In this study the Holland model has been chosen as a reference model because of its analytical nature. Such a model can easily be optimized and thus used together with SAR wind field measurements improving the wind field in area where the SAR measure saturate.

3.5 The parametric Holland model for tropical cyclones' wind speed.

The Holland Model is an analytical model for the radial profiles of wind speed V_r in a tropical cyclone [Holland, 1980]. As shown in [Schleomer, 1954] the relationship between the pressure and the radial distance in tropical cyclone follows a hyperbolic law:

$$r^B \ln\left[\frac{p_n - p_c}{p - p_c}\right] = A \tag{3.1}$$

where A and B are scaling parameters, p_n is the ambient pressure (corresponding to the value of the first anticyclonically curved isobar), p_c is the pressure in the tropical cyclone centre and p is the pressure at radius r.

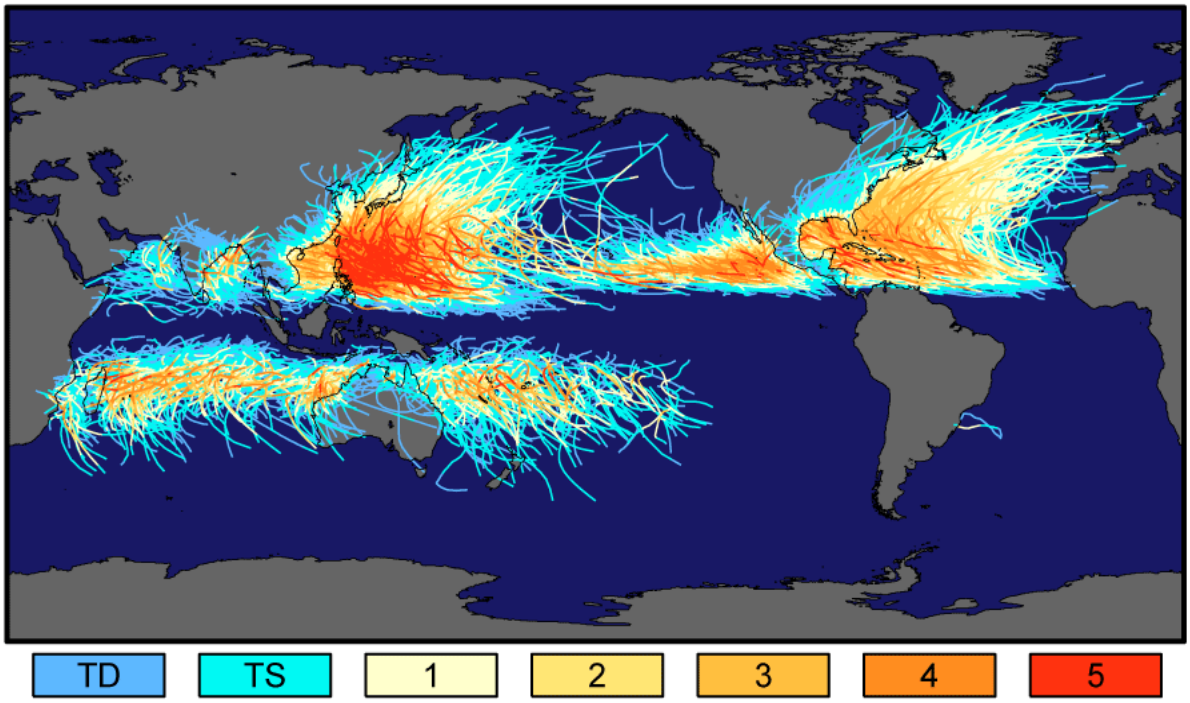

Fig. 3-5: Global track and intensity map of tropical cyclones (image courtesy: Robert A. Rohde). The tracks are coloured according to the Saffir-Simpson scale.

Using the gradient wind formula [Andrews, 2000] the wind profile can be expressed as:

$$V_g = \left[AB\frac{(p_n - p_c)}{\rho r^B}\exp\left(-\frac{A}{r^B}\right) + \frac{r^2 f^2}{4}\right]^{\frac{1}{2}} - \frac{rf}{2} \tag{3.2}$$

where V_g is the gradient wind at radius r, f is the Coriolis parameter and ρ the air density. In the region of maximum wind the pressure gradient and the centrifugal force are much bigger than the Coriolis force and the air is in cyclostrophic balance, thus equation (3.2) can be reduced to:

$$V_{MW} = \left[AB\frac{(p_n - p_c)}{\rho r^B}\exp\left(-\frac{A}{r^B}\right)\right]^{\frac{1}{2}} \tag{3.3}$$

Setting dV_{MW}/dr equal to zero we get the radius of maximum wind R_{MW}:

$$R_{MW} = A^{\frac{1}{B}} \tag{3.4}$$

R_{MW} is independent of the values of central and ambient pressure. Substituting formula 3.4 in 3.3 leads to the formula of the maximum wind speed V_M:

$$V_M = C(p_n - p_c)^{\frac{1}{2}} \tag{3.5}$$

where

$$C = \left(\frac{B}{\rho e} \right)^{\frac{1}{2}} \tag{3.6}$$

with e equal to the base of the natural logarithm.

The A parameter determines the location of the peak in the wind profile relative to the origin and B defines the shape of the tropical cyclone wind profile. As the difference between the central pressure and the environment pressure increases, the wind profile becomes more peaked with higher wind speed more concentrated around the radius of maximum wind and a reduction of the radius of destructive winds.

In a final step to obtain a more realistic simulation a vector corresponding to the direction and speed of forward movement of hurricane, V_A, has been added to the Holland wind field:

$$\vec{V} = \overrightarrow{V_g} + \overrightarrow{V_A} \tag{3.7}$$

For physical reason the B parameter should be between 1 and 2.5. To keep the radius of maximum wind speed coincident with the radius of maximum pressure gradient the B parameter cannot be less than 1, while constraints on the conservation of the relative angular momentum of the air flowing inside the storm places the upper bound [Holland, 1980].

Fig. 3-6 shows the effect of varying the B parameter on the wind profile. Fig. 3-7 shows an example of the simulation of a tropical cyclone wind field using the Holland model. The input parameters for this simulation V_m, R_{MW} and p_c have been taken from the NOAA Hurricane Research Division with reference to the hurricane Katrina on September 28 15:00 UTC.

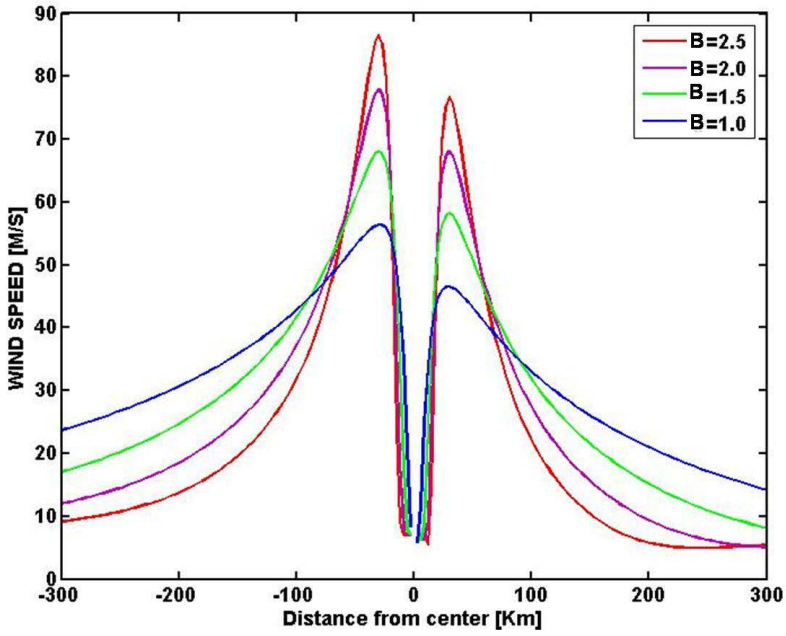

Fig. 3-6: Holland wind speed profile for different values of *B*

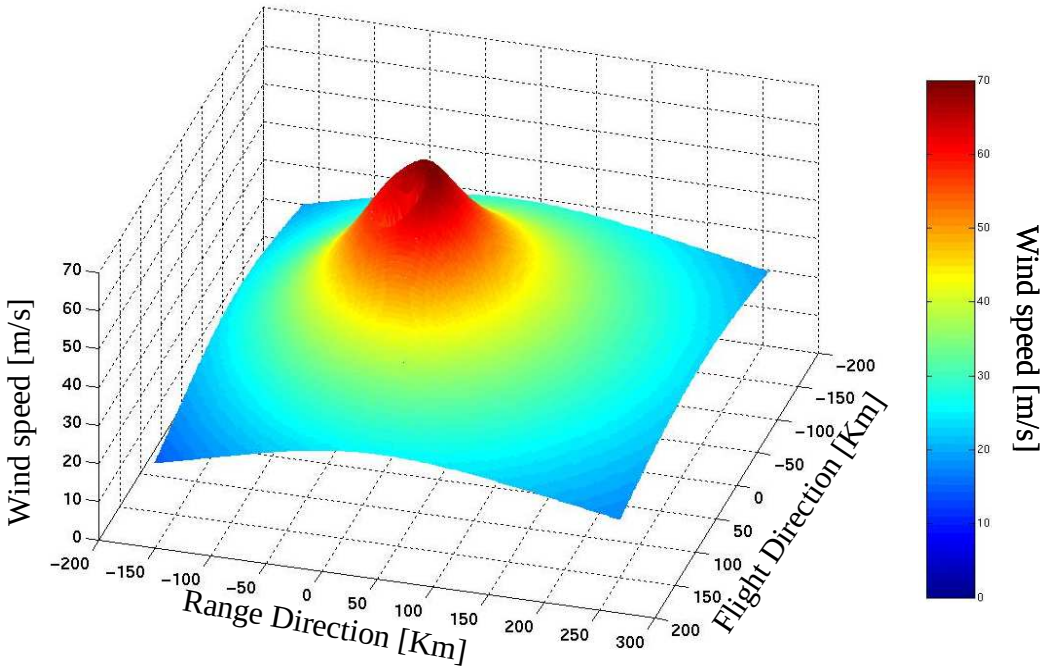

Fig. 3-7: Holland wind field simulation of hurricane Katrina on September 28 15:00 UTC

3.6 References

Aberson, S. D., 1998, Five-day tropical cyclone track forecasts in the North Atlantic basin. *Wea. Forecasting*, no. 13, pp 1005-1015.

Andrews D. G.,2000. An Introduction to Atmospheric Physics. *Cambridge University Press.*

Bender, M.A., I. Ginis, R. Tuleya, B. Thomas, and T. Marchok, 2007, The Operational GFDL Coupled Hurricane–Ocean Prediction System and a Summary of Its Performance. *Mon. Wea. Rev.*, 135, 3965–3989.

Brand, S., K. Rabe, and T. Laevastu, 1977, Parameterization Characteristics of a Wind-Wave Tropical Cyclone Model for the Western North Pacific Ocean. *J. Phys. Oceanogr.*, 7, 739–746.

Chao Y.Y., Burroughs L.D. and Tolman H.L. , 2003, Wave Forecasting for Western North Atlantic Ocean and Adjacent Waters. *Technical Procedures Bulletin*, no. 495, NationalWeather Service, NOAA, U.S. Department of Commerce.

Dvorak V., 1975, Tropical cyclone intensity analysis and forecasting from satellite imagery. Mon. *Wea. Rev.*, no 103, pp. 420 430.

Emanuel K. A., 2003, Tropical Cyclones. *Ann Rev. Earth Planet. Sci*., no. 31, pp.75-104.

Emanuel K.A., 1991, The theory of hurricanes. *Annual Rev. Fluid Mech.*, no. 23, pp. 179-196.

Franklin J. L., Black M. L., Valde K., 2000, Eyewall Wind Profile Determined by GPS Dropsondes. *Weather and Forecasting*, no. 18, pp 32-44.

Gordon C.T., Stern W., 1982, A description of GFDL Global Spectral Model. *Mon. Wea. Rew*., no. 110, pp 625-644.

Hawkins, J. D., T. F. Lee, K. Richardson, C. Sampson, F. J. Turk and J. E. Kent, 2001, Satellite multi-sensor tropical cyclone structure monitoring. *Bull. Amer. Met. Soc.*, no. 82, pp. 567-578.

Katsaros, K. B., Vachon, P. W., Liu, W. T. and Black, P. G., 2002, Microwave remote sensing of tropical cyclones from space. *Journal of Oceanography*, 58, pp. 137-151.

Kidder S. Q., Goldberg M. D., Zehr R. M., DeMaria M., Purdom J.F.W., Velden C. S., Grody N.C. and Kusselson S. J., 2000. Satellite analysis of tropical cyclones using the advanced microwave sounding unit (AMSU)", *Bull. Amer Meteor Soc.*, no. 81, pp. 1241-1259.

Holland, G. J., 1980, An analytic model of the wind and pressure profiles in hurricanes. *Mon. Wea. Rev*. no. 108, pp.1212-1218.

Hsu, S. A., M. F. Martin, Jr., and B. W. Blanchard, 2000, An evaluation of the USACE's deepwater wave prediction techniques under hurricane conditions during Hurricane Georges in 1998. *Journal of Coastal Research*, no. 16, pp.823-829.

Hughes L. A., On the low level structure of tropical storms. *J. Meteor*., no. 9, pp. 422–428, 1952.

Insurance Information Institute: http:// www.iii.org/media/facts/statsbyissue/hurricanes.

Kurihara, Y., Tuleya, R. E. and Bender, M. A., 1998, The GFDL hurricane prediction system and its performance in the 1995 hurricane season. *Monthly Weather Review*, 126, pp. 1306-1322.

Landsea C.W., 2000, Climate Variability of Tropical Cyclones: Past, Present and Future. *Edited by R. A. Pielke, Sr. and R. A Pielke, Jr, Routledge, New York*, 220-241.

McTaggart-Cowan, R., Bosart, L. F., Davis, C. A., Atallah, E. H., Gyakum, J. R., and Emanuel, K. A., 2004, Analysis of Hurricane Catarina . *Monthly Weather Review*, no 134, pp. 3029–53, 2006.

NOAA HRD: http://www.aoml.noaa.gov/hrd/

NOAA NHC: Technical Summary of the National Hurricane Centre Track and Intensity Models, update 2009, http://www.nhc.noaa.gov/modelsummary.shtml.

Quilfen, Y., B. Chapron, T. Elfouhaily, K. B. Katsaros and J. Tournadre, 1998, Observations of tropical cyclones by high-resolution scatterometry. *J. Geophys. Res.*, no. 103, pp. 7767–7786.

Ross, D., 1976, A simplified model for forecasting hurricane generated waves. *Bul. Am. Meteo. Soc.*, no. 57(1), pp. 113-114.

Schloemer R. V., 1954, Analysis and synthesis of hurricane wind patterns over Lake Okeechobee, Florida. *Hydrometeorological Report*, USWB, no. 3, pp 1-49.

4 Wind speed retrieval from SAR images

4.1 The state of the art

The use of SAR images gives the opportunity to obtain a high resolution wind field to be used in all the applications where the knowledge of the fine scale structure of the wind field is required, e.g. wind farm siting, coastal monitoring, near coastal wind field, high vulnerability.

The retrieval of a high resolution wind speed maps from SAR images is a well established technique [Lehner et al., 1998] [Horstmann et al., 2003] [Monaldo et al., 2005]. In particular under tropical cyclone conditions, where numerical modelling and forecasting of ocean wind fields is still a challenge, SAR data can be used to improve the existing numerical model using assimilation techniques [Horstmann et al, 2005], [Morey et al., 2005], [Perrie et al., 2008].

Using the technique based on the inversion of a geophysical model function (GMF), SAR wind fields are retrieved in two steps. In the first step wind directions are retrieved, which are a necessary input in the second step to retrieve wind speeds. Fig. 4-1 shows a flowchart of the processing chain used to estimate wind fields from SAR images.

In this chapter the different algorithms developed, with particular emphasis on tropical cyclone wind speed retrieval, are described.

In the first section the geophysical model used to retrieve wind speed is presented. Then the SAR image calibration is discussed in detail for the different types of data, as this is the basis for a correct retrieval of the wind speed. As wind direction is required as additional input to the geophysical model the different techniques to retrieve this information directly from SAR images or from numerical models are described. In the last section of the chapter the different algorithms developed for wind speed retrieval, and in particular for tropical cyclone conditions, are detailed.

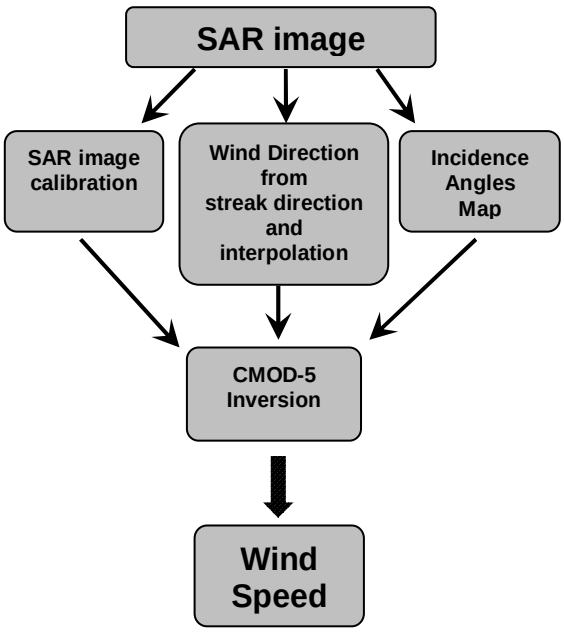

Fig. 4-1: Flowchart of the wind speed retrieval from SAR images.

4.2 The GMF

For C-band frequencies and moderate incidence angles between 20° and 60° the main contribution of backscattering from the ocean surface is due to the so called Bragg resonance [Hasselman et al. 1985], [Ulaby et al. 1982]. According to this model the backscattered power is proportional to the density of surface elements whose size is comparable to the wavelength of the incident electromagnetic radiation. For microwaves the corresponding roughness is generated by so-called short-gravity and capillary ocean waves.

These waves respond instantaneously to the wind that blows over the sea surface. Moreover, as they are distributed around the direction perpendicular to the local wind they make the radar backscattering dependent on the wind direction. Therefore the backscatter can be used as a measure of the local sea surface wind.

The condition for resonance is dependent on the microwave wavelength λ_r and the incidence angle θ and is given by (Fig. 4-2):

$$\lambda_B = \frac{\lambda_r}{2\sin\theta} n \tag{4.1}$$

where λ_B is the Bragg resonant wavelength, and n a positive number [Wright, 1978].

To relate the radar geometry and the NRCS measurements to the surface wind field (10 *m* height) a geophysical model function is used. GMF models are empirically based upon statistical analysis and physical knowledge of the a-priori behaviour of the backscatter signal, and properly tuned for the sensor employed. The general form of such semi empirical models is [Ulaby et al. 1982]:

$$\sigma^0(\chi, U, \theta) = a\,(1 + b\cos\chi + c\cos 2\chi) \tag{5.10}$$

where U is the near surface wind speed usually defined at 10 *m* height, and χ is the azimuth angle, i.e. the angle between the wind direction and the antenna beam look direction. A wind blowing in the direction of the radar beam and toward the radar is referred to as upwind (χ=0°), while one blowing away from the radar is referred to as downwind (χ=180°), and the one perpendicular to the

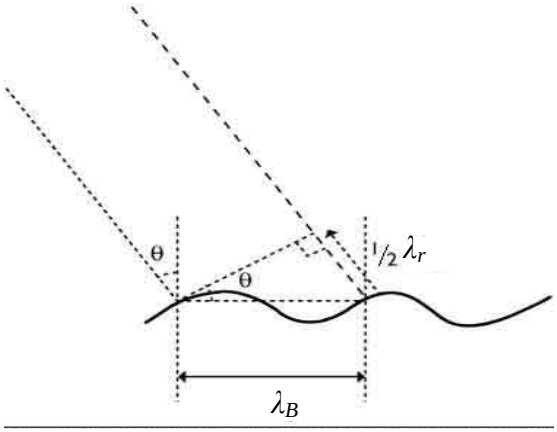

Fig. 4-2: Bragg resonance. λ_r is the radar wavelength, θ the incidence angle and λ_B is the Bragg resonant wavelength.

radar is referred to as crosswind (χ=90° and χ=270°). The coefficients *a*, *b* and *c* are functions of the wind speed and incidence angle, modelled using Legendre polynomials.

For C-band and vertical polarization the CMOD GMF is used [Stoffelen and Anderson, 1997], [Quilfen et al. 1998], [Hersbach et al., 2007]. A series of CMOD functions were tuned to different sets of parameters. The latest version of this family, CMOD5, is particularly suited for the retrieval of wind fields in case of storms, as backscatter measurements in extreme winds conditions obtained by aircraft and in situ measurements have been used to tune the model function. The GMF was adapted by Hersbach and Stoffelen using ECMWF model wind and data from the Imaging Wind and Rain Airborne Profiler (IWRAP) instrument [Hersbach et al., 2007].

Fig. 4-3 shows the behaviour of the NRCS as modelled using the CMOD-5 GMF for different wind directions (a) and wind speeds (b), and an incidence angle of 25°.

In Fig. 4-4 a 3-D plot of NRCS evaluated by CMOD5 for different wind speeds and directions, for an incidence angle of 25° is shown. For high wind speeds the CMOD-5 model accounts for the reduction of the drag coefficient, that is a measure of the momentum exchange at the sea surface. A reduction of the drag coefficient will lead to a reduction of surface roughness and thus to a reduction of the SAR measured NRCS. One can observe that for a wind speed above 25 *m/s* the GMF starts saturating and for hurricane force winds or even higher ones it is reduced. This behaviour is confirmed by measurements in a wave tank [Powell et al., 2003]. It can also be observed that the area of CMOD5 that ranges from 30 *m/s* to 70 *m/s* is contained in one *dB* or less. This makes wind speed retrieval from SAR even more challenging, considering that the radar measurement is affected by noise or attenuation.

4.3 Image calibration.

In order to invert the GMF, the NRCS has to be derived from the image. The measure of NRCS has the advantage to be independent of a particular sensor used to acquire the data, and depends only on

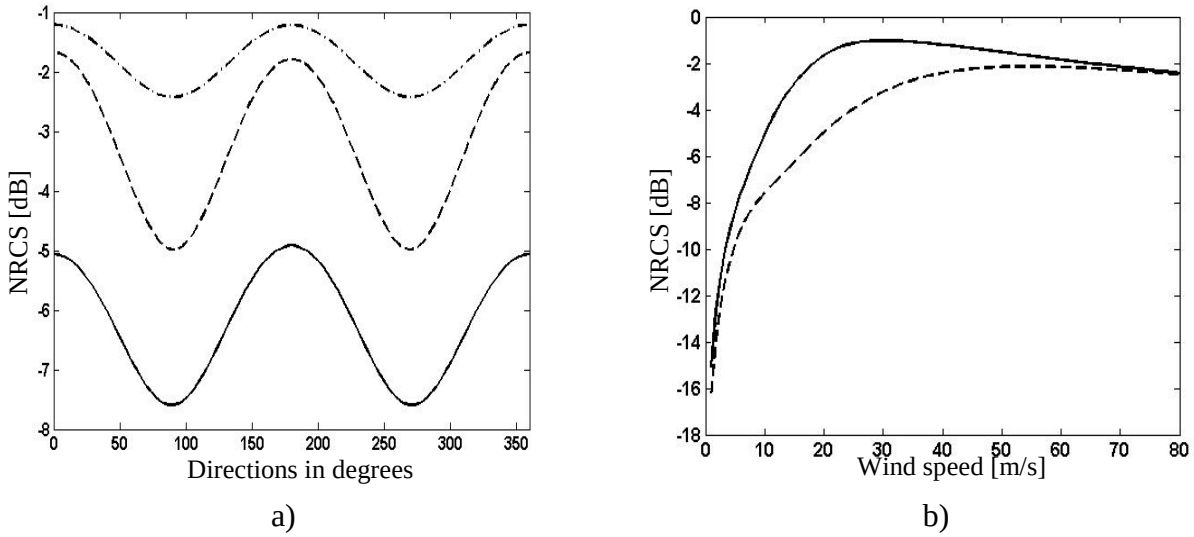

Fig. 4-3: NRCS behaviour for different wind directions (a) (wind speed equal to 10 m/s continuous line, 20 m/s dashed line and 40 m/s dash-dotted line) and different wind speed (b) (up-wind continuous line, cross-wind dashed line) for a fixed incidence angle of 25° at C-band according to CMOD-5.

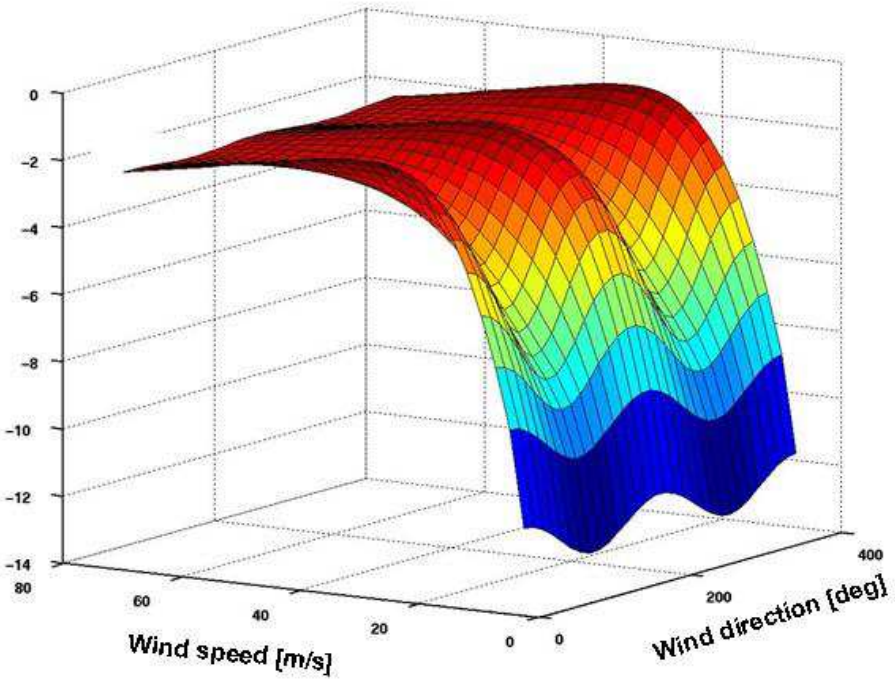

Fig. 4-4: Plot of CMOD-5 GMF for various wind speeds and directions and a fixed incidence angle of 25°.

the radar frequency, the geometry of acquisition and the scene characteristics, like roughness, or dielectric constant.

The relationship between the image amplitude, given in digital number "*DN*", and the radar NRCS coefficient (σ^o) can be written as:

$$\sigma^0 = DN^2 \frac{\sin(\theta)}{K} \tag{4.1}$$

where θ is the local incidence angle and the constant factor K is the "Absolute Calibration Constant", derived from measurements over precision transponders [Zink et al., 2002]. The factor K is processor and product type dependent, and may change between different beams for the same SAR product type.

4.3.1 Wide swath data radiometric quality

Assessment of the radiometric quality, which consists in the measurement of the radiometric accuracy, radiometric stability and radiometric resolution, is needed to better understand the SAR performance when used for wind speed retrieval.

In Tab. 4-1 the ENVISAT ASAR wide swath mode radiometric quality parameters are summarized [Buch et al., 2000]. Radiometric accuracy is defined as the absolute accuracy of the radar cross-section measurement, which is the difference between the nominal and the measured target radar cross-section [Bally, Kader, 1995]. Radiometric stability bounds are given by the temporal variability of the instrument response from a target of constant σ^o. The radiometric resolution of a SAR image, in *dB*, is the measurement of the ability to distinguish between targets with different σ^o. The equivalent number of look is intended to represent the speckle component of the observed intensity.

Parameter	Value
Radiometric Resolution	1.45 dB to 1.72 dB
Radiometric accuracy	1.20 dB to 1.45
Radiometric stability	0.32 dB to 0.42 dB
Equivalent number of look	>12

Tab. 4-1: ENVISAT ASAR radiometric quality parameter.

Speckle noise occurs in a coherent system such as SAR, and affects the radiometric accuracy. Speckle is multiplicative noise which is formed as a result of random phase variations in the interaction between the radar signal and the surface [Ulaby et al. 1982].

Statistics of speckle are usually described in terms of the Effective (or Equivalent) Number of Looks (*ENL*), defined by the normalized standard deviation in a SAR image of a homogeneous target [Bally and Fellah, 1995]:

$$ENL = \frac{1}{(qr)^2} \tag{4.2}$$

where *qr* is the normalized standard deviation:

$$qr = \frac{\sigma}{\mu} \tag{4.3}$$

μ and σ are the sample mean and standard deviation of the signal power .

qr is a measurement of the width of the SAR signal power distribution. The corresponding interval Δ_{qr} around the expected intensity I_{expec} is:

$$\Delta_{qr} = \left[(1-qr)\cdot I_{\exp ec};(1+qr)\cdot I_{\exp ec}\right] \tag{4.4}$$

As an example, in the case of the ASAR Wide Swath Mode image, as *ENL* =12 the value of *qr* is :

$$qr = ENL^{-\frac{1}{2}} = 0.2887 \tag{4.5}$$

For a homogeneous target the recorded values are distributed around the expected value I_{expec} with a standard deviation equal to 0.2887. Therefore certain amounts of data lie within the interval:

$$\left[\sigma^o - 1.47\,dB;\ \sigma^o + 1.1\,dB\right] \tag{4.6}$$

where σ^o is the expected NRCS.

Radiometric confidence intervals can be reduced by averaging over independent 'uncorrelated' pixels in the radar image. The relationship between the *ENL* after pixel averaging and the original *ENL* is:

$$ENL_{average} = ENL_{orig.} \cdot \frac{N}{R} \tag{4.7}$$

where N is the number of pixels of the averaged area and R is the number of pixels per resolution cell in the radar image.

In the case of ASAR Wide Swath Mode Image, averaging over 40 x 40 pixels, corresponding to an area of 3 *Km* x 3 *km*, leads to an improvement in the error bound of:

$$\left[\sigma^o - 0.41dB; \sigma^o + 0.37dB\right] \tag{4.8}$$

This value of averaging will be used in the following to retrieve wind fields, as it assures a radiometric accuracy of the same order as scatterometer.

4.3.2 Wave mode data calibration

The ERS-2 Wave Mode images are not delivered as radiometrically calibrated data by ESA. In any case to use them for wind speed retrieval and wave analysis their mean intensity has to be accurately calibrated and translated into NRCS values.

Due to the small variation of the incidence angle across Wave Mode images equation 4.1 reduces to:

$$\sigma^0 = \frac{DN^2}{K} \tag{4.9}$$

In this study the calibration of the imagettes was performed using the calibration constant K estimated by [Horstmann et al., 2003] using a data set acquired in September 1996. Before applying the calibration a cross check with a new data set of 6000 Wave Mode data, acquired three years later between September 1 and September 30 1999 by the ERS-2 Satellite and collocated with the ERS-2 Scatterometer data, has been performed to detect a possible drift in the value of the constant. The Wave Mode images NRCS have been compared with the corresponding scatterometer NRCS.

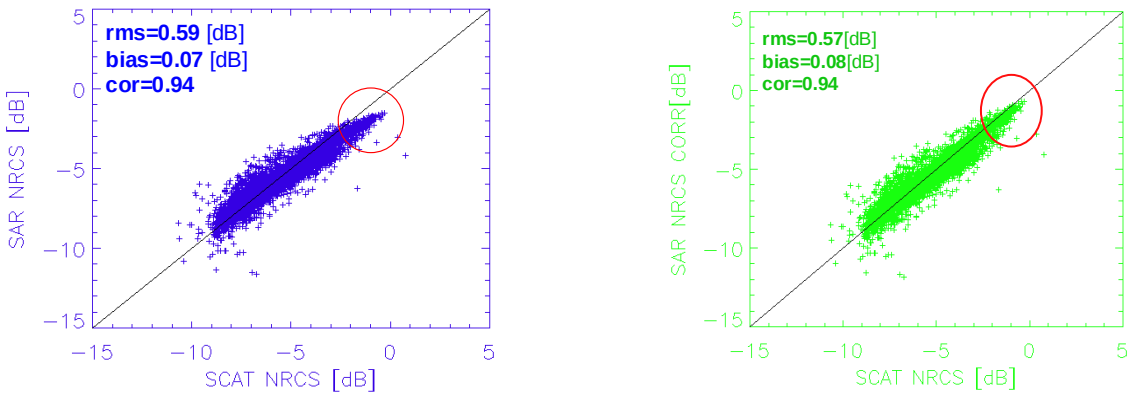

a) b)

Fig. 4-5: Plot of Scatterometer NRCS vs. Imagette NRCS. a) before correction, b) after correction using I Q standard deviation (see Fig. 4.6)

The scatterometer NRCS values have been retrieved using the wind fields delivered by the French Processing Facility to invert the geophysical model function CMOD-2FR [Quilfen et al., 1998] originally used to estimate them. Since the real (*I*) and imaginary(*Q*) data channel of Wave Mode data are quantized by the analog to digital converter (ADC) with a limited number of bits (4 bits for each channel), NRCS measurement are affected by a saturation effect, particularly for high values of NRCS. In Fig. 4-5 a) this effect is shown plotting the imagettes NRCS versus the simulated scatterometer NRCS.

The power loss correction (Fig. 4-6) [Kerbaol et al., 1998] is given as function of the *I* or *Q* channel standard deviation which is computed as part of the processing from the raw data. Fig. 4-5 b) shows the scatter plot of the Wave Mode data NRCS vs the scatterometer NRCS after the power loss correction is applied. It can be observed that the power loss correction is significant for values above -4 *dB*. This level of NRCS values can easily be reached in tropical cyclones conditions, at wind speed above 30 *m/s*.

4.4 Wind direction retrieval using spectral analysis

As shown in the workflow of Fig. 4-1 wind direction is required as input in the SAR wind speed retrieval algorithm. For this purpose the derivation based on spectral analysis has been chosen for its robustness and relatively easy implementation, allowing it to be put in a semi-automatic chain.

On SAR images often so-called “wind streaks” are visible, ranging in wavelengths from 600 to 2,000 meters [Alpers and Bruemmer, 1994]. In Fig. 4-7 (a) the direction and wavelength of the wind streaks measured from the image of hurricane Katrina are shown. The variation in sea surface roughness that makes wind streaks visible on SAR images is explained by changes in surface wind speed due to the formation of boundary layer rolls.

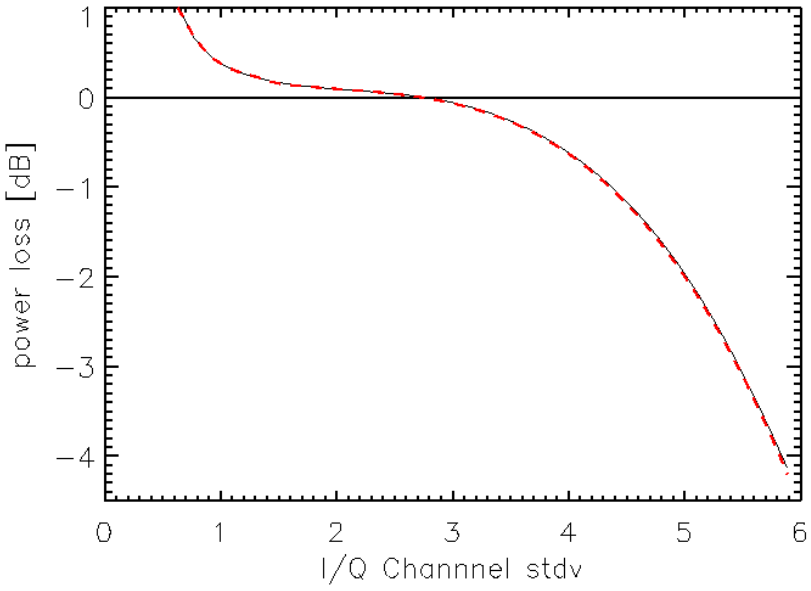

Fig. 4-6: I Q standard deviation vs power loss for ERS-2 Wave mode images.

Under combined surface heating and strong winds, horizontal helical circulations can form in the boundary layer. These circulation are consists of clockwise and counterclockwise pair of helices [Stull, 1998] (Fig. 4-8). They have an important role in the vertical exchange of momentum, heat and moisture in the atmosphere. The direction of these rolls is assumed to be parallel to the wind direction [Lehner et al., 1998]. The wavelength of wind streaks can be related to the roll size and thus the mixed layer depth [Foster, 2007], [Morrison et al., 2005].To determine wavelength and direction of wind streaks from SAR images as first step the image is divided in subscenes of 10 *km* x 10 *km*. Then an FFT analysis is performed on each subscene, in order to obtain the 2 dimensional image spectrum. To remove spectral features, which are not due to wind streaks, a filtering is applied on the image spectrum, cutting out the frequencies higher than 500 *m* and lower than 2000 *m*. Fig. 4-7 b shows as an example the filtered spectrum retrieved from the box highlighted by the light-blue square in Fig. 4-7 a. The orientation of the streaks (black arrow) is perpendicular to the main spectral energy peaks.

As the image spectrum is symmetric there is a 180° ambiguity in the estimated wind direction. This ambiguity may be removed through comparison with other data sources or through a study of wind shadows in the images. In particular, for the analysis of tropical cyclones, knowing that in the Northern (Southern) hemisphere the winds field follows a spiral path in anticlockwise (clockwise) direction is possible to resolve the 180° direction ambiguity without external information.

Due to many sea surface features it is often not possible to retrieve the wind direction over the complete swath using the aforementioned technique, as shown in Fig. 4-6 a. To obtain a uniform field of wind direction an interpolation is performed as final step.

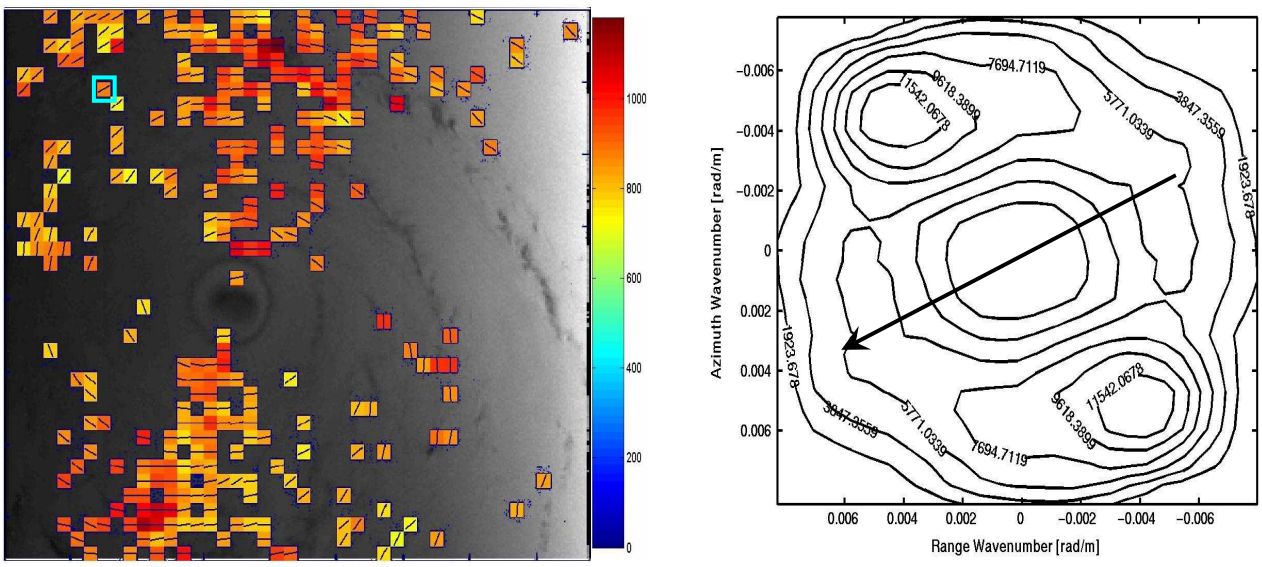

a) b)

Fig. 4-7: a) Wind streaks retrieved from the ASAR image of hurricane Katrina. b) Two dimensional spectrum retrieved from the box highlighted with light-blue in a). The black arrow represents the wind direction, perpendicular to the main spectral energy peaks.

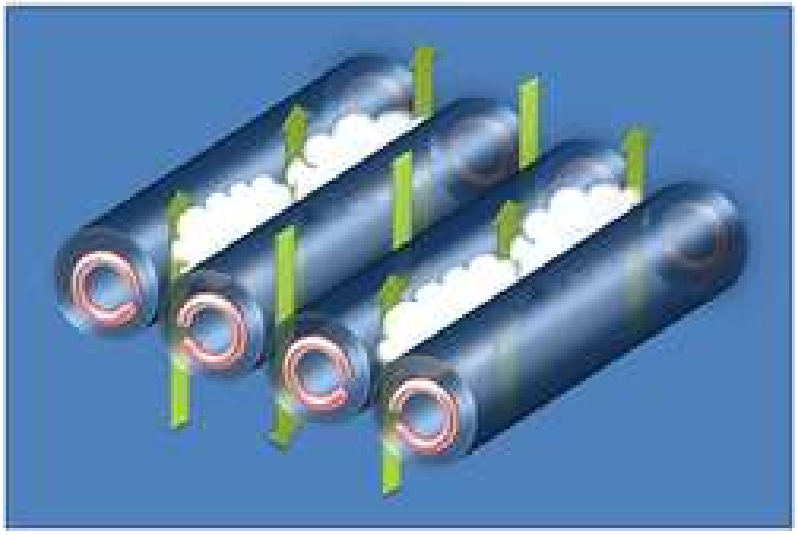

Fig. 4-8: Wind rolls in the planetary boundary layer.

4.5 The SAR wind speed retrieval algorithm

In this section the algorithms developed to retrieve the wind field from SAR images are described. Particular attention is given to the scatterometer approach as it is employed for the following analysis.

4.5.1 Scatterometer based approach

This method is based on the direct use of a GMF that links wind speed and direction to NRCS measurements. The method is widely accepted, and used in operational services.

For a fixed incidence angle, given a wind speed and direction vector as input to the GMF, it produces a unique value of NRCS. The inverse is not true as a particular value of NRCS can be associated to several pairs of wind speed and direction. For a Scatterometer the problem can be solved thanks to the multiple acquisitions of the same area from different look angles that the sensor operates. In the case of SAR, where only one acquisition with fixed look angle is available, the problem is indeterminate. It is therefore necessary to know the wind direction a priori in order to determine the wind speed.

It is possible to obtain information on wind direction from the SAR images itself detecting linear features, like wind streaks, aligned with the wind direction. Several methods to determine the wind streak direction have been developed, e.g. spectral analysis [Lehner et al., 1998], wavelet analysis [Du et al., 2002;] and local gradients [Koch, 2004]. The 180° ambiguity associated with these methods may be removed through comparison with other data sources or through a study of wind shadows in the images. In this study the method based on the FFT analysis for the streak detection [Lehner et al., 1998] has been chosen as previous studies have shown a good retrieval of wind direction in tropical cyclone conditions, in which the general circulation is known.

A reasonable estimate of wind direction may also be provided by numerical model data [Monaldo, 2000], scatterometry [He et al., 2005], or in situ measurements [Hasager et al., 2004]. Unfortunately the spatial resolution at which these data are provided is too coarse, not allowing resolving the fine scale structure of the wind field that may be retrieved from SAR images.

Once the wind direction is estimated for each cell of the SAR image the inversion of the GMF can be performed. When the wind direction is known a priori, the wind speed retrieval procedure is straightforward, and requires only the solution of a "zero-crossing" problem. At given $\sigma^o(i,j)$ in cell (i,j) the corresponding value of wind speed $v(i,j)$ for a fixed wind direction φ_0 and incidence angle θ_0 is :

$$v(i,j) = \min\left(\sigma^0_{(\varphi_0\theta_0)} - \sigma^0(i,j)\right) \tag{4.10}$$

where $\sigma^o_{(\varphi_0\theta_0)}$ is the simulated NRCS for fixed φ_0 and θ_0 and wind speed varying between 3 *m/s* and 80 *m/s*.

4.5.2 2D-var retrieval approach

This inversion technique uses an optimal inversion method that combines numerical weather prediction data with the measured NRCS and the GMF [Portabella et al 2002]. Using a two dimensional variational approach a cost function whose minimization leads to the optimal wind vector is defined.

The cost function can be written as:

$$J = \left(V - V_{NWP}\right)^T B^{-1}\left(V - V_{NWP}\right) + \left(\sigma^o_{SAR} - \sigma^o_{GMF}\right)^T R^{-1}\left(\sigma^o_{SAR} - \sigma^o_{GMF}\right) \tag{4.11}$$

where V is the estimated wind field, V_{NWP} is the model wind field, σ^o_{SAR} is the SAR measured NRCS and σ^o_{GMF} is the NRCS estimated from GMF. B and R are the error covariance matrices of the NWP estimates and NRCS measurements respectively, which under the assumption of no spatial correlation are diagonal matrices.

The method produces results comparable with the ones of the Scatterometer approach, but it requires a considerable processing time.

4.5.3 Neighbouring blocks approach.

This technique estimates the complete wind field, speed and direction, using the NRCS measurements from two neighbouring subimage blocks, having slightly different incidence angles [He et al., 2005].

The method is based on the minimization of the following cost function, assuming that the wind vectors of two neighbour subimages in the range direction are equal:

$$I = (\sigma^o_{1SAR} - \sigma^o_{1GMF})^2 + (\sigma^o_{2SAR} - \sigma^o_{2GMF})^2 \tag{4.12}$$

where σ^o_{iSAR} is the measured NRCS and σ^o_{iGMF} is the GMF predicted NRCS. The minimization process requires that the partial derivative with respect to wind speed and wind direction have to be equal to zero. The technique requires external information on wind direction to remove the 180° ambiguity. The method is still experimental and needs some improvements to reach the accuracy level of the other techniques.

4.6 Retrieval of wind speed in tropical cyclone conditions

SAR provides an alternative approach to acquire observations for improved and timely characterization of the wind field of tropical cyclones. Since the launch of satellites like RADARSAT or ENVISAT, that are able to acquire SAR images with dimensions up to 500 *Km* x 500 *Km* and so to capture the whole structure of a tropical cyclone, a growing interest has been shown by the scientific community to use these images for the retrieval of wind field and the analysis of atmospheric features associated with the storm. While several authors have shown that SAR images can be helpful to improve the understanding of the storm morphology [Katsaros et al., 2000], [Vachon et al., 2002], the retrieval of wind fields and in particular the maximum wind speed is still an open issue. Several authors have observed that using the technique based on the inversion of a scatterometer GMF for SAR wind speed retrieval in hurricane force wind conditions the results are biased low when compared to in situ measurements [Horstmann et al., 2005].

Besides the approach described in section 4.4, Perrie et al., (2006) extended the application given by He et al. (2005) to tropical cyclones. However, external wind direction information is still needed to find the best solution for the cost function. Shen et al., (2006) modified the method, making it possible to retrieve wind vectors from SAR images without external information, in certain circumstances. However, an apparent bias still exists for hurricane wind speed in the studies of both Perrie et al., (2006) and Shen et al., (2006).

Long and Nie, (2007) proposed a new technique based on the use of a numerical model to recalibrate RADARSAT images of tropical cyclones before applying the retrieval technique based on the inversion of scatterometer GMF CMOD5. Although the method avoids the use of the polarization ratio, which is often a source of errors, the authors show that the retrieved wind speed is in agreement with collocated model data for wind speeds up to 25 *m/s*. For higher wind speed large errors have been found, mainly due to saturation of the GMF and presence of heavy rain.

All authors of the above mentioned papers agree that the retrieval of the wind field in a tropical cyclone is still an open issue. Heavy rain, that in tropical cyclone conditions can reach up to 100 *mm/h*, and the saturation of the backscattered signal are the principal reasons for the underestimation of the actual wind speed in SAR retrieved wind speed.

4.7 References

Alpers W., and Bruemmer B., 1994, Atmospheric boundary layer rolls observed by the synthetic aperture radar aboard the ERS-1 satellite. *J. Geophys. Res.*, no. 99 (C6), pp. 12,613–12,622.

Bally P. and Fellah K., 1995, Evaluation of the accuracy of the Backscattering Coefficient Measurement in SAR data products. *ESA - Earth Sciences Division, technical note*.

Buck C.H., Suchail J.-L., Torres R., Zink M., 2000, ASAR Instrument Calibration. *ERS - ENVISAT Symposium*, Gothenburg, 16.-20.

Du Y., Vachon P. W., and Wolfe J., 2002, Wind direction estimation from SAR images of the ocean using wavelet analysis. *Canadian Journal of Remote Sensing*, no.28, pp.498−509.

Foster R. C., 2007, Boundary Layer Similarity Under an Axisymmetric, Gradient Wind Vortex. In submission.

Hasager, C. B., Dellwik, E., Nielsen, M., & Furevik, B., 2004, Validation of ERS-2 SAR offshore wind-speed maps in the North Sea. *International Journal of Remote Sensing*, no. 25, pp.3817−3841.

Hasselmann K., Raney R.K., Plant W.J., Alpers W., Shuchman R.A., Lyzenga D.R., Rufenach C.L., and Tucker M.J., 1985, Theory of synthetic aperture radar ocean imaging: a MARSEN view. *Journal of Geophys. Res*., vol. 90, no. C3, pp. 4659-4686.

He Y., Perrie W., Zou Q., and Vachon P. W., 2005, A New Wind Vector Algorithm for C-band SAR. *IEEE Trans. Geosci. Remote Sens*., no. 43(7), pp. 1453– 1458.

Hersbach, H., A. Stoffelen, and S. de Haan, 2007, An improved C-band scatterometer ocean geophysical model function: CMOD5. *Journal of Geophys. Res*., no. 112 (C3).

Horstmann J., Schiller H., Schulz-Stellenfleth J., and Lehner S., 2003, Global wind speed retrieval from SAR. *IEEE Trans. Geosci. Remote Sens*, no. 41(10),pp. 2277–2286.

Horstmann, J., Thompson, D.R., Monaldo, F., Graber, H.C. & Iris, S., 2005, Can Synthetic Aperture Radars be used to Estimate Hurricane Force Winds? *Geophysical Research Letters*, no. 32.

Katsaros K. B., Vachon P. W., Black P. G., Dodge P. P., Uhlhorn E. W., 2000, Wind Fields from SAR: Could They Improve Our Understanding of Storm Dynamics? *Johns Hopkins APL Technical Digest*, vol 21, No. 1.

Kerbaol V. and Chapron B., 1998, Analysis of ERS-1/2 Synthetic Aperture Radar Wave Mode Imagettes. *Journal of Geophys. Res.*, no. 103, pp 7833-7846.

Koch, W., 2004, Directional analysis of SAR images aiming at wind direction. *IEEE Transactions on Geoscience and Remote Sensing*, no.42, pp. 702−710.

Lehner S., Horstmann J., Koch, W., and Rosenthal W., 1998, Mesoscale wind measurements using recalibrated ERS SAR images. *Journal of Geophysical Research—Oceans*, no.103, pp.7847−7856.

Monaldo, F., 2000, The Alaska SAR demonstration and near-real-time synthetic 910 aperture radar winds. *Johns Hopkins Apl Technical Digest*, no.21, pp.75−79.

Monaldo, F.M. Thompson, D.R., Winstead, N.S., Pichel, W.G., Clemente-Colón, P. and Christiansen, M.B., 2005, Ocean wind field mapping from Synthetic Aperture Radar and its application to research and applied problems. *Johns Hopkins APL Technical Digest*, 26, 2, 102-113.

Morey S. L., Bourassa M. A., Davis X. J., O'Brien J. J., and Zavala-Hidalgo J., 2005, Remotely sensed winds for episodic forcing of ocean models. *Journal of Geophys. Res.*, no.110(C10).

Morrison I., Businger S., Marks F., Dodge P., Businger J. A., 2005, An Observational Case for the Prevalence of Roll Vortices in the Hurricane Boundary Layer. *Journal of the Atmospheric. Sciences*, vol.62, pp.2662-2673.

Perrie W., He Y., and Shen H., 2006, On Determination of Wind Vectors for C-band SAR for High Wind Speeds. *Proc. SEASAR workshop*, Frascati, Italy.

Perrie, W., W. Zhang, M. Bourassa, H. Shen, and P. W. Vachon, 2008, Impact of satellite winds on marine wind simulations. *Wea. Forecasting*, no. 23, pp. 290–303.

Plant, W.J., Relationship between stress wind and wave slope. *Journal of Geophys. Res*., vol. 87, no.C3, pp. 1961-1967, 1982.

Powell M. D., J. Peter Vickery, and Reinhold T. A., 2003, Reduced drag coefficient for high wind speeds in tropical cyclones. *Nature*, no. 422, pp. 279-283.

Quilfen Y., Chapron B., Elfouhaily T., Katsaros K. and Tournadre J., 1998, Observation of tropical cyclones by high-resolution scatterometry. *Journal of Geophys. Res.*, 103, C4, 7767-7786.

Shen H., Perrie W., and He Y., 2006, A new hurricane wind retrieval algorithm for SAR images. *Geophys. Res. Lett*., no.33.

Stoffelen, A., and D. Anderson, 1997, Scatterometer data interpretation: Estimation and validation of the transfer function CMOD4. *Journal of Geophys. Res*., no. 102(C3), pp. 5767–5780.

Stull R. B., 1998, An introduction to boundary layer meteorology. *Kluwer Accademic Publisher*.

Vachon P. W., Liu W. T., and Black P. G., 2002, Microwave remote sensing of tropical cyclones from space. *J. Oceanogr*., no. 58, pp. 137–151.

Wright J. W., 1978, Detection of ocean waves by microwave radar; The modulation of short gravity-capillary waves. *Boundary-Layer Meteorology*, vol 13, no. 1-4.

Zink, M.; Torres, R.; Buck, C.H.; Rosich, B.; Closa, J., 2002, Calibration and early results of the ASAR on ENVISAT. *Proc. IGARSS 2002 IEEE*, vol. 1, pp. 596- 598.

5 Data set description

Because of their all-weather capability and wide swath coverage space borne radars are of particular interest for the study of tropical cyclones. One of the main advantages of these sensors, e.g. scatterometers, SARs and altimeters, is the penetration of dense clouds coverage and weak influence of rain. Hence such radars can measure with rather high precision the NRCS of the sea surface.

This chapter describes the different types of data used in the present study. In the first part a detailed introduction to ENVISAT ASAR Wide Swath mode (ScanSAR) data, RADARSAT Wide Swath mode data and ERS-2 wave mode data is given, followed by a description of ERS-2 scatterometer and altimeter data used for validation. The performance and limitation of each data set is also addressed.

5.1 Remote sensing data

In this paragraph the remote sensed data used for the study are described. All these data have been acquired using satellite-borne radars. Radar sensors can be separated in two categories: nadir looking radars such as altimeters, and side looking radars such as SARs and scatterometers.

Altimetry sensors basically determine the distance from the satellite to the target surface by measuring the satellite-to-surface round-trip time of a radar pulse. Additionally, analysis of the intensity and shape of the returned pulse allows retrieving information on sea state and wind speed. To obtain a high vertical resolution these radars are operated with very short pulses. Such sensors have a high vertical resolution, in the order of centimetres [ENVISAT radar altimeter handbook], but have a small footprint on the illuminated surface due to the short pulse length.

Satellite scatterometers are side looking non coherent radars that accurately measure the power of the pulse scattered back to the antenna. They have been originally designed to map wind speed and direction over the oceans, but they also measure various land, sea and ice variables. To achieve a high radiometric resolution pulses received over a wide area are averaged. This results in a spatial resolution of only several kilometres.

As detailed in chapter 2, SAR sensors are coherent systems designed to image the earth surface with high spatial resolution. The last generation SAR system, like TerraSAR-X, can achieve a sub meter resolution.

In Tab. 5-1 the key characteristics of the present satellite missions equipped with radar sensors for the monitoring of the ocean surface are listed.

5.1.1 ENVISAT ASAR wide swath data

The European satellite ENVISAT was launched on March 1st, 2002 into a Sun-synchronous polar orbit to provide measurements of the atmosphere, ocean, atmosphere, and sea ice. The satellite, equipped with ten different sensors, allows the monitoring of sea surface temperature, water vapour, cloud top height, earth radiation budget, and the sea state conditions. The satellite has been positioned in an orbit similar to the ERS-2 satellite to allow the acquisition of data over the same area with half an hour time shift.

	Waveband (central frequency) [GHz]	**Polarization**	**Radiometric accuracy** [dB]	**Incidence angle range** [deg]	**Resolution** [m x m]	**Swath width** [km]
ENVISAT ASAR	C (5.3)	VV,HH	1.5-3.5	19-45	Image Mode 30 x 30	100
					Wide Swath 150 x 150	400
ERS 1-2 AMI	C (5.3)	VV	2.5	20 - 26	30 x 30	100
RADARSAT-2	C (5.3)	VV,HH	1.	20-49	From 3x 3 to 100 x 100	
RADARSAT	C (5.3)	HH	1.5-3.5	20 - 49	From 8x8 to 100x100	From45 to 500
TerraSAR-X	X (9.65)	VV,HH	1.5	20 - 45	From 1 to 16	From 10 to 100
Sea Winds Scatterometer	Ku (13.4)	VV,HH	0.2	46 - 54	12.5 x 12.5	1800
ASCAT Scatterometer	C (5.3)	VV	0.5			500 + 500
ERS Scatterometer	C (5.3)	VV	0.2	18 - 59	2500 x 2500	500
ERS altimiter	Ku(13.8)	n.a.	0.4	Nadir	16000 to 20000	n.a.
ENVISAT altimiter	Ku(13.575), S(3.2)	n.a.	0.4	Nadir	2000	n.a.
Topex Poseidon, Jason 1/2	Ku(13.6), C(5.3)	n.a.	0.2	Nadir	3000 to 5000	n.a.

Tab. 5-1: Key characteristics of Synthetic Aperture Radar and Scatterometer instruments.

ENVISAT carries a SAR instrument, called “ASAR” operating in C-band (5.331 *GHz*). The main feature of ASAR is the active phased array antenna that offers the possibility to operate in a number of different modes with different incidence angles and polarizations. ASAR can acquire data in the so called ScanSAR mode, in which several beams are combined to generate an image of 400 *Km* width (Wide Swath), with 150 *m* resolution and 75 *m* pixel size (Fig. 5-1). The incidence angles in ScanSAR mode vary between 19° and 45°. A constraint in the use of ASAR Wide Swath mode for wind speed retrieval at medium to high wind speed and with high spatial variation of the wind field is set by the saturation of the analog to digital converter for small incidence angles.

In ScanSAR mode a large part of a tropical cyclone can be imaged synoptically allowing the analysis of the storm structure and the associated mesoscale features (Fig. 5-2).

5.1.2 RADARSAT-1 scan SAR images (SWA)

The Canadian satellite RADARSAT-1 equipped with a SAR sensor was put in a sun- synchronous orbit on November 4, 1995 at 798 *Km* above the Earth. The SAR sensor works at 5.3 *GHz* (C-band) in HH polarization. Like the ENVISAT ASAR sensor RADARSAT-1 is able to operate in different

modes (Fig. 5-3) with image swath ranging from 45 *Km* to 500 *Km* with a resolution from 8 *m* to 100 *m*. The scanning SAR (ScanSAR) wide mode (SWA) of RADARSAT-1 provides coverage of 500 *Km* nominal ground swaths at incidence angles between 20° and 49°, with a spatial resolution of 100 *m* and a pixel size of 50 *m* (Fig. 5-4).

RADARSAT images are acquired with HH polarization and no geophysical model function, to retrieve wind fields for such polarization has been developed. Some studies to adapt the GMF for VV polarization, through the use of an empirically determined multiplication factor, have been done [Elfouhaily, 1997],[Thompson et al., 1998],[Vachon et Dobson, 2000],[Horstmann et al., 2000], [Mouche et al., 2005] but the results are under discussion and a consensus has not been found yet. In this study RADARSAT images are used only for the analysis of atmospheric features, e.g. wind streaks, associated with tropical cyclones.

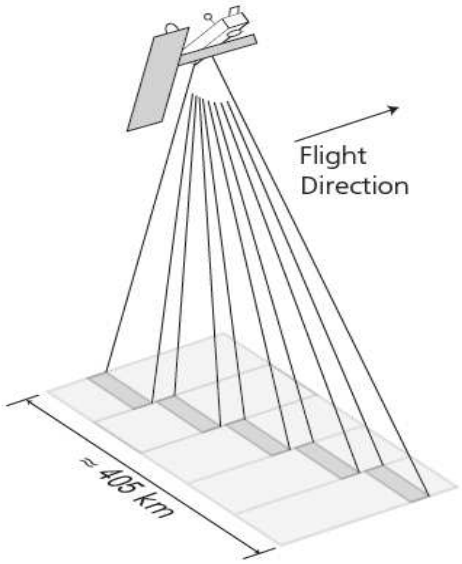

Fig. 5-1: ENVISAT ASAR acquisition geometry in Wide Swath Mode, (image courtesy ESA).

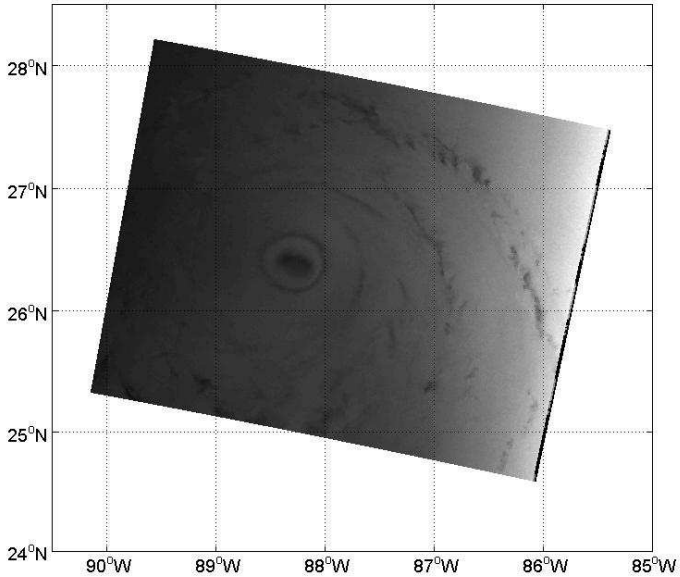

Fig. 5-2: ASAR ScanSAR Image of hurricane Katrina acquired on 28 Aug. 2005 15:51, over the Gulf of Mexico. Coverage is about 400 km x 400 Km.

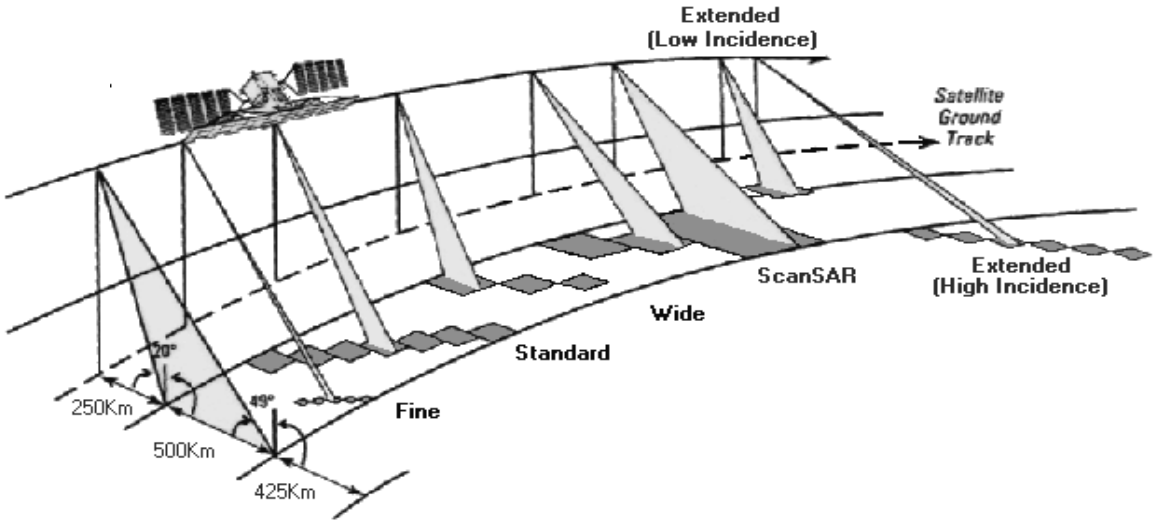

Fig. 5-3: RADARSAT-1 acquisition modes.

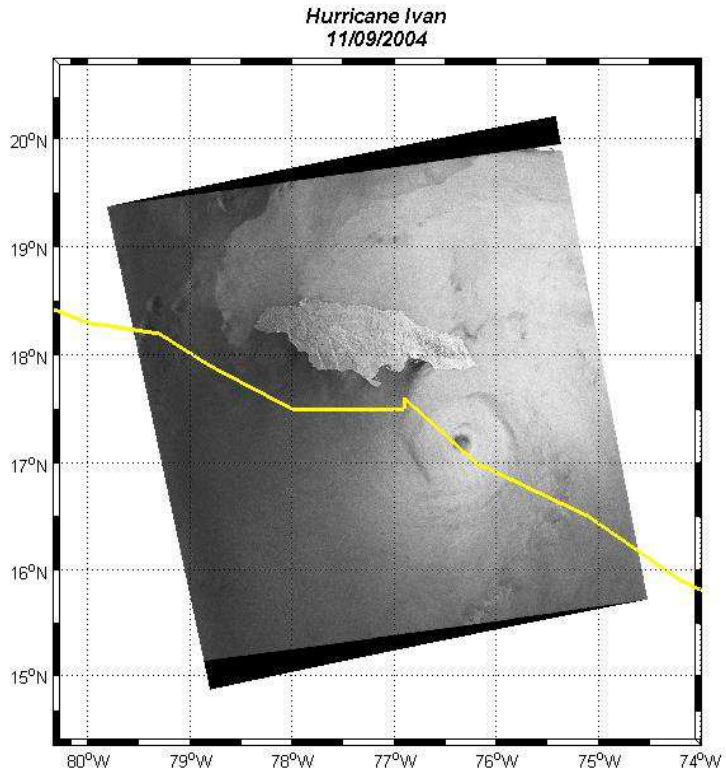

Fig. 5-4: RADARSAT Image of hurricane Ivan acquired on 11 Sep. 2004 23:13 UTC. Yellow line represents the storm track.

5.1.3 AMI SAR data

The European Remote Sensing satellite ERS-2 is the follow-on mission of ERS-1 and was launched in April 1995 [ESA Earthnet on line]. The satellite is still operating and is flying in a sun-synchronous polar orbit at 785 *Km* height and 98.5° inclination.

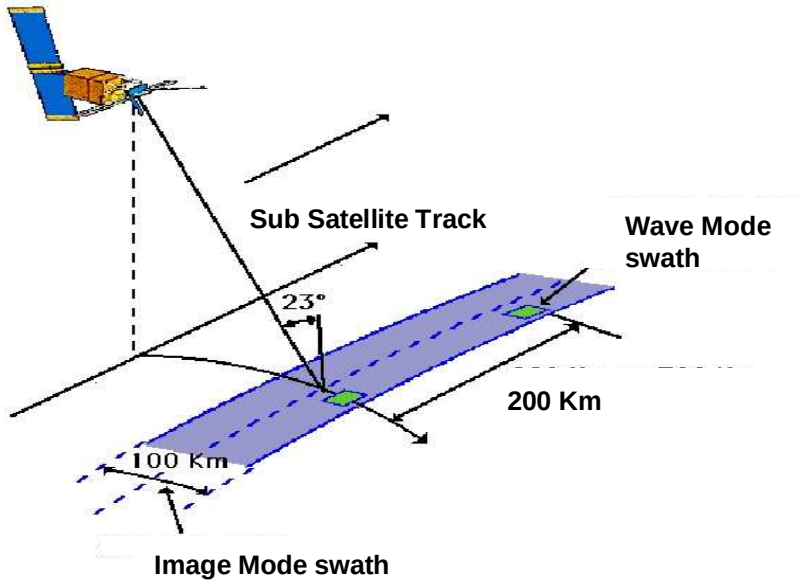

Fig. 5-5: ERS-2 SAR Wave Mode Data acquisition geometry

At the time of their launch the ERS satellites represented the most sophisticated Earth observation platform ever developed and launched in Europe. Both satellites were designed to acquire data for a large variety of users and applications.

In this study data acquired with the Active Microwave Instrument (AMI) are used. The instrument incorporates two radars, a SAR and a Scatterometer for Wind Mode operation. Due to operational requirements the two modes are mutually exclusive, but Wind and Wave Modes are also capable of interleaved operation, in so-called 'Wind/Wave Mode' (Fig. 5-5).

To provide a global and continuous coverage of the ocean the SAR provides 5 *Km* x 10 *Km* images, also called Wave Mode Images, or imagettes at intervals of 200 *Km* along the satellite track (Fig. 5-6). The relatively low data rate allows on-board data storage and subsequent downlink when a receiving antenna is in line of sight. Wave Mode data are acquired at a nominal incidence angle of 23°, with a resolution of 20 *m* in range and 4 *m* in azimuth. The size of an imagette in azimuth (along track) is 5.12 *Km* (320 pixels), while in range (across track) it is approximately 10 *Km* (600 pixels).

ESA delivers as standard product derived from Wave Mode data coarsely gridded image power spectra, so called UWA spectra [G. Brooker, 1995]. These data are distributed to weather centres in real time and used for ocean wave mode validation and assimilation.

Using the BSAR processor developed at DLR/DFD Wave Mode raw data have been processed to single look complex SAR image data. In total more than 800,000 imagettes were processed, covering the period from January 1999 to December 2000. More technical details about the reprocessing of the data can be found in Lehner et al., (2000).

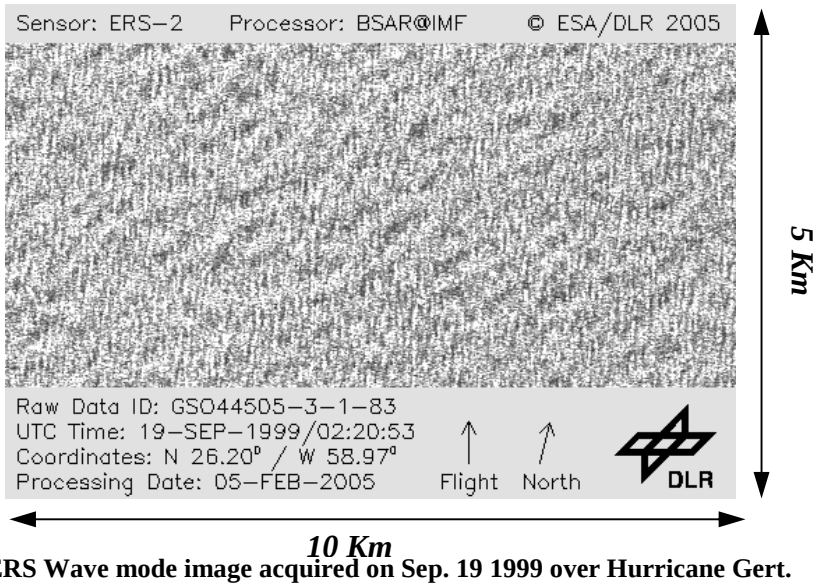

Fig. 5-6: ERS Wave mode image acquired on Sep. 19 1999 over Hurricane Gert.

5.1.4 AMI scatterometer data

Spaceborne scatterometers are radars originally developed to obtain information on wind speed and direction over the sea surface. The AMI Scatterometer consists of three antennas, one pointed sideways and two at ± 45°.

The antennas illuminate a swath of 500 *Km* and are processed to a pixel size of 25 *Km* both in range and in flight direction. A wind field retrieved using the AMI scatterometer on Oct. 24 2005 over Gulf of Mexico is shown In Fig. 5-7.

As Wave Mode data are available at the same time and location within the larger ERS-2 Scatterometer swath, for every Wave Mode image a precisely collocated Scatterometer wind vector is associated. AMI Scatterometer data have been used to validate the calibration of Wave Mode data and to compare the SAR retrieved wind speed. The scatterometer wind fields used in this study have been processed and delivered by the French Processing and Archiving Facility (F-PAF) [Pouliquen and Harscoat, 1994].

5.1.5 ERS-2 RADAR altimeter data

The ERS-2 Radar Altimeter is a Ku-band (13.8 GHz) nadir-pointing active microwave sensor that allows the measurements of significant wave height over the ocean with a radar footprint that varies with the sea state from two to ten kilometers [http://earth.esa.int/missions/]. The standard delivered product consist of one measurement every second, that corresponds to 7 *Km* in distance, along the satellite orbit. Altimeter estimates of significant wave height, provided by the Altimeter Data Processing System (ADP) at GeoForschungsZentrum Potsdam (GFZ), are used to compare SAR measurements and to improve the detection of the early stage of storms in the open ocean.

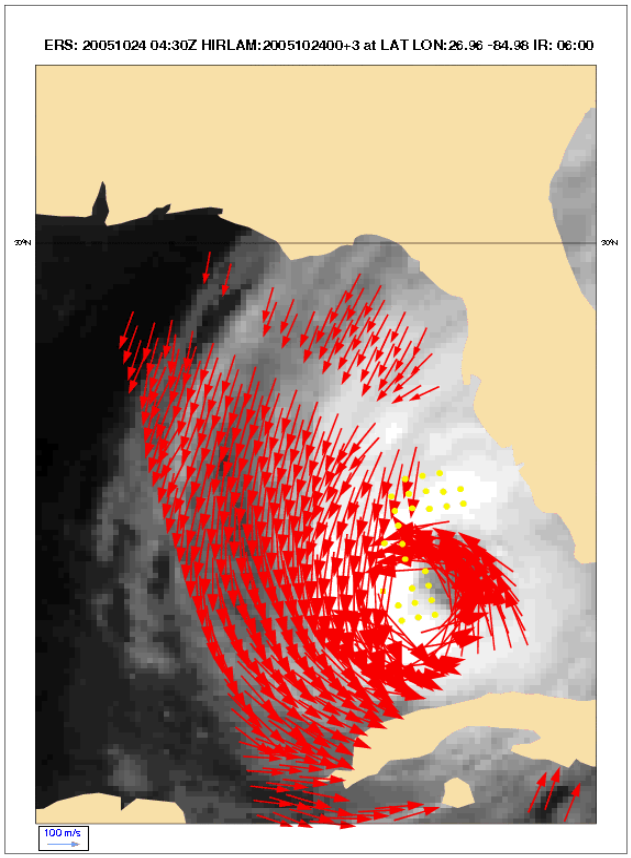

Fig. 5-7: ERS Scatterometer wind field acquired on Oct. 24 2005 over the Gulf of Mexico (Hurricane Wilma) (image courtesy ESA).

5.2 References

Brooker G., 1995, UWA processing algorithm specification Version 2.0. *ER-TN-ESA-GS-0342*, Issue 1.0 Rev 0.

Elfouhaily T., 1997, Physical modelling of electromagnetic backscatter from the ocean surface; Application to retrieval of wind fields and wind stress by remote sensing of the marine atmospheric boundary layer. *Dépt. d'Océanogr. Spatiale, l'Inst. Français Rec. l'Exploitation Mer (IFREMER)*, Plouzane, France.

Envisat radar altimeter handbook: http://envisat.esa.int/handbooks/ra2-mwr/

ESA Earthnet on line: http://earth.esa.int/missions/

Horstmann J., Koch W., Lehner S., Tonboe R., 2000, Wind retrieval over the ocean using synthetic aperture radar with C-band HH polarization. *IEEE Trans. Geosci. Remote Sens.*, vol. 38, no. 5, pp. 2 122–2 131.

Lehner, S.; Schulz-Stellenfleth, J.; Schattler, B.; Breit, H.; Horstmann, J., 2000, Wind and wave measurements using complex ERS-2 SAR wave mode data. *IEEE Transactions on Geoscience and Remote Sensing*, vol. 38, issue 5, pp. 2246-2257.

Migliaccio M., 2003, Sea Scatterometry. In “Remote Sensing of Atmosphere and Ocean from Space: Models, Instruments and Techniques”. *Springer Netherlands*.

Mouche A., Hauser D., Daloze J.F., Gurin C., 2005, Dual Polarization Measurements at C-Band over the Ocean: Results from Airborne Radar Observations and Comparison with ENVISAT ASAR data. *IEEE Trans. Geosci. Remote Sens.*, vol. 43, no. 4, pp. 753 – 769.

National Data Buoy Centre: http://www.ndbc.noaa.gov/

Niedermeier A., Hoja D. and Lehner S., 2005, Topography and morphodynamics in the German Bight using SAR and optical remote sensing data, *Ocean Dynamics*, vol. 55, no. 2 .

Pouliquen, S.; Harscoat, V., 1994, The French processing and archiving facility: Overview and status. *Proc. OCEANS apos;94*, Volume 1, pp. 895 - 899.

Rentsch M., Braun A., Helm A., Schone T., 2000, Operational Altimetry at GFZ - From ERS-2 to ENVISAT. *Proceedings of the ESA ERS/ENVISAT Symposium*.

Schulz-Stellenfleth J. and Lehner S., 2004, Measurement of 2D Sea Surface Elevation Fields Using Complex Synthetic Aperture Radar Data. *IEEE Trans. Geosci. Remote Sensing*, vol. 42, no. 6.

Thompson, D. R., Elfouhaily, T. M., and Chapron, B., 1998, “Polarization Ratio for Microwave Backscattering from the Ocean Surface at Low to Moderate Incidence Angles. *Proc. 1998 Int. Geosci. and Remote Sensing Symp*., Seattle, Washington, pp. 1671–1676.

Ulaby F. T., Moore R. K., and Fung A.K., 1982, Microwave Remote Sensing: Active and Passive, Vol. II -- Radar Remote Sensing and Surface Scattering and Emission Theory. *Addison-Wesley, Advanced Book Program, Reading*, Massachusetts.

Vachon P. W. and Dobson F. W., 2000, Wind retrieval from RADARSAT SAR images: Selection of a suitable C-band HH polarization wind retrieval model. *Can. J. Remote Sensing*, vol. 26, no. 4, pp. 306–313.

6 Features Analysis of tropical cyclone images

This chapter describes the estimation of some characteristic tropical cyclones parameters like eye size and shape, radius of maximum wind speed and wind streaks from SAR images. These parameters are key input for a parametric model of tropical cyclones used in this study. A technique based on wavelet analysis is used to estimate the eye size and shape, while the wind streaks are analysed making use of a Fourier Transformation. A dataset of fourteen SAR images selected from the ENVISAT ASAR and Radarsat-1 archives have been selected for the study.

6.1 Tropical cyclones analysed

The images selected for this study were chosen from the ENVISAT ASAR and RADARSAT-1 wide swath archives if the eye of the tropical cyclone, needed for the analysis, is visible. A total of 14 images were selected for the analysis. In Tab. 6-1 the key characteristics of the tropical cyclones at the time of the SAR acquisition are given.

6.2 Eye size and shape

Tropical cyclones, in the mature stage, are characterized by the presence of a well defined eye at the geometric centre of the storm. The eye of a tropical cyclone is a region of mainly low wind speed and very little rain. It can be clear or filled by low and mid-level clouds (a filled eye), or it may be obscured by the central dense overcast.

The size of a tropical cyclone eye can vary between 5 *Km* and 50 *Km* [Kimball, 2004]. For very intense tropical cyclones a phenomenon called ‘Eyewall Replacement’ can occur. In such cases, some of the outer rainbands may strengthen and organize into a ring of thunderstorms, the so called ‘Outer Eyewall’, that slowly moves inward acquiring moisture and angular momentum from the inner eyewall until the latter collapses. During this phase usually the storm weakens, to eventually re-intensify when the outer eyewall replaces the inner one completely.

As the ocean surface of the eye area is relatively smooth, the SAR backscattered signal will be weak when compared to the surrounding area which is characterized by the strongest wind speed in the storm. The tropical cyclone’s eye will appear in the SAR image as a dark area with elliptical shape. Fig. 6.1 shows as an example the eyes of four tropical cyclones. The size of each image is 60 *Km* x 60 *Km*. The top left image shows the eye (32 *Km* major axis) of hurricane Katrina (2005) when an eye replacement was in progress. The top right image shows the small eye (12 *Km* major axis) of typhoon Kiko (2004), while the lower left and lower right images show the eyes of hurricanes Danielle (1998) (38 *Km* major axis) and Lili (2002) (20 *Km* major axis) respectively.

6.2.1 Eye detection using wavelet analysis

The characteristic appearance in SAR images of the tropical cyclone eye makes possible to detect its size, shape and orientation using an edge detection technique. Hereafter the image of the hurricane Lili’s eye will be used to show the various processing steps (see Fig 6.2).

In this study the approach proposed by Du and Vachon (2003) has been followed, and applied for the first time to ENVISAT ASAR images [Reppucci et al., 2008]. As first step a wavelet analysis is

	Sensor	Image centre Lat, Lon	Image acquisition Time (UTC)	Max. Wind Speed	Central Pressure	Cat
Hurricane Katrina	ENVISAT ASAR	26,22°N - 87,8°W	28-08-05 - 15:50	70 m/s	905 mb	V
Hurricane Rita	ENVISAT ASAR	24,08°N - 86,00W°	22-09-05 - 03:45	75 m/s	897 mb	V
Typhoon Kiko	ENVISAT ASAR	17,99°N 131,00°E	09-09-05 - 01:11	40 m/s	955 mb	I
Typhoon Kiko	ENVISAT ASAR	25,73°N 123,35°E	11-09-05 - 01:46	55 m/s	945 mb	II
Typhoon Songda	ENVISAT ASAR	28,7°N 128,54°E	06-09-04 - 13:23	45 m/s	940 mb	II
Typhoon Marce	ENVISAT ASAR	25,36°N 121,83°E	25-08-04 - 15:21	33 m/s	980 mb	I
Hurricane Frances	ENVISAT ASAR	29,43°N 84,20°W	06-09-04 - 15:38	23 m/s	982 mb	TS
Hurricane Wilma	ENVISAT ASAR	24,64°N 84,68°W	24-10-05 - 03:39	49 m/s	958 mb	II
Typhoon Talim	ENVISAT ASAR	21,20°N 128,06E°	30-08-05 - 01:24	63 m/s	925 mb	IV
Hurricane Danielle	RADARSAT-1	30,48°N 72,87°W	31-08-98 - 10:52	46 m/s	977 mb	II
Hurricane Humberto	RADARSAT-1	39,44°N 56,80°W	26-09-01 - 21:41	40 m/s	977 mb	I
Hurricane Lili	RADARSAT-1	29,13°N 86,76°W	02-10-02 - 11:46	47 m/s	971 mb	II
Typhoon Sinluka	RADARSAT-1	30,17°N 125,44°E	05-09-02 - 21:38	45 m/s	950 mb	II
Hurricane Floyd	RADARSAT-1	33,99°N 76.21°W	15-09-99 - 11:08	51 m/s	943 mb	III

Tab. 6-1: Key characteristic of Tropical Cyclones analysed as reported by HRD and JMA.

performed in order to remove the high frequency features due to the noise that can affect the performance of the edge detection.

A wavelet transform provides a time-frequency representation of a signal. Applying wavelet analysis for edge detection gives the possibility of choosing the size of the details that will be detected. When used with SAR images this allows filtering out the high frequency features that are associated with local noise. The size of the detected details is set by the wavelet scale. Using as basis the 'Daubechies D4' wavelet with a level of approximation equal to 5 corresponds to look at features with a spatial scale of 2.4 *Km* in the case of ASAR images and 1.6 *Km* in the case of RADARSAT-1 images. At this scale the eye of the tropical cyclones will be detected as a low frequency feature. Fig. 6-2 shows the eye of the hurricane Lili after the processing using the aforementioned technique. After the filtering the SAR image is transformed into polar coordinates (Fig. 6-3).

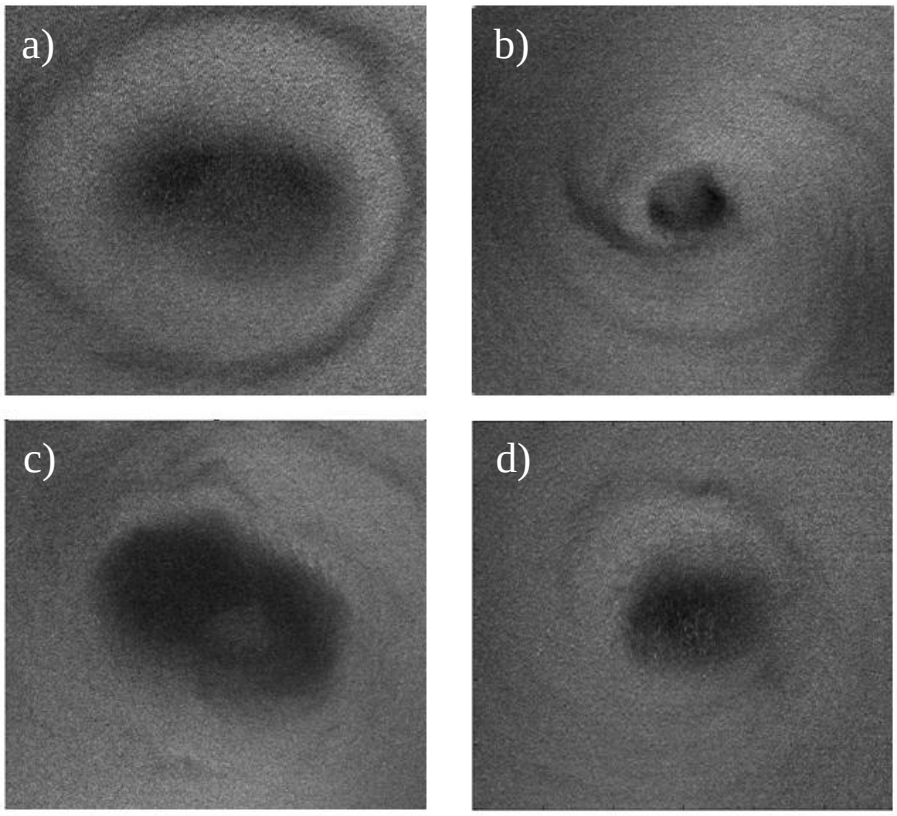

Fig. 6-1: Tropical cyclone eyes of hurricane Katrina (a), typhoon Kiko (b), hurricane Danielle (c) and hurricane Lili (d). Each image is 60 Km x 60 Km.

Fig. 6-2: Eye of the hurricane Lili after the processing using wavelet analysis.

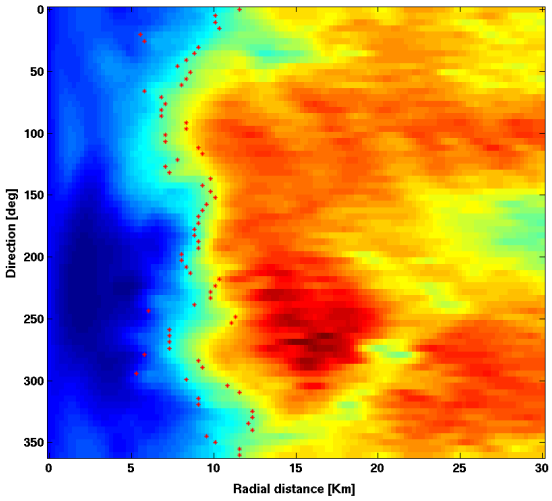

Fig. 6-3: The eye of Lili transformed into polar coordinates. Pixel are coloured according to their intensity value.

The maximum radiometric gradient is then computed along the radial directions with a step size of 1 degree. In a final step the average value of the maximum radiometric gradient is used as threshold to estimate the extent of the eye area. Fig. 6-4 shows the resulting eye area for the tropical cyclones shown in Fig. 6-1. In Tab. 6-2 the results of the procedure applied to the whole dataset of Tab. 6-1 is presented.

It should be noted that following this approach the area of the eye is estimated objectively, i.e. the threshold is estimated for each case without using other external information.

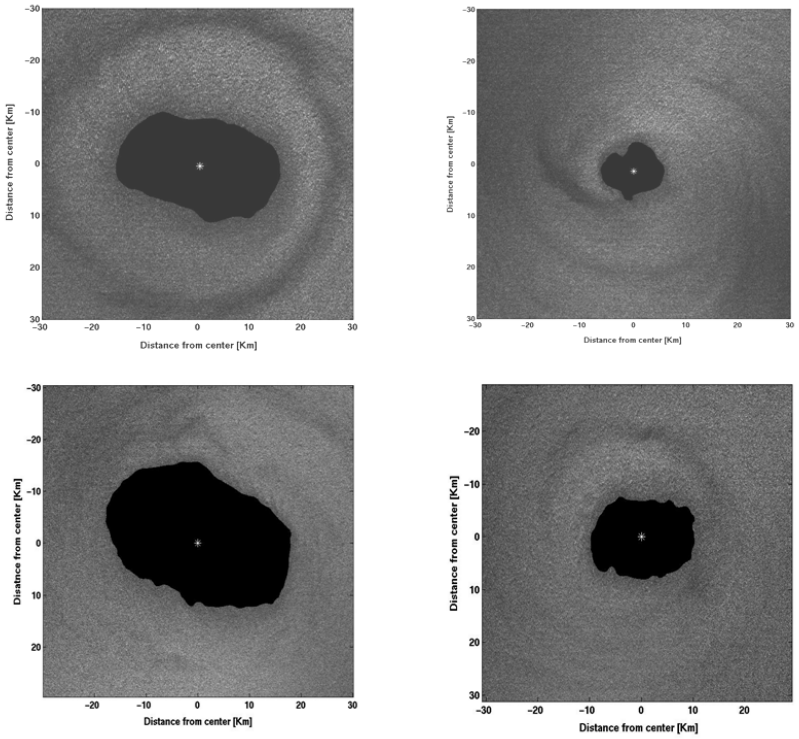

Fig. 6-4: Estimation of the eye's area for the tropical cyclones shown in Fig. 6.2., with an asterisk denoting the eye's centre.

Tropical Cyclone Name (number)	Area	Major Axis	Min Axis	Eccentricity	Orientation
Hurricane Katrina (1)	484,24	32,73	19,06	0,82	101,82°
Typhoon Kiko 09 (2)	89,73	11,96	9,87	0,56	79,53°
Typhoon Kiko11 (3)	245,67	19,89	15,18	0,65	88,65°
Typhoon Songda (4)	225,58	27,80	12,41	0,89	116,26°
Typhoon Marce (5)	749,12	46,71	21,75	0,88	97,77°
Hurricane Frances (6)	904,2	40,02	30,39	0,65	83,85°
Hurricane Wilma (7)	4376,3	87,6	64,12	0,68	120,29°
Hurricane Danielle (8)	736,77	38,21	24,69	0,76	114,79°
Hurricane Humberto (9)	255,47	23,018	14,34	0,78	114,62°
Hurricane Lili (10)	251,08	20,94	15,42	0,68	85,37°
Typhoon Sinluka (11)	4785,2	107,42	57,88	0,84	97,62°
Hurricane Floyd (12)	2579,2	67,94	49,094	0,69	111,99°
Mean Values **Standard deviation**	1306.9 1668.2	43.68 29.42	27,85 18.72	0,73 0,1	

Tab. 6-2: Eye size and shape parameters.

6.2.2 Eye size, shape and centre location

Once the extent of the tropical cyclones has been determined different parameters can be computed. The size of the eye is estimated multiplying the number of pixels belonging to the eye by the pixel size.

The centre of the tropical cyclone (asterisks in Fig. 6-4) is estimated computing the centre of mass of the eye region (first moment). The reference ellipse is calculated as the ellipse that has the same normalized second central moments as the eye region [Jain, 1999]. The eccentricity can be used to estimate the shape of the eye, i.e. the smaller the eccentricity is the closer to a circle is the eye area. The orientation is given as the direction in degree between a vertical axis in the image and the major axis of the reference ellipse. Fig. 6-5 shows the reference ellipse calculated for the eye of the hurricane Lili. In Fig. 6-6 to Fig. 6-8 the histograms of the parameters estimated from the dataset reported in Tab. 6-2 are plotted.

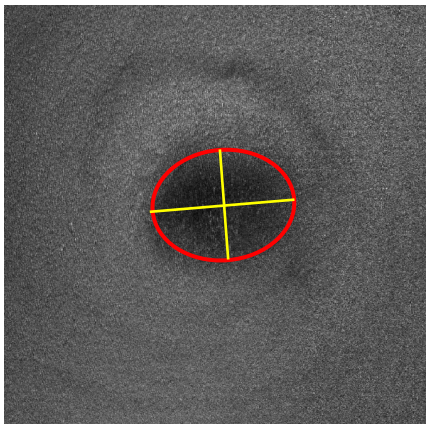

Fig. 6-5: Reference ellipse for the eye of hurricane Lili.

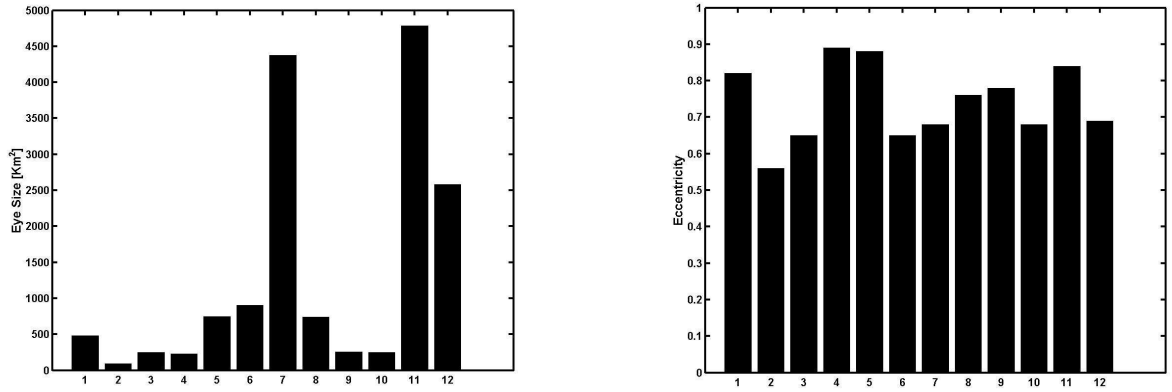

Fig. 6-6: Histograms of eye size (left) and eye eccentricity as estimated from the dataset of Tab. 6-2.

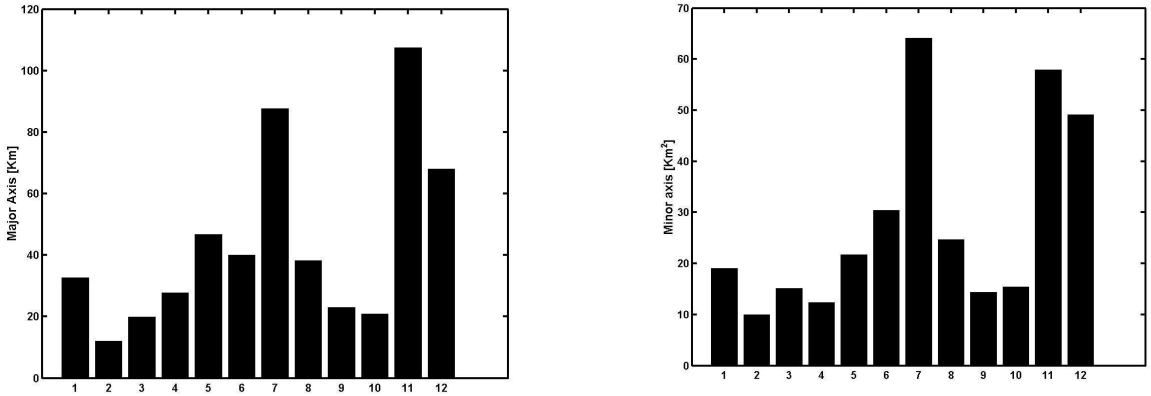

Fig. 6-7: Histograms of major (left) and minor (right) axis eyes as estimated from the dataset of Tab. 6-2.

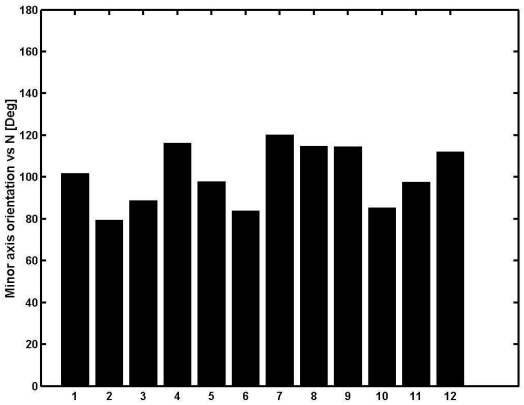

Fig. 6-8: Histograms of minor axis orientation with respect to the North as estimated from the dataset of Tab. 6-2.

6.3 Estimation of the radius of maximum wind speed

The radius of maximum wind speed is the region at the boundary of the tropical cyclone eye affected by the highest wind speed. This parameter is one of the inputs for the Holland parametric model used in the following analysis. In the SAR image this area will appear as a ring much brighter than the surroundings. The radius of maximum wind speed is estimated from SAR images using two perpendicular profiles, in the range and azimuth directions, passing through the tropical cyclone centre.

Fig. 6-9 shows a cut through the centre of the eye of the hurricane Katrina in the range (look) direction. In this direction it is possible to observe a strong ramp in the brightness values introduced by the incidence angle variation across the swath. To remove the contribution due to the incidence angle variation a polynomial of first degree has been fitted to the data (dash-dotted line in Fig. 6-9) and subtracted to obtain the result shown in Fig. 6-10. In a following step the radius of maximum wind speed is estimated measuring the distance between the centre of the tropical cyclone and the abscissa of the point with the highest brightness value (see black arrow in Fig. 6-10).

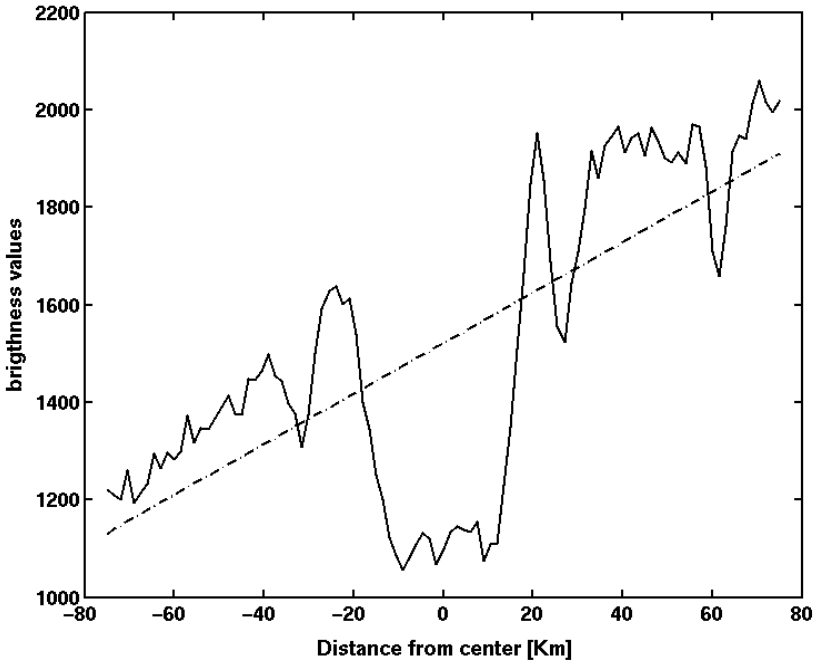

Fig. 6-9: Cut through the eye of hurricane Katrina in the range direction.
The dash-dotted line represents the first order polynomial fitting to the SAR measurements.

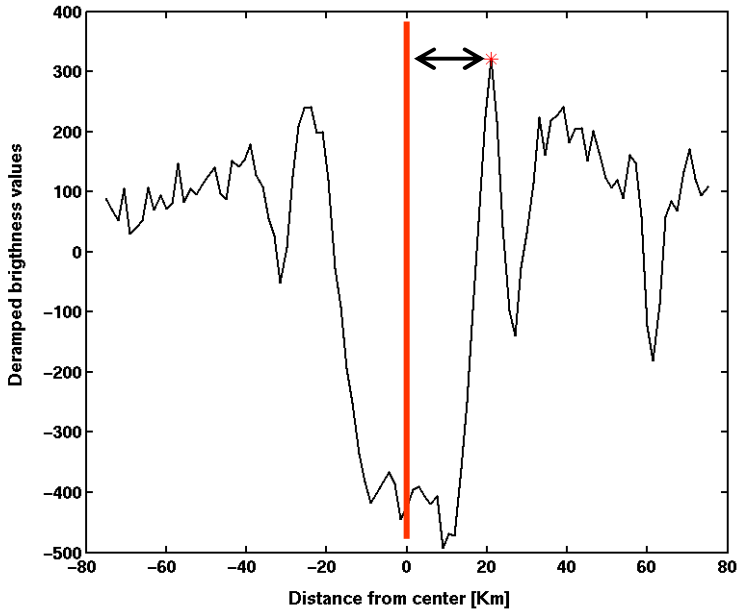

Fig. 6-10: Cut through the eye of hurricane Katrina in the range direction after deramping. The red asterisk represents the point with highest brightness. The black arrow represents the estimated radius of maximum wind speed.

In the azimuth direction, as the variation in the SAR measurements are only due to changes in the wind field the deramping step it is not needed (Fig. 6-11). Assuming that the wind direction along the two cuts it is not changing, the R_{MW} is then computed finding the maximum in the profile (black arrow in Fig. 6-11). In Tab. 6-3 the values of R_{MW} as estimated in the two directions and the mean value are reported.

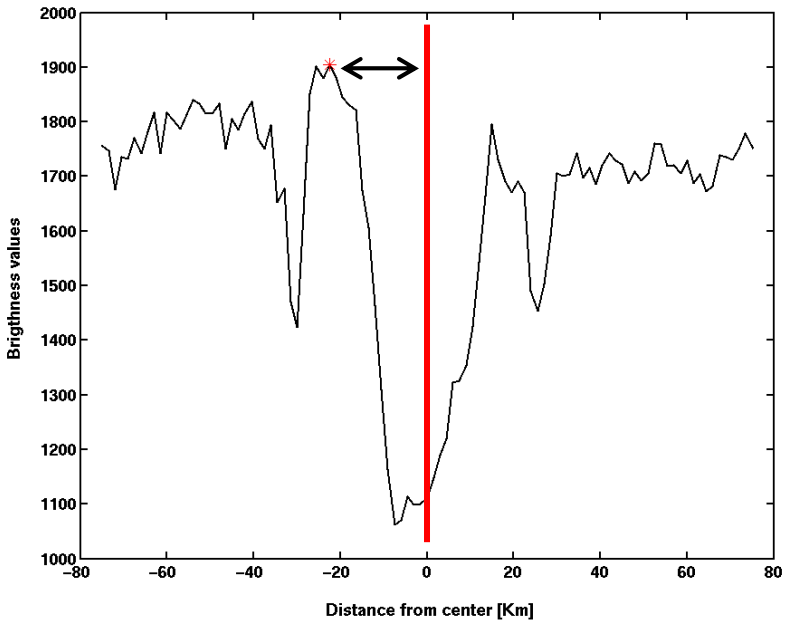

Fig. 6-11: Cut through the eye of hurricane Katrina in the azimuth direction. The red asterisk represents the point with highest brightness. The black arrow represents the estimated radius of maximum wind speed.

Tropical Cyclone	R_{MW} range [*Km*]	R_{MW} azimuth [*Km*]	R_{MW}Mean [*Km*]
Katrina	21	22.5	21.75
Kiko 09	9.0	10.5	9.75
Kiko11	15	12	13.5
Songda	15	13.5	14.25
Marce	43.5	22.5	33
Frances	43,5	42	42.75
Wilma	51	43	47
Danielle	28,5	30	29.25
Humberto	21	25.5	23.25
Lili	13.5	16.5	15
Sinluka	75	61.5	68.25
Floyd	45	67.5	56.25

Tab. 6-3: Estimated radius of maximum wind speed in range direction and in azimuth direction.

6.4 Atmospheric boundary layer roll analysis

The marine atmospheric boundary layer is part of the atmosphere that is in direct contact to the ocean. It is in this region that ocean and the atmosphere exchange heat, moisture and moment via turbulent transport. The turbulent flux is organized in convective cell and rolls. Atmospheric boundary layer rolls (or convective rolls) are helical circulation patterns in the marine atmospheric boundary layer which are superimposed on the mean wind field (primary flow) [Stull, 1998]. These rolls modulate the short scale roughness due to primary flow, resulting in lines of enhanced and decreased backscatter in the SAR image. The direction of the roll is parallel to the mean boundary layer wind shear vector [Lehner et al., 1998].

In tropical cyclone conditions the inhomogeneous turbulence in the boundary layer led, mainly, to the formations of roll vortices [Foster, 2005]. Fig. 6-12 shows an ENVISAT ASAR image acquired over typhoon Kiko on Sept. 9, 2005. The image contains signatures of roll vortices. The wavelength of these rolls is on the order of 700 m to 1100 m. Some scientists [Foster, 2007], [Morrison et al., 2005] assume that the wavelength of these rolls is related to boundary layer depth, which would be valuable information to be deduced from the SAR image.

Following the approach explained in section 4.4, an analysis of the wavelengths of the SAR detected boundary layer rolls has been conducted on the tropical cyclone dataset reported in Tab. 6-1.

Fig. 6-13 and Fig. 6-14 show two examples of the retrieved boundary layer rolls (a) and the relative histograms (b) for the hurricane Danielle (1998) and the typhoon Songda (2004), respectively. Tab. 6-4 shows the result of the analysis of boundary layer rolls from the dataset described in Tab. 6-1. For each tropical cyclone the number of detected boundary layer rolls as well as the mean value of the wavelength and the standard deviation is given. The histograms of the results given in Tab. 6-4

are shown in Fig. 6-15. The estimated wind directions will be used in chapter 7 as input for the algorithm used to retrieve tropical cyclone wind speed fields.

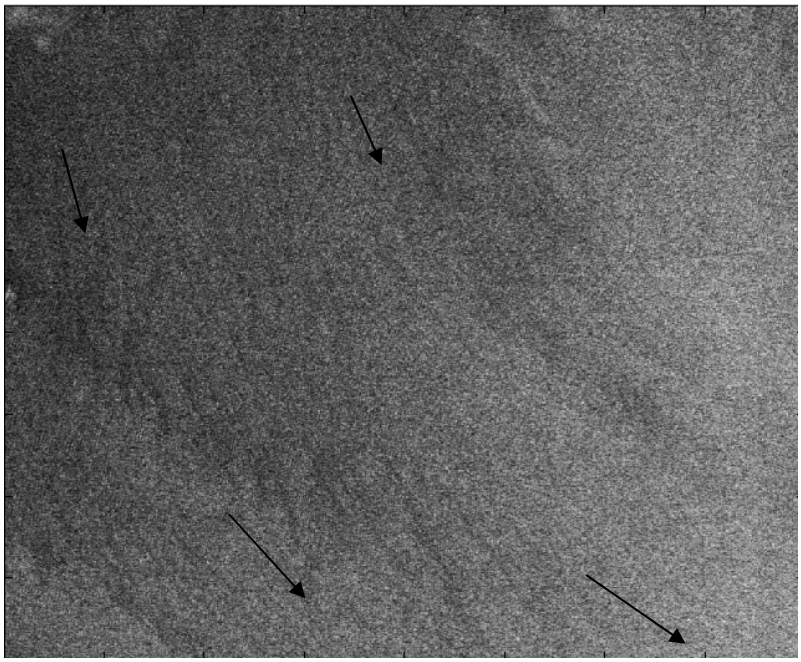

Fig. 6-12: Sub image of 30 Km x 30 Km extracted from the ASAR image of typhoon Kiko (2005), showing the imprint of wind streaks. The black arrows show the wind direction.

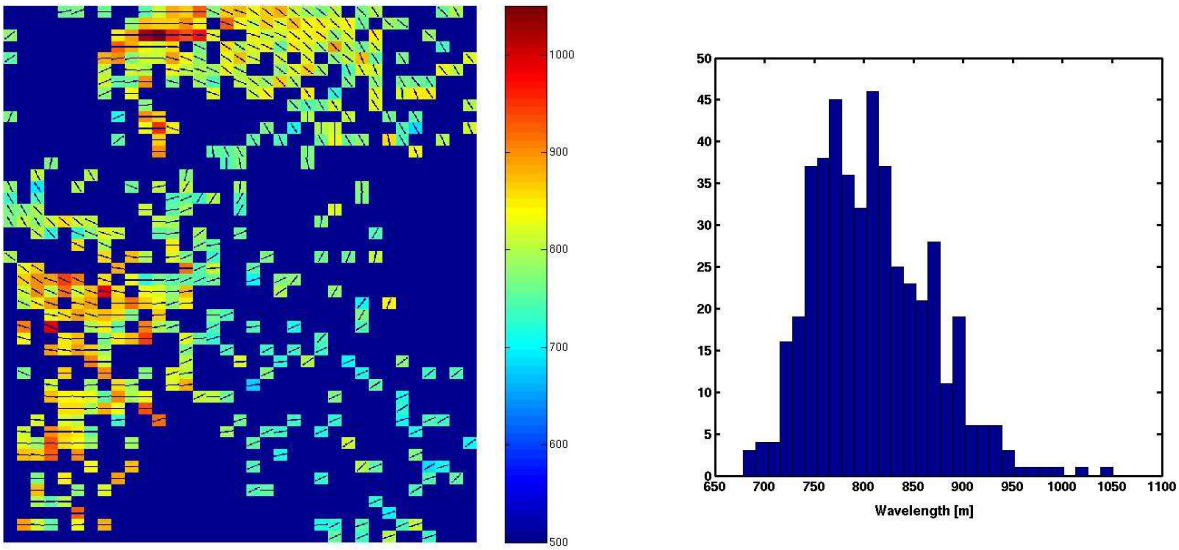

a) b)

Fig. 6-13: a) Wind rolls retrieved and b) histogram of wavelength for hurricane Danielle.

	Max. Wind Speed	Central Pressure	Cat	Number of Detected Rolls	Mean wavelength	STD
Hurricane Katrina	70 *m/s*	905 *mb*	V	265	879	74.38
Hurricane Rita	75 *m/s*	897 *mb*	V	247	875	81
Typhoon Kiko	40 *m/s*	955 *mb*	I	458	890	77
Typhoon Kiko	55 *m/s*	945 *mb*	II	198	877	77.6
Typhoon Songda	45 *m/s*	940 *mb*	II	709	844	68
Typhoon Marce	33 *m/s*	980 *mb*	II	189	911	92
Tropical storm Frances	23 *m/s*	982 *mb*	TS	606	897	80.7
Hurricane Wilma	49 *m/s*	958 *mb*	II	346	887	88
Typhoon Talim	63 *m/s*	925 *mb*	IV	244	863	75.8
Hurricane Danielle	46 *m/s*	977 *mb*	II	471	807	58.2
Hurricane Humberto	40 *m/s*	977 *mb*	I	440	822	55,9
Hurricane Lili	47 *m/s*	971 *mb*	II	711	823	53.4
Typhoon Sinluka	45 *m/s*	950 *mb*	II	605	788	48,6
Hurricane Floyd	51 *m/s*	943 *mb*	III	547	820	69,4
Mean value				431	855,92	77,71

Tab. 6-4: : Number of wind rolls and mean wavelength detected from each SAR image of Tab. 6-1.

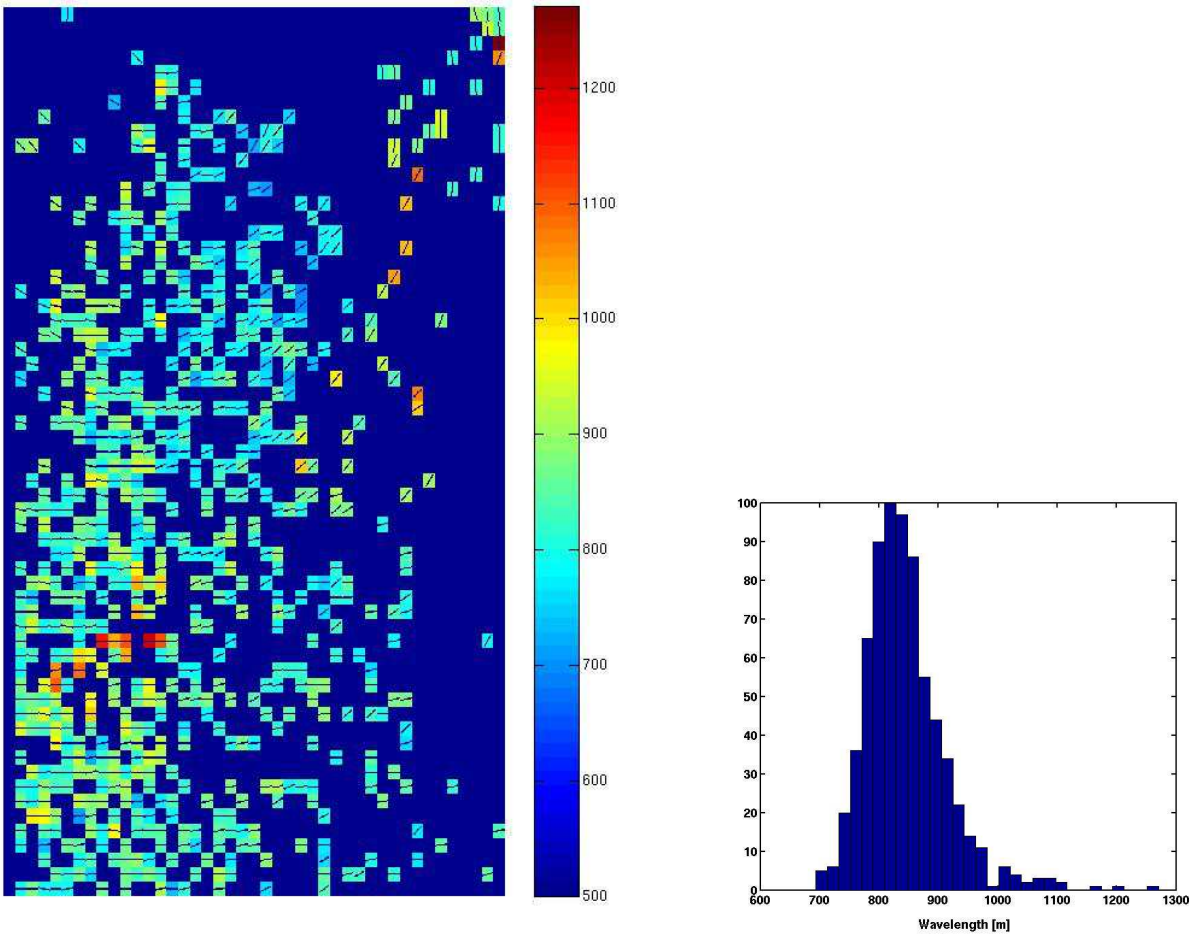

a) b)

Fig. 6-14: a) Wind rolls retrieved and b) histogram of wavelength for typhoon Songda.

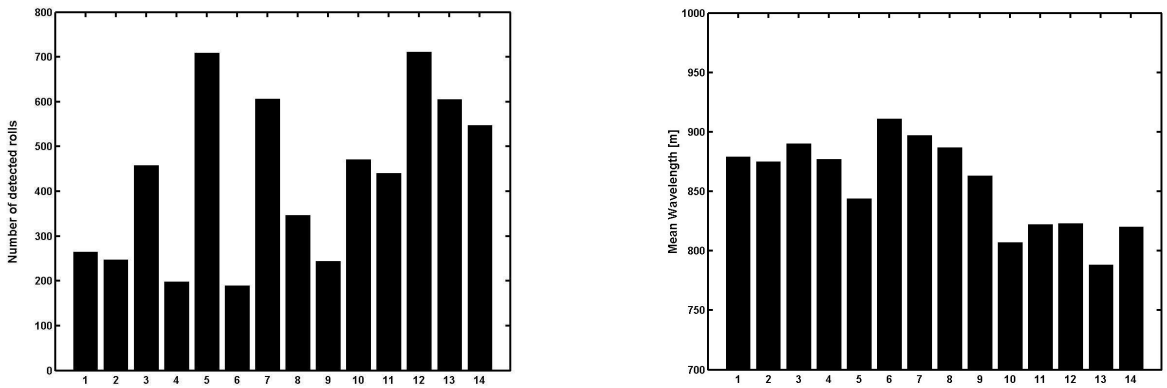

a) b)

Fig. 6-15: a) Number of rolls and b) mean wavelength of the dataset shown in Tab IV.

6.5 References

Foster R. C., 2009, Boundary Layer Similarity Under an Axisymmetric, Gradient Wind Vortex. *Boundary-Layer Meteorology*, vol 131, Issue 3, pp 321-344.

Foster R. C., 2005, "Why Rolls are Prevalent in the Hurricane Boundary Layer", *Journal of Atmospheric Sciences*, vol. 62, Issue 8, pp.2647-2661.

Jain, A.K., 1989. Fundamentals of Digital Image Processing, *Random House*, New York.

Kimball, S.K., and M.S. Mulekar, 2004, A 15-Year Climatology of North Atlantic Tropical Cyclones. Part I: Size Parameters. *J. of Climate*, no. 17, pp. 3555–3575.

Lehner S., Horstmann J., Koch, W., and Rosenthal W., 1998, Mesoscale wind measurements using recalibrated ERS SAR images. *Journal of Geophys. Res.—Oceans*, no.103, pp.7847−7856.

Morrison I., Businger S., Marks F., Dodge P., Businger J. A., 2005, An Observational Case for the Prevalence of Roll Vortices in the Hurricane Boundary Layer. *Journal of the Atmospheric. Sciences*, vol.62, pp.2662-2673.

Du Y., P. W. Vachon, 2003, Characterization of hurricane eyes in RADARSAT-1 images with wavelet analysis. *Canadian Journal of Remote Sensing*, no.29, pp. 491-498.

Reppucci, A., Lehner, S., Schulz-Stellenfleth, J., Yang, C. S, 2008, Extreme wind conditions observed by satellite synthetic aperture radar in the North West Pacific. *International Journal of Remote Sensing,* vol. 29, no. 21, pp. 6129-6144.

Stull R. B., 1998, An introduction to boundary layer meteorology. *Kluwer Accademic Publisher*.

7 A new technique to estimate tropical cyclone intensity using SAR Wide Swath data

The knowledge of the wind field in a tropical cyclone is essential for the estimation of its dimensions and the identification of the regions that may be seriously damaged by its passage.

The standard SAR wind field retrieval techniques allow retrieving a smooth field of wind vectors that can be used to define the size and the shape of the storm, but fail in the evaluation of the maximum wind speed, which is underestimated. Nevertheless Wide Swath SAR data contain valuable information on the tropical cyclone structure that can be used to infer its intensity.

In the first part of the chapter an analysis of the SAR measurements in tropical cyclone conditions is presented. For tropical cyclone conditions saturation of the radar backscatter and dampening due to heavy rain occurs leading to an underestimation of the wind speed. A quantitative damping of the cross section due to heavy rain is estimated using the radiative transfer model and compared to the SAR measurements. The influence of damping by rain on wind speed retrieval is then analysed.

In the second part of the chapter a new technique for the estimation of wind field in tropical cyclones from SAR data, using the parametric Holland model, is presented. The method is based on a least square minimization of the difference between a parametric model and the SAR measurement in the range where the wind speed is below 20 *m/s*. A strategy to include the technique into an operational hurricane forecast system is discussed. As a final step a possible correction for NRCS in tropical cyclones is presented.

7.1 Wind speed retrieval for tropical cyclone conditions

The extraction of quantitative information about the wind field of tropical cyclones from spaceborne SAR sensors is an important application. The potential of looking in a synoptic way with sub kilometric resolution at the ocean surface in condition where all the conventional instruments fail has gathered the interest of both the scientific community and the political authorities in charge of issue warnings. Several studies have been conducted on tropical cyclone wind field retrieval from SAR images [Shen et al, 2006], [Pichel et al., 2007], [Reppucci et al., 2008] and it has been shown that although the technique is able to retrieve a smooth field of wind vectors that can be used to define the size and the shape of the storm, the maximum wind speed is underestimated. As an example, Fig. 7-1 shows the wind speed retrieved using the scatterometer approach detailed in chapter 7 from the ASAR wide Swath image of hurricane Katrina acquired on Aug. 28, 2005. In the area where the wind speed should be higher than 30 *m/s* when compared to the actual winds peed (see Fig. 7-2) and in particular around the eye the directional distribution of wind speed contains artefacts, which do not seem to be of geophysical origin [Horstman et al., 2005].

In this case the maximum wind speed retrieved, of about 50 *m/s*, is much lower than the wind speed reported by the HRD of about 70 *m/s*. The cause of this underestimation can be mainly due to strong rain contamination and effects due to severe sea state. In the following an analysis of the NRCS measurements in tropical cyclone conditions will be presented. Particular emphasis will be put on the effect of rain on the NRCS measurements.

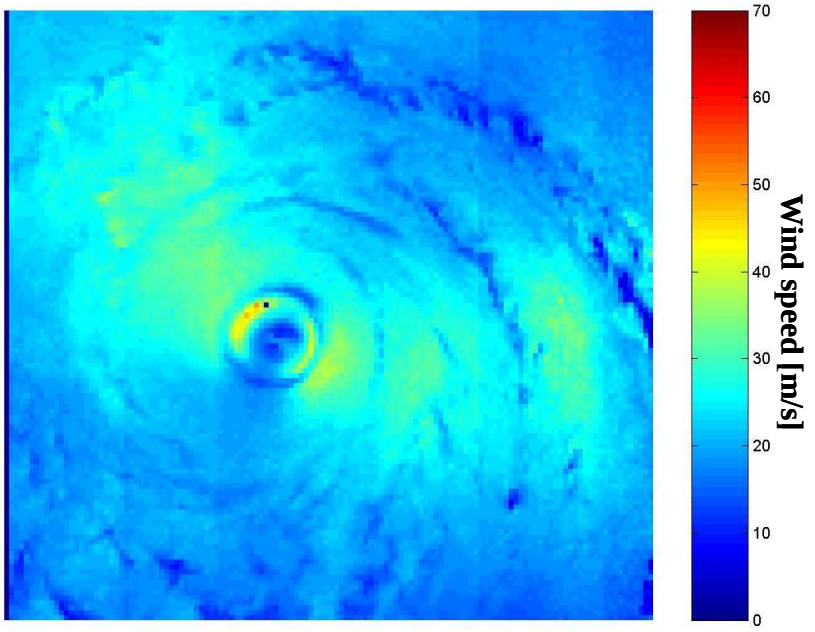

Fig. 7-1: SAR derived wind speed from the hurricane Katrina acquired over the Gulf of Mexico on Aug. 28, 2005 15:50 UTC.

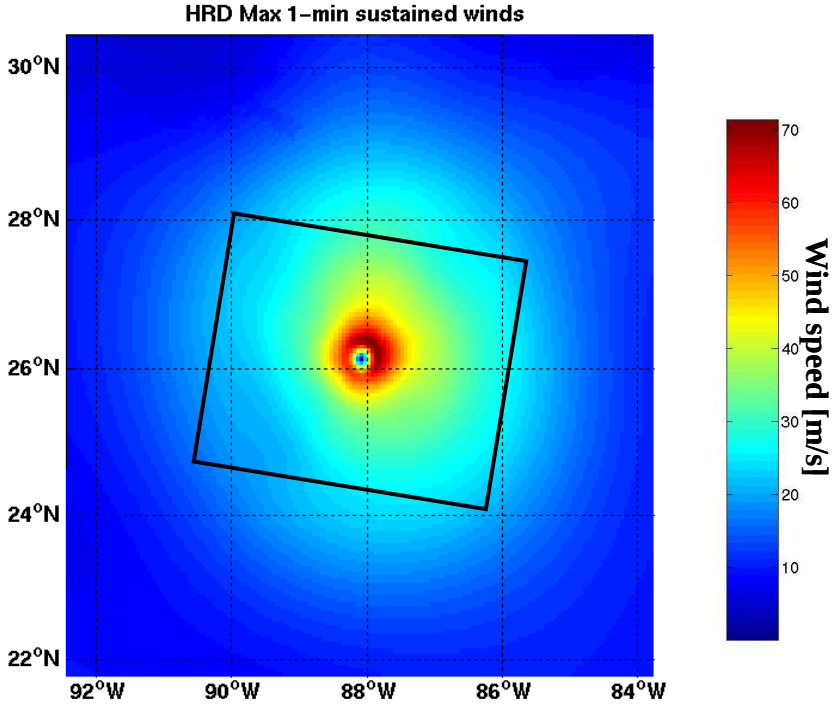

Fig. 7-2: Reanalysed wind speed U10 of hurricane Katrina at 15:00 UTC, processed by NOAA HRD. The black rectangle represents the SAR image of Fig.7.1

7.1.1 NRCS measurement in tropical cyclones

To quantify the amount of attenuation that occurs in NRCS measurements in tropical cyclone conditions the SAR measurements have been compared to simulated NRCS obtained using the Holland model wind field as input to the CMOD5 GMF. In these simulations the incidence angle

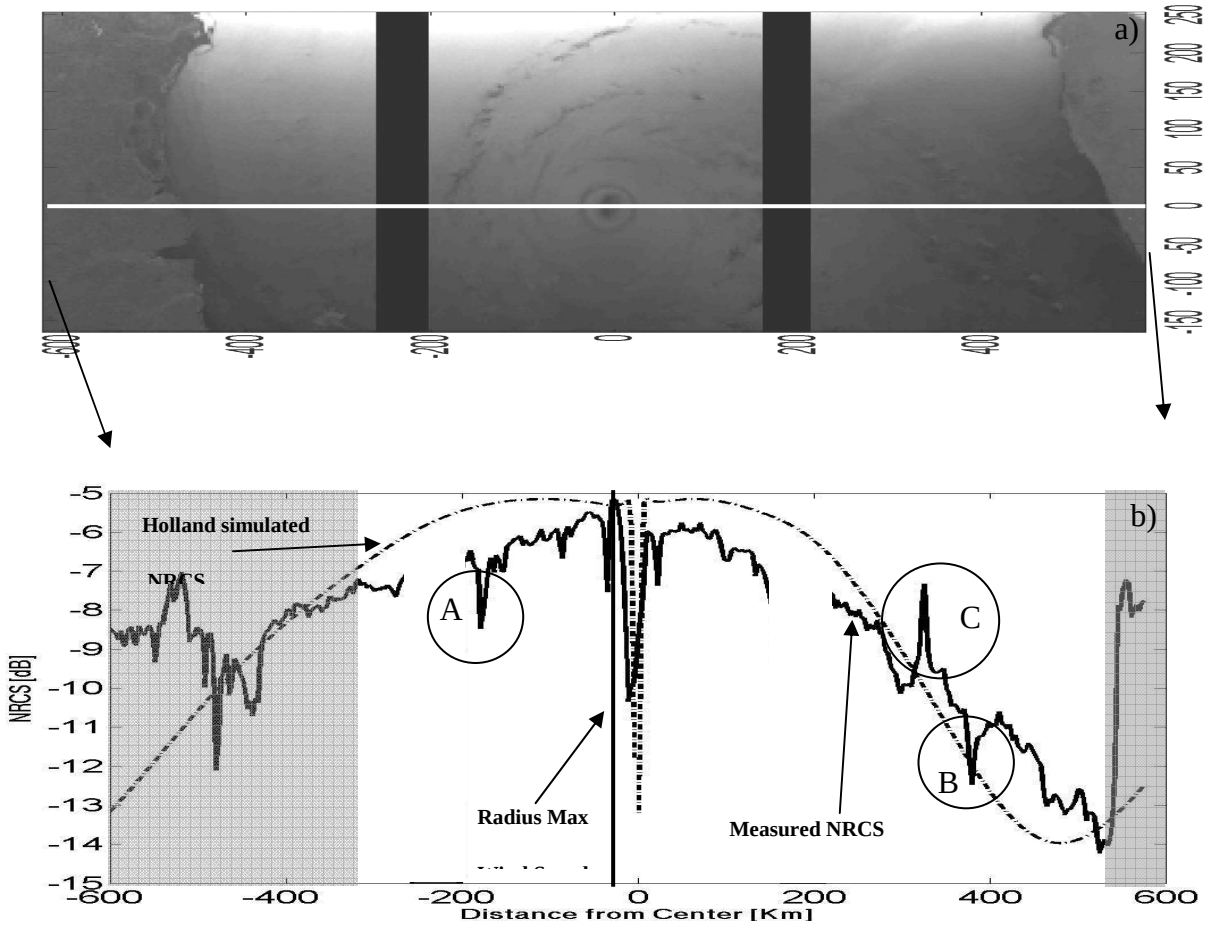

Fig. 7-3: (a) Along track cut (white line) through three consecutive images of Hurricane Katrina. (b) Measured (solid line) and simulated NRCS (dash dotted line) using the Holland model. Grey parts correspond to land.

grid is the same of the SAR image under investigation. The wind directions have been simulated using spiral direction turned 15° inside.

Fig. 7-3 b shows in solid the NRCS values corresponding to a cut through the centre of the hurricane's eye in the SAR image (see white line in Fig. 7-3 a) along the azimuth direction.

The dash dotted curve represents a simulation of the expected NRCS using wind speed from the Holland model. Within a distance of 300 *Km* from the centre of the hurricane we can observe that the measured NRCS is lower than the simulated one by about 1 dB.

From the cut it is possible to estimate the radius of maximum wind speed R_{MW} as approximately 25 *Km*. This is consistent with the in situ measurement reported by NOAA HRD [HRD web site].

A strong damping of 3 dB or more in the centre of the rain band “A” and about 2 dB for the rain band “B” can be observed. This damping arises from attenuation of the microwaves by raindrops in the atmosphere, from a modification of the sea surface roughness induced by the impact of raindrops and by wind field variations associated with the rain band. The area of enhanced backscattering “C” is due to a thunderstorm cell. As hurricane Katrina was characterized by a region of heavy rain around the centre, the uniform NRCS reduction can be in part explained by the atmospheric attenuation due to rain and by the change on the surface due to the impinging rain drops.

7.1.2 Analysis of rain damping

Depending on radar wavelength and incidence angle strong rain can have three different effects on microwave signals, i.e. scattering of the incident signal back to the sensor (Volume Scattering), attenuation of the microwave radar signals due to rain drop absorption, and alteration of the ocean surface roughness and hence of the backscattered signal.

Experiments in wave tanks have shown that the change of the surface roughness due to the impinging rain drops can be a significant source of error; unfortunately the limited number of experiments and the limited configuration of incidence angles and polarization at which they have been performed do not allow to fully parameterizing the modification of the NRCS by rain. Thus in this study a model which only takes in to account the atmospheric effects of the rain will be used.

Attenuation and volume scattering produced by rain drops has been widely studied and several formulations based on the Mie scattering are available [Ulaby, 1982].

The effects of the rain in the atmosphere have been modelled using the following formulation of the radiative transfer model:

$$\tilde{\sigma}_0 = \sigma_0 e^{-2kH\sec(\theta)} + \eta \frac{1}{2k}(1 - e^{-2kH\sec(\theta)}) \tag{7.1}$$

where θ is the radar incidence angle, $\tilde{\sigma}_0$ is the rain modified NRCS and σ_0 is the undisturbed NRCS. The model assumes a rain layer of height *H*.

The first term on the right hand size of Eq.7.1 represents the attenuation term, while the second is due to volume scattering.

The attenuation coefficient of rain, *k* (*dBKm*$^{-1}$), is related to the rain rate, *R*, by the following power law:

$$k = a \cdot R^b \tag{7.2}$$

The volume scattering coefficient, η (in m^{-1}), depends on reflectivity, *Z* (in mm^6m^{-3}), and rain rate, *R*, by:

$$\eta = \frac{\pi^5}{\lambda^4} 10^{-18} \left|K_0\right|^2 Z \tag{7.3}$$

$$Z = \alpha \cdot R^\beta \tag{7.4}$$

The model coefficients *a*, *b*, α, β, depend on the shape and drop size distribution (DSD) of rain drops.

The DSD exhibits a different behaviour according to whether the rain is convective or stratiform. Since both type of rain are present in tropical cyclones, the model coefficients are modelled using the results from [Haddad et al., 1997] for convective and stratiform rain. Tab. 7-1 lists the coefficients for the C-band case.

.	a	b	α	β
Convective clouds	0,0013	1,124	196,32	1,382
Stratiform clouds	0,0012	1,186	378,71	1,454

Tab. 7-1: Model coefficients for attenuation (eq.7.2) and reflectivity (eq.7.4).

In Fig. 7-4 (a) and Fig. 7-4 (b) the plots of the attenuated NRCS for different rain rate and for convective and stratiform rain are shown.

For low NRCS, that correspond to low wind speed the term that accounts for the volume scattering is dominant leading to an increase of the backscattering, while for high values of NRCS the attenuation is dominant. An additional attenuation term should be taken into account for the layer of foam that covers the sea surface in tropical cyclone conditions

7.1.3 Impact of NRCS attenuation on wind speed retrieval

The rain rate in tropical cyclones conditions can reach extreme values. Precipitations in hurricane Katrina measured on Aug. 28 2005, 03:25 UTC by TRMM satellite in Fig. 7-5 show around the eye and in the centre of the rain band values above 50 *mm/h.* Values of rain rate with the same magnitude were also measured by the NOAA HRD aircraft on the same day between 14:00 and 16:00 UTC as shown in Fig. 7-6.

To quantify the impact of rain on the measured NRCS the attenuation due to different rain rates has been simulated as a function of the undisturbed NRCS. The height of the rain layer *H* has been set equal to 5 *Km*, i.e. the mean freezing level altitude for the tropics. As shown in Fig. 7-4 (a) and (b) for a rain rate of 50 *mm/h*, the attenuation can be between -1.5 and -2 *dB*. These simulations indicate that about 60% to 80 % of the NRCS damping within tropical cyclones can be explained by rain attenuation in the atmosphere. The remaining damping can be explained considering that the rain can strongly modify the sea surface causing an additional damping of the measured NRCS that must be added to the one due to atmospheric attenuation. Finally there is a potential impact of the foam layer that covers the sea surface in tropical cyclones conditions on the SAR measured NRCS.

The effect of NRCS attenuation on the wind speed retrieval has been estimated through a simulation study. Using the CMOD5 GMF, NRCS values for wind speed between 3 and 70 *m/s* and for wind directions between 0° and 360° have been simulated. Then an attenuation of 0.5 *dB* has been applied. The attenuated NRCS has then been reused to retrieve back the wind speed.

Contour plots of the errors of the retrieved wind speed for two incidence angles are presented in Fig. 7-7a) and Fig. 7-7b).

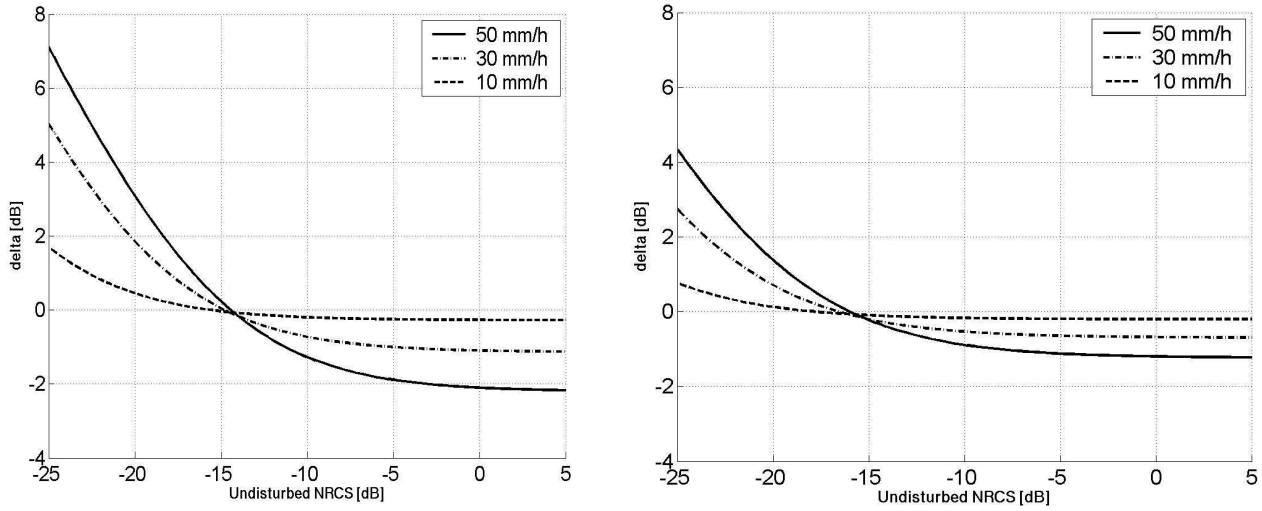

a) b)

Fig. 7-4: NRCS attenuation (delta) due to a) convective and b) stratiform rain vs. undisturbed surface NRCS for three different rain rates .

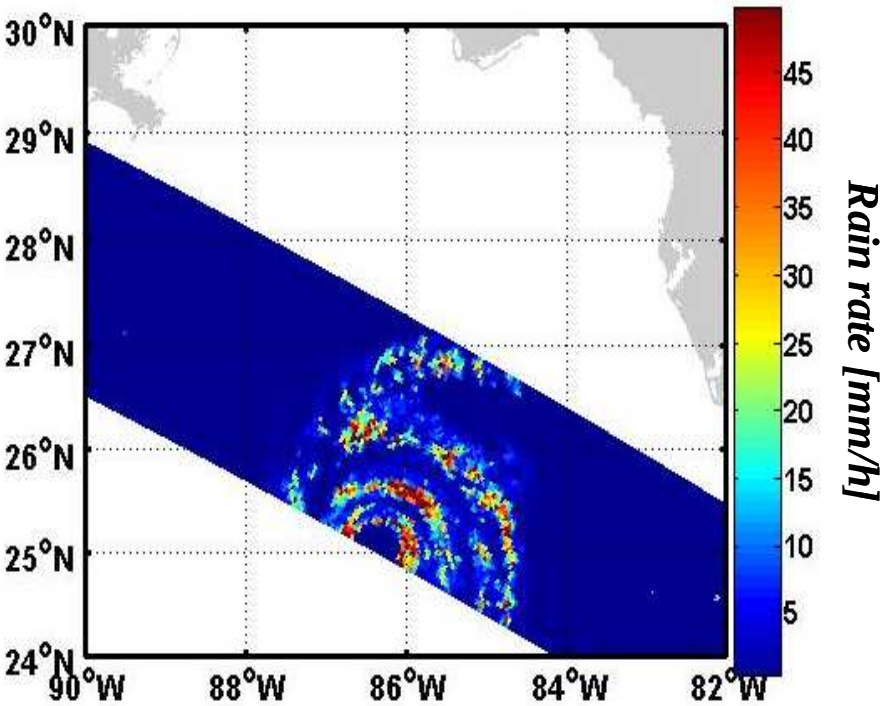

Fig. 7-5: Rain rate of hurricane Katrina measured on Aug. 28 2005, 03:25 UTC by TRMM satellite.

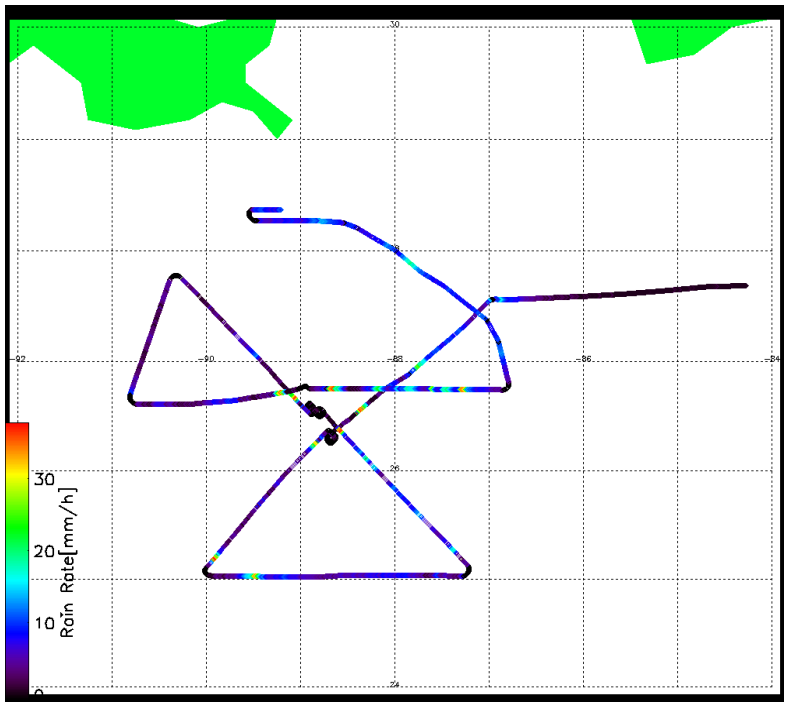

Fig. 7-6: Rain rate derived from the airborne Stepped Frequency Microwave Radiometer data on Aug. 28 for the hurricane Katrina.

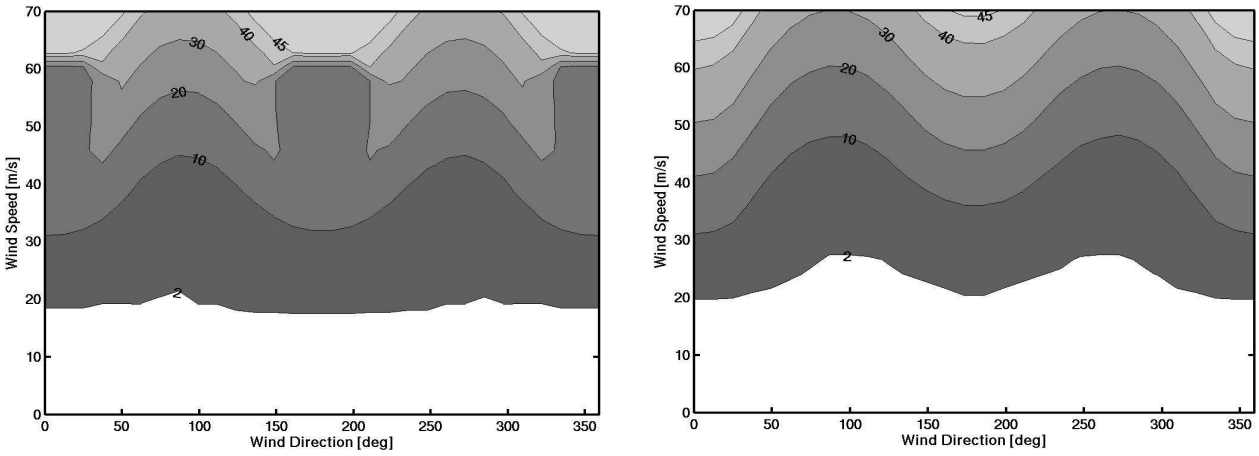

a) b)

Fig. 7-7: Contour map of the wind speed error [m/s] due to 0.5 dB attenuation in the measured NRCS as function of wind speed and direction for incidence angles of 25° (a) and 35° (b).

The error of the wind speed retrieval increase with wind speed. The rate at which the error increases depends also on the incidence angle and wind direction. This behaviour can be explained looking at the shape of the GMF (see Fig. 4-4). For low to medium wind speed, up to 20 *m/s*, the increase of NRCS with wind speed is high, so even a big error in the measurement will not affect significantly the wind retrieval. The contour plots of Fig. 7-7 (a) and Fig. 7-7 (b) show that for this case the error is less than 10%. For wind speed above 20 m/s the shape of the GMF is a flattened and small errors in the measured NRCS lead to large errors in the wind speed retrieved.

7.2 A new tropical cyclone wind speed algorithm

From the above analysis it is clear that due to severe sea state and high rain rates the retrieval of wind speed from SAR images can be affected in a severe way. To correct the measurements and in order to obtain reliable estimates of wind speed additional collocated information provided by other sensors are needed. Unfortunately these additional data are not available in most of the cases. Nevertheless, as tropical cyclones exhibit a stable behaviour, Wide Swath SAR measurements contain valuable information on the storm structure that can be used to infer its intensity, i.e. maximum wind speed. The contour plots of Fig. 7-7 a and Fig. 7-7 b clearly show that for wind speed of about 20 *m/s* or less the error on the SAR retrieved wind vector is less or equal to 10%, making the measurements rather reliable. Moreover the analysis in chapter 6 has demonstrated that, although the measurements are attenuated, it is possible to estimate the shape parameters of the tropical cyclone eye. The measurements of wind speed below 20 *m/s* and the estimated radius of maximum wind speed can be used to fit an appropriate Holland model, obtaining an estimate of the storm intensity.

In the following section details about this new technique will be given. Then the results for the selected hurricanes and typhoons cases will be analysed and discussed. The last part of the chapter will be dedicated to a potential correction to apply to SAR measurements in the area above 20 *m/s*.

7.2.1 Methodology

In this study to retrieve information on tropical cyclone intensity we make use of SAR Wide Swath images together with a priori information on tropical cyclones wind speed profiles from the Holland parametric model.

In a first step a one dimensional approach has been used to investigate the behaviour of the NRCS and of the wind speed in tropical cyclones conditions. From the SAR image a profile in the azimuth direction through the tropical cyclone has been extracted. This allows analysing the dynamics of the NRCS avoiding the strong modulation introduced by the incidence angle. The selected profile has then been used to retrieve the wind speed. In a further step a tropical cyclone wind speed profile has been superimposed using the Holland model. For these simulations the model input parameters central pressure and radius of maximum wind speed have been taken from the HRD [HRD web site] and JAXA [JAXA web site] web sites. Wind directions have been estimated from the SAR image using the technique detailed in section 4.4.

Fig. 7-8 to Fig. 7-12 show five profiles, extracted from different tropical cyclones, of the SAR retrieved wind speed (solid) and the Holland simulated wind speed (dash-dotted) along the flight direction. All the profiles show a good agreement with the Holland simulation in the area where the wind speed is below tropical storm force wind (17 *m/s*). This shows that SAR wind speed measurements below the aforementioned threshold are reliable even in tropical cyclone conditions.

Once the reliability of SAR measurements in the area of interest is established, a two dimensional approach has been used to estimate the tropical cyclone intensity.

As first step we have selected from the SAR retrieved wind field the area that is below to tropical storm force wind to avoid possible contamination by attenuation effects. As an example, Fig. 7-13 shows the wind field retrieved from the SAR image of hurricane Katrina and the area selected for the fitting procedure (red rectangles). The area has been selected using as thresholds 17 *m/s* and the tropical cyclone advection speed, i.e. the speed at which the storm moves as estimated by the

Meteorological Agency. In this area an appropriate Holland model which matches the SAR retrieved wind speed has been fitted.

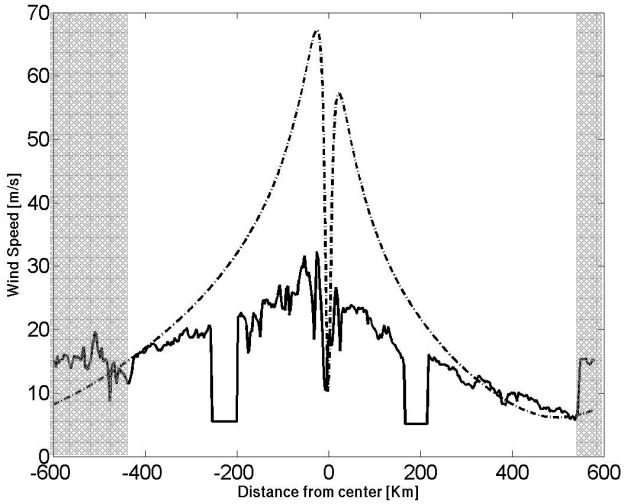

Fig. 7-8: Wind speed retrieved from a NRCS profile of Hurricane Katrina (solid) and the simulated wind speed using the Holland model (dash-dotted).

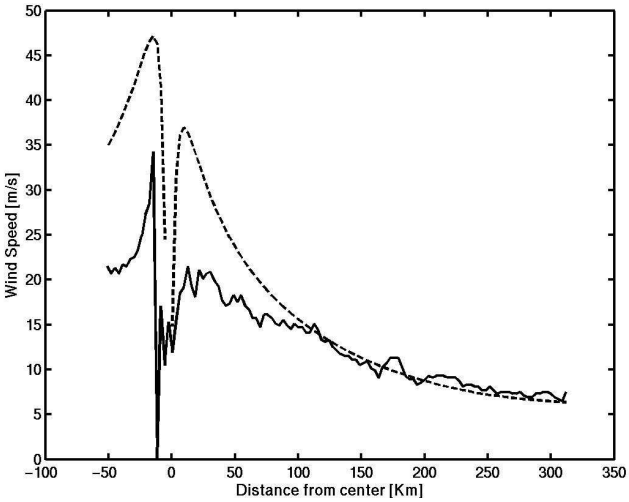

Fig. 7-9: Wind speed retrieved from a NRCS profile of Typhoon Kiko (Sept. 9) (solid) and the simulated wind speed using the Holland model (dash-dotted).

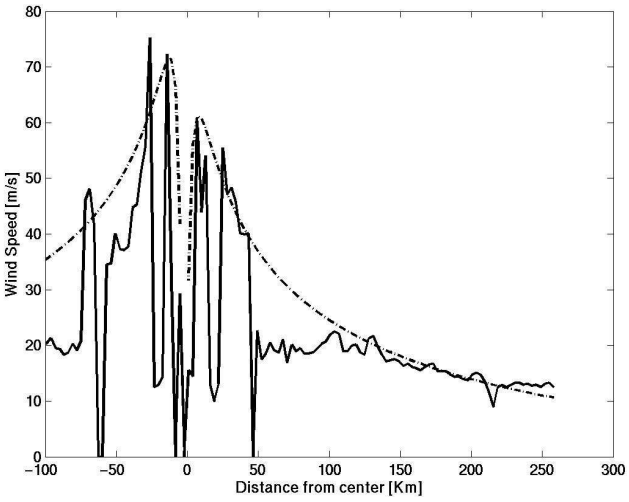

Fig. 7-10: Wind speed retrieved from a NRCS profile of Hurricane Rita (solid) and the simulated wind speed using the Holland model (dash-dotted).

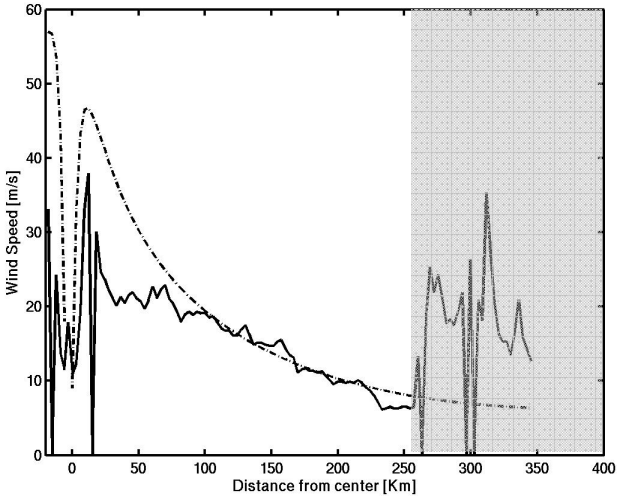

Fig. 7-11:Wind speed retrieved from a NRCS profile of Typhoon Kiko (Sept. 11) (solid) and the simulated wind speed using the Holland model (dash-dotted).

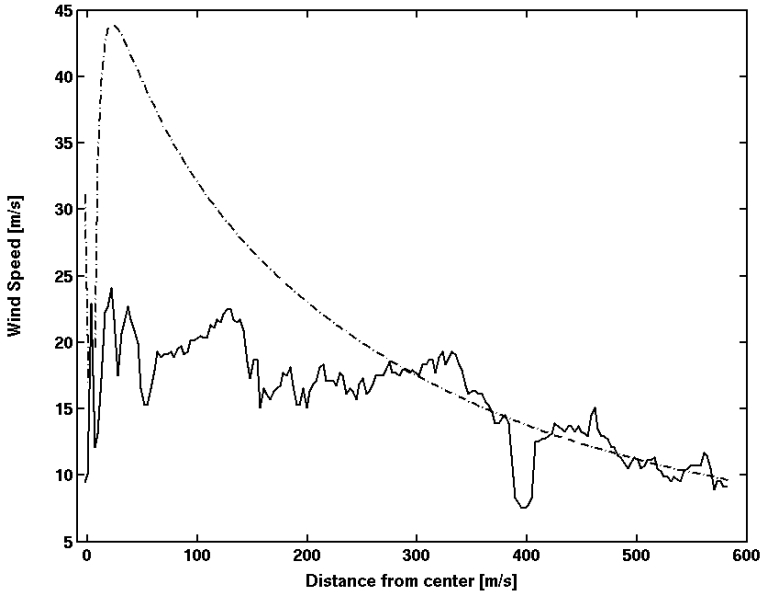

Fig. 7-12: SAR retrieved wind speed profile (solid) and fitted wind speed profile (dash dotted) for typhoon Songda on Sep 06 2005.

As explained in chapter 3 the Holland model depends on three inputs, i.e. the radius of maximum wind speed, the minimum central pressure and the maximum wind speed. In the fitting procedure the radius of maximum wind speed has been fixed as measured from the SAR images using the approach explained in chapter 6, while the central pressure and the maximum wind speed are free variables to be minimized.

The retrieved maximum wind speed and central pressure are the ones that minimize the cost function:

$$J\left(p_c, v_M\right) = \sum_{ij} \; abs\left[\hat{\sigma}_{ij}^{o}\left(p_c, v_M\right) - \sigma_{ij}^{o}\right] \tag{7.5}$$

where:

$\hat{\sigma}_{i,j}^{o} = \text{Holland simulated NRCS}$

$\sigma_{i,j}^{o} = \text{Holland measured NRCS}$

In Fig. 7-14 (a) is shown the three dimensional plot of the SAR retrieved wind speed and the result of the fitting in the case of the hurricane Katrina in Fig. 7-14 (b). The results of the fitting yield a new maximum wind speed of 67 *m/s* that agree with the HRD analysis of 70 *m/s*.

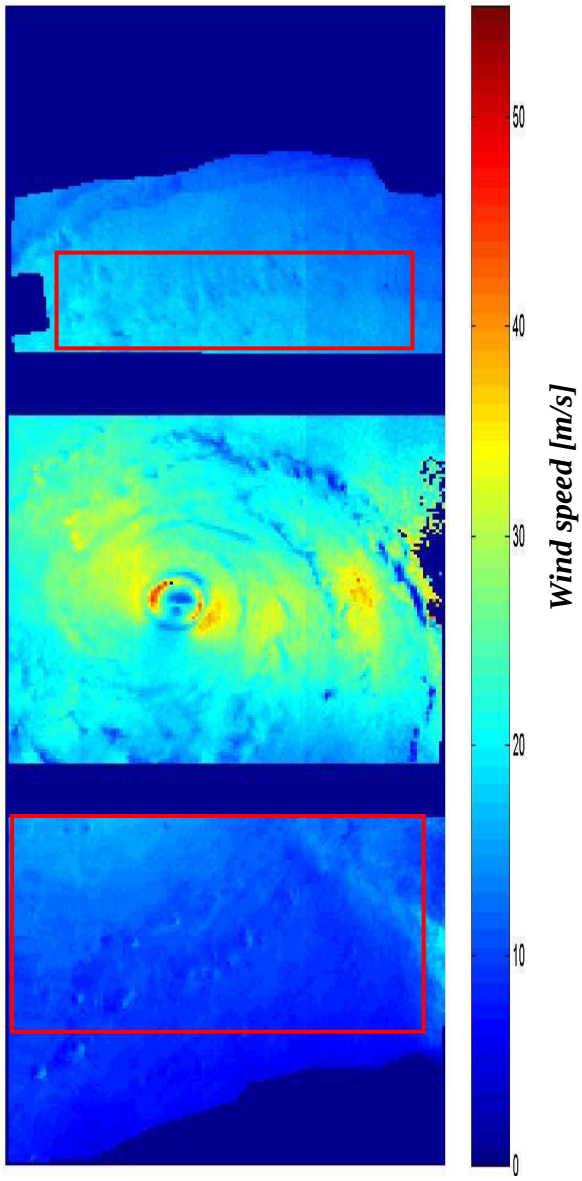

Fig. 7-13: Wind speed retrieved from the SAR image shown in Fig.7-3 a. The red rectangles define the area used for the fitting procedure.

7.2.2 Results

We validate the result of the new technique using five tropical cyclone images. All the images were acquired by the ASAR sensor in VV polarization. The choice of ASAR VV polarized images has been dictated by the possibility of using the GMF CMOD5 directly on the measurements, avoiding the use of a polarization correction that can be source of further error. For all the cases the fitting procedure succeeds to select a profile that matches the SAR retrieved wind speed in the area below 20 *m/s* giving an estimate of the tropical cyclone intensity. The values of maximum wind speed and central pressure estimated are in agreement with the values reported by the web site of HRD [HRD web site] and JAXA [JAXA web site], as reported in Tab. 7-2.

In the following the hurricane and typhoon cases will be analysed in detail. A statistic of the results will be shown as well. In a final step an analysis of the behaviour of the NRCS in the area above 20 *m/s* will be presented and a potential correction will be discussed.

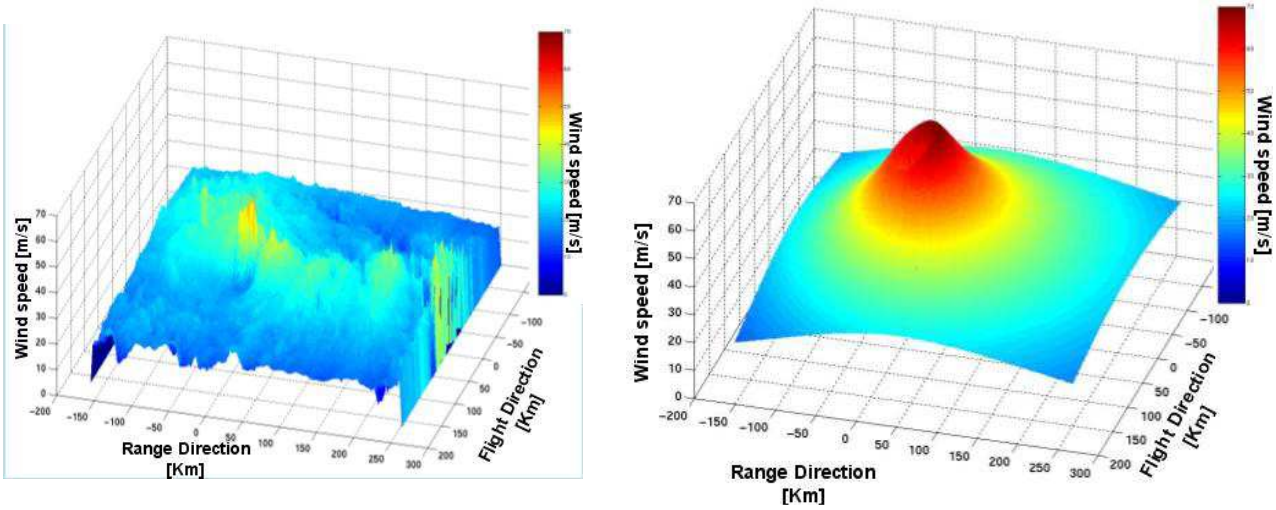

a) b)

Fig. 7-14: Three dimensional plot of the SAR retrieved wind speed a) and the result of the fitting in the case of the hurricane Katrina b).

	Measured Max Wind Speed	SAR Retrieved Max Wind Speed	Measured Central Pressure	SAR Retrieved Central Pressure
Hurricane Katrina	70 m/s	68 m/s	905 mb	901 mb
Hurricane Rita	75 m/s	70 m/s	897 mb	887 mb
Typhoon Kiko	45 m/s	48 m/s	955 mb	950 mb
Typhoon Kiko	55 m/s	60 m/s	945 mb	940 mb
Typhoon Songda	45	45	940	940

Tab. 7-2: Results of the new procedure for the determination of the max wind speed ad central pressure (eq. 7.5) applied to the data set of Tab. 7-1.

Hurricane cases

Two hurricane images of Katrina and Rita were acquired in the Gulf of Mexico in 2005 with the storm eyes clearly visible.

Hurricane Katrina was at the time of the ENVISAT satellite overpass a category V storm of large dimension with a radius of hurricane force wind of about 180 *Km* and the radius of tropical force wind exceeding 300 *Km*.

The cut in Fig. 7-8 shows that above 20 *m/s* there is a clear underestimation of wind speed that increases with distances approaching the hurricane eye. The wind speed difference reaches a maximum value of about 30 *m/s* in the area around the storm eye. The fitting procedure gives a value of maximum wind speed equal to 68 *m/s* that agrees with the values of 70 *m/s* reported by HRD.

Hurricane Rita reached the exceptional maximum wind speed of 80 *m/s* although the dimension of the storm where relatively small with a radius of hurricane force wind of only 50 *Km*.

From the cut in Fig. 7-10 one can observe that apparently around the eye the SAR measurements seem to agree well with the model measurements. For this case it must be considered, that the eye of the storm is in the near range of the SAR image at an incidence angle of 22°, where the measured NRCS can be contaminated by contribution due to specular reflection or breaking waves.

The fitting procedure gives in this case a maximum wind speed of 75 *m/s* and a central pressure of 890 *mb,* values that even in this case agree with the HRD report.

Typhoon cases

In the two SAR acquisitions of Kiko (Fig. 7-9 and Fig. 7-11) the maximum difference between the two profiles is smaller as the storm at the time of SAR acquisition was only category 1 according to the Saffir-Simpson scale with a maximum wind speed smaller by 30 *m/s* compared to Katrina case .

Also in the case of typhoon Songda (Fig. 7-12) the SAR retrieved wind speed profile shows a strong attenuation, that reach a maximum value of about 20 *m/s* in the area of maximum wind speed.

7.2.3 Statistics over ScanSAR scenes

A statistic of the retrieved maximum wind speed and central pressure is presented. The actual measured value for each tropical Cyclone in Tab. 7-3 has been taken from the HRD web site and the JAXA web site. In Fig. 7-15 is plotted the scatter plot of the measured maximum wind speed versus the retrieved maximum wind speed. The mean error is about 4 *m/s*. Fig. 7-16 shows the scatter plot of the retrieved central pressure versus the measured central pressure; the mean error is about 7 *mb*.

7.2.4 Error analysis

As final step, to estimate the effect of variations on the input parameters an error analysis has been performed.

For each of the input parameters radius of maximum wind speed, SAR measurements and advection speed of the storm 100 optimizations have been calculated adding at each run a random error ε to the parameter under investigation. The error ε has been chosen as follows: for the SAR measurement white noise with zero mean and standard deviation equal to 0.5 *dB* has been added; in the case of storm advection speed and radius of maximum wind speed an error with Gaussian distribution and standard deviation equal to 2.0 *m/s* and 2.0 *Km* respectively has been selected. Moreover to quantify the error due to a possible bias in the measured data a test of 100 optimizations has been done adding to the SAR profile each time a random value with zero mean and standard deviation equal to 0.5 dB.

In Tab. 7-3 the results are shown. The first column names the investigated input parameters, the second column presents the standard deviation of ε and in the last column the root mean square error of the estimated maximum wind speed. The procedure shows stable results and the effect of errors on the estimation of the input parameters lead to an RMS error that in the worst case is less than 7 % of the actual maximum wind speed.

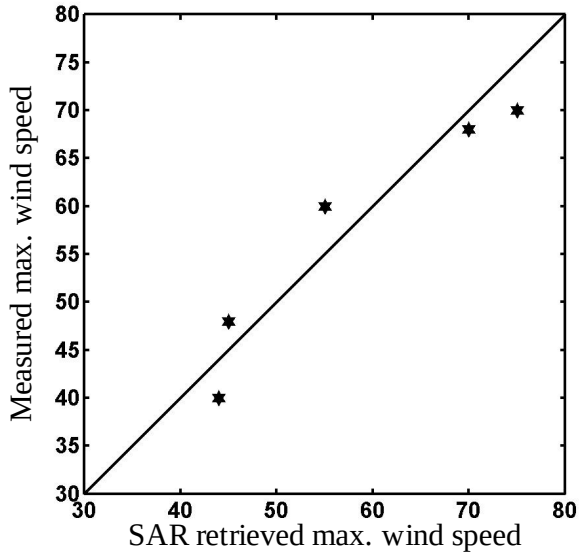

Fig. 7-15: Scatter plot of the measured max. wind speed versus the SAR retrieved max. wind speed.

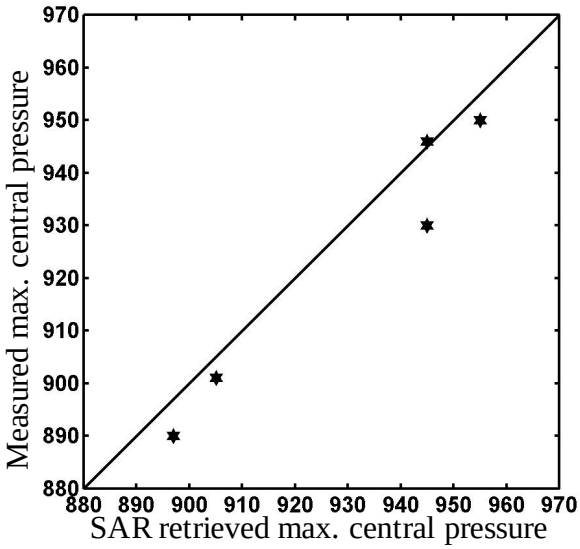

Fig. 7-16: Scatter plot of the measured minimum central pressure versus the SAR retrieved minimum central pressure.

	Std ε	**Max wind speed RMS error**
SAR measurement	0.5 *dB*	0.2 *m/s*
Advection speed	2.0 *m/s*	2.81 *m/s*
Radius max wind	2.0 *Km*	4.54 *m/s*
Bias	0.5 *dB*	3.28 *m/s*

Tab. 7-3: Error analysis of the optimization procedure.

7.3 NRCS correction

The analysis detailed in section 7.1.3 has shown that in the area above tropical storm force wind the retrieval of wind speed using the standard GMF (CMOD5) lead to underestimation that is dependent on wind speed, direction and SAR acquisition geometry, generally increasing for increasing wind speed. To analyse the SAR measurements in the area where the wind speed is above tropical storm force winds (33 *m/s*) a profile from the SAR image through the tropical cyclone eye has been extracted (Fig. 7-17 (a) and Fig. 7-18 (a)). This allows to study the trend of the measured NRCS for fixed incidence angle and fixed wind direction, though in the regime of the analysed wind speed (above 17 *m/s*) the modulation due to wind direction is few tenth of dB [Horstman et al. 2005].

Fig. 7-17 (b) and Fig. 7-18 (b) show two plots of SAR measured NRCS in the area above 17 *m/s* (red); the blue curve represent the simulated NRCS using Holland model and the GMF CMOD5 for the hurricane Katrina and the typhoon Kiko respectively. To compare the SAR measurements to the simulations a third order polynomial profile has been fitted to the SAR measurements (see dotted line in Fig. 7-17 b and Fig. 7-18 b). The difference between the two measurements is plotted in Fig. 7-17 c and Fig. 7-18 c.

In both cases we can observe that the difference between the measured NRCS and the simulated one decreases as we move in the direction of the storm eye. This can be explained observing the different trend between the SAR measurements and the simulations. The decrease of the NRCS predicted by the simulations seems not to be followed by the radar measurements.

However, in both cases the decrease shows a linear decrease with distinct slopes due to the different incidence angle at which the profile is extracted (33.9° for the Katrina case and 37° for Kiko case). This suggests that a correction to the SAR measurement could be in principle developed.

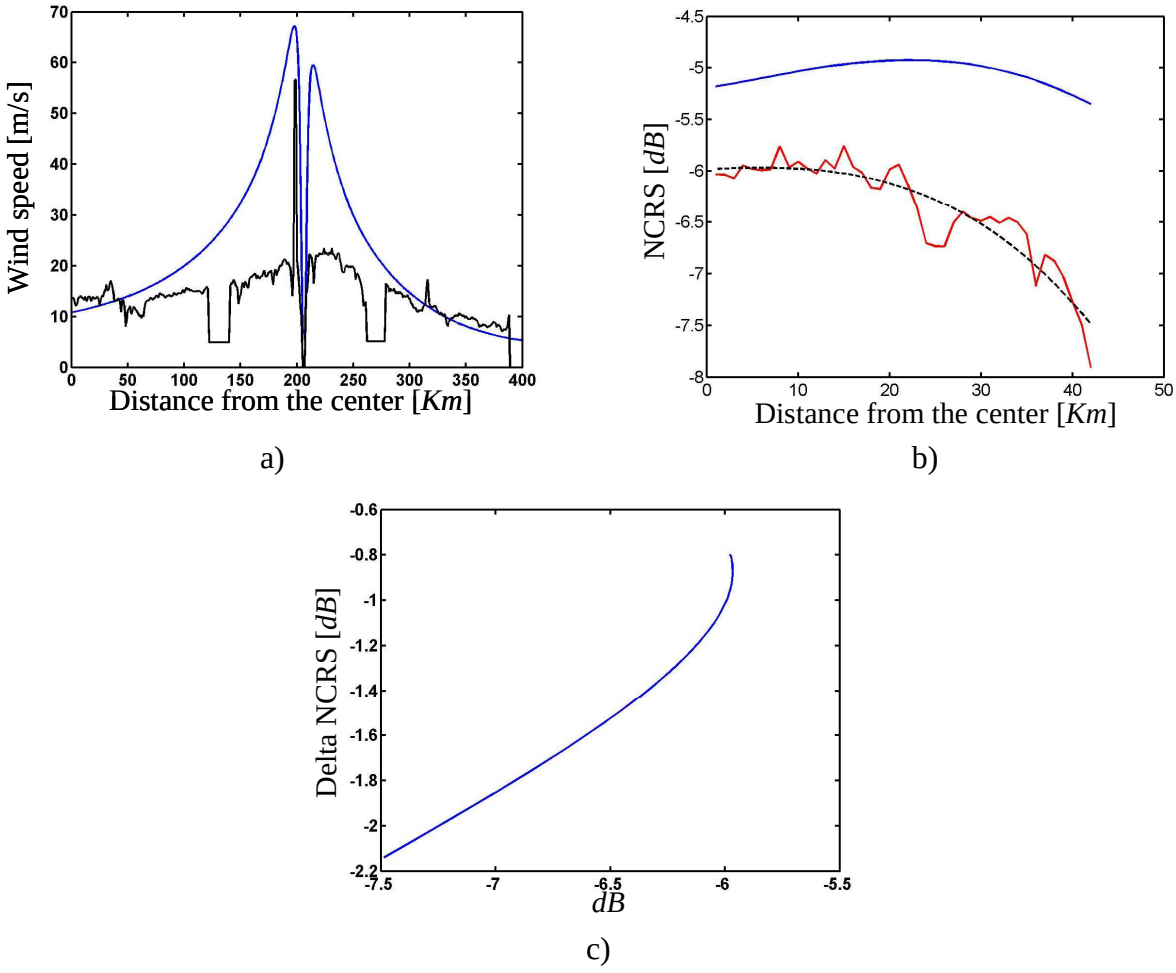

Fig. 7-17: SAR retrieved wind speed (black line (a)) and Holland simulated (blue line (a)) for hurricane Katrina. (b) shows the SAR measured NRCS in the area above 17 m/s (red line) and Holland simulated NRCS using CMOD5 GMF (blue line). The dashed line represents the 3rd order polynomial fitted to the SAR measurements, (c) shows the difference between the Holland simulated NRCS and the fitted profile of (b) (black dashed line).

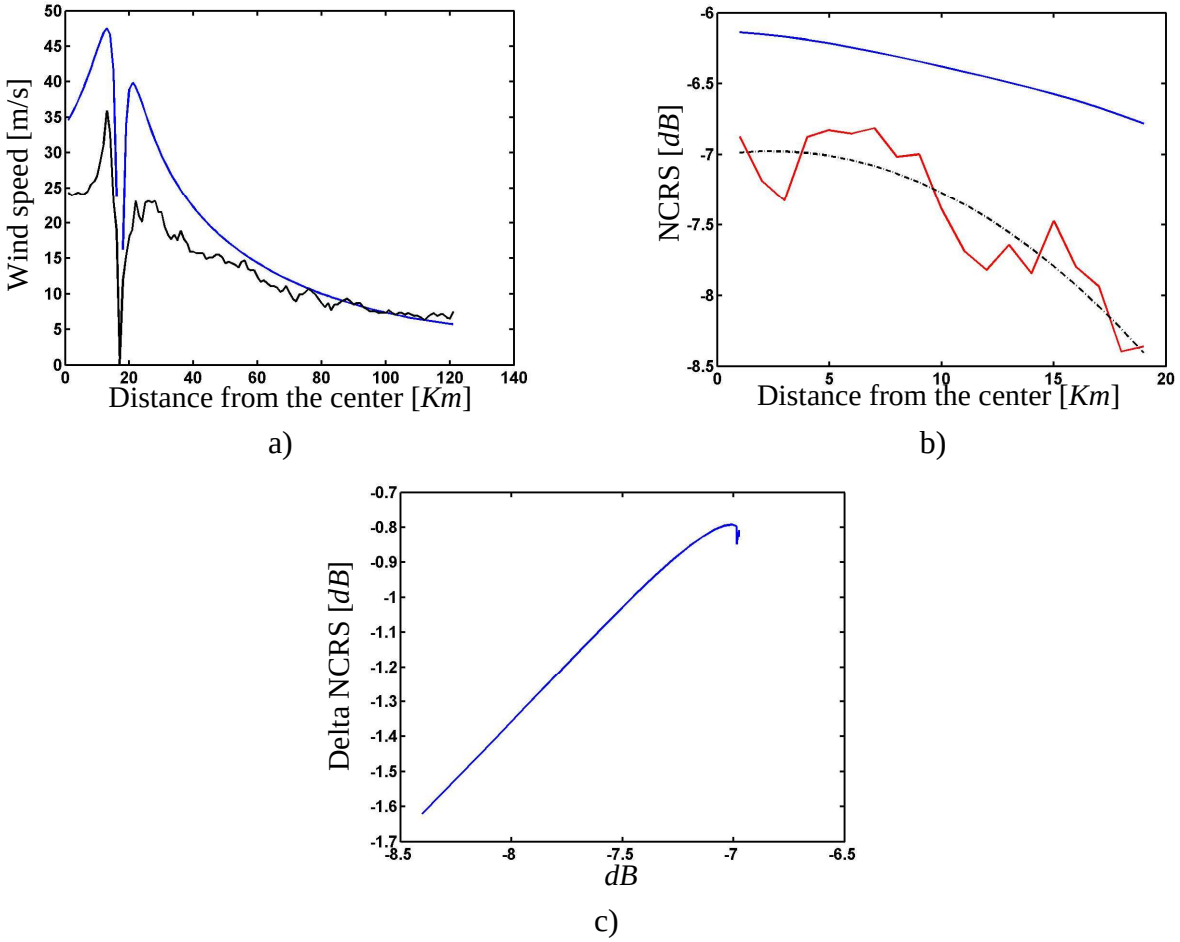

Fig. 7-18: SAR retrieved wind speed (black line (a)) and Holland simulated (blue line (a)) for typhoon Kiko; (b) shows the SAR measured NRCS in the area above 17 m/s (red line) and Holland simulated NRCS using CMOD5 GMF (blue line). The dashed line represents the 3rd order polynomial fitted to the SAR measurements; (c) shows the difference between the Holland simulated NRCS and the fitted profile of (b) (black dashed line).

7.4 Conclusion

Although C-Band is considered robust against atmospheric disturbances, the standard wind field retrieval technique using the scatterometer GMF CMOD5 shows an underestimation in the area of tropical cyclone force winds. This could be explained by the rain contamination and additional effects due to severe sea state that produce a strong damping of NRCS. This leads, for wind speed above 20 *m/s*, to an error in the retrieved wind speed that is up to 30 *m/s* when using the standard procedure, for the cases considered in this study. An Improvement could be given by the combined use of SAR with other instrument that can measure rain rate on the same platform.

A new technique to derive the maximum wind speed and the tropical cyclone strength from SAR images has been proposed. The problem of saturation in tropical cyclone wind regime is overcome basing the technique on the combined use of SAR measurements for areas of wind speed of 20 *m/s* or less and a parametric model for tropical cyclone wind speed. The radius of maximum wind speed, required as input, is measured from the SAR image using a technique base on wavelet transform. Wind directions have been computed from the SAR image using spectral analysis to detect the area containing feature associated with the wind flow and a new interpolation technique.

The procedure has been applied to five images of tropical cyclones showing agreement with in situ measurements. Maximum wind speed up to 70 *m/s* can be determined with an rms error of 3.9 *m/s*. More tropical cyclone images would be required for a further validation and optimization of the procedure.

7.5 References

Z.S.Haddad, D.A.Short, S. L.Durden, E.Im, S.Hensley, M.B. Grable, R.A. Black, 1997. A New Parametrization of the Rain Drop Size Distribution. *IEEE Trans. Geosci. Remote Sensing*, vol. 29, pp. 690–703.

J. Horstmann, D. R. Thompson, F. Monaldo, S. Iris, and H. C. Graber, 2005. Can synthetic aperture radars be used to estimate hurricane force winds? *Geophys. Res. Lett.*, 32, L22801.

HRD web site: http://www.aoml.noaa.gov/hrd/

JAXA web site: http://www.jma.go.jp/en/typh/

G. Pichel, X. Li, F. Monaldo, C. Wackerman, C. Jackson, C. Z.Zou, W. Zheng, K. S.Friedman, P. Clemente-Colón, 2007, ENVISAT ASAR Applications Demonstrations: Alaska SAR Demonstration and Gulf of Mexico Hurricane Studies. *Proc. 'Envisat Symposium 2007'*, Montreux, Switzerland 23–27 (ESA SP-636, July 2007).

A. Reppucci, S. Lehner, J. Schulz-Stellenfleth, C. S. Yang, 2008, Extreme wind conditions observed by satellite synthetic aperture radar in the North West Pacific. *International Journal of Remote Sensing 29*(21): 6129-6144.

H. Shen, W. Perrie and Y. HeThe, 2006, Capability of Hurricane Wind Monitoring by SAR. *Proceedings OceanSAR 2006 – Third Workshop on Coastal and Marine Applications of SAR*, St. John's, NL, Canada.

F. T. Ulaby, R. K. More, and A. K. Fung, 1981, Microwave Remote Sensing: Active and Passive. *MA: Addison-Wesley*, vol. 1.

A. Reppucci, S. Lehner, J. Schulz-Stellenfleth, S. Brush, 2010, Tropical Cyclone Intensity Estimated from Wide Swath SAR Images. *IEEE Trans. Geosci. Remote Sensing*, vol. 48, Issue: 4, pp. 1639 – 1649.

8 Analysis of Wave mode data taken under tropical cyclone conditions

Ocean waves, particularly in high wind and fetch limited conditions, can have an important role in the interaction between the ocean and the atmosphere, since they modulate the air/sea fluxes of momentum, heat and moisture. These parameters have been recognized as fundamental in the development of tropical and extratropical storms [Kataros et al., 1993].

The ERS satellites acquire SAR images of 10 by 5 *Km* size in Wave Mode every 200 *Km* along the orbit over all oceans providing about 1200 measurements daily. These images are of great interest for the study of tropical cyclone induced sea state and wind field, in particular in areas where measurements by airplane or in situ are not available or not feasible.

Several studies have demonstrated that SAR images of the ocean surface contain information on ocean waves [K. Hasselmann et al, 1995]. Different techniques can be used to retrieve the propagation direction of ocean waves, the surface wind speed and direction and to identify and analyse mesoscale surface features [Lehner et al., 2000].

This chapter focuses on the analysis of ocean wave parameters, e.g., significant wave height, and on the retrieval of surface wind speed in extreme wind and wave conditions using a new data set of reprocessed ERS-2 SAR Wave Mode data, also called “Imagettes”. These type of SAR images have been analysed and validated in the framework of Extrop project [Song G, 2009].

In details the data set contains scenes acquired over the North Atlantic in 1999 when several storms classified as hurricanes [http://www.nhc.noaa.gov] occurred. The number of overflights and the respective number of imagettes acquired in the vicinity of the tropical cyclones (within 500 *Km* from the storm centre) are summarized in Tab. 8-1. In Fig. 8-1 the sampling of hurricane Floyd which occurred in September 1999 is shown; the diamonds represent the imagettes acquired within 500 *Km* from the hurricane centre with the colour coding referring to the power loss corrected Normalized Radar Cross Section (NRCS). The colour of the hurricane path indicates the respective Saffir-Simpson storm intensity categories.

Hurricane track 1999		
Name	Num. of passes	Num. of Imagette
Bret	2	8
Cindy	8	45
Dennis	5	23
Floyd	10	40
Gert	11	48
Irene	5	19
Jose	6	31
Lenny	6	27

Tab. 8-1: Number of imagettes acquired within 500 Km of the centre of different hurricanes in the season 1999.

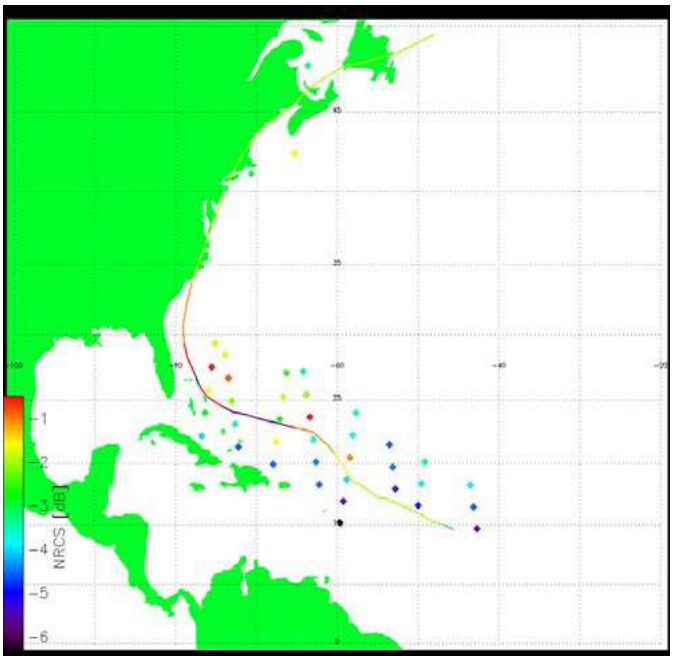

Fig. 8-1: Hurricane Floyd (Sep.1999) track with location of Wave Mode acquisitions.

Some illustrative case studies of extreme storms, e.g., Hurricanes Floyd and Gert in the North Atlantic in September 1999, are used for numerical experiments. The potential of wave mode data, which provide high spatial resolution and continuous sampling at the same time, to improve our understanding of storm dynamics is assessed. Comparisons of the SAR retrieved parameters with parametric Holland type cyclone models are performed.

8.1 Preprocessing of ERS-2 Wave Mode data

ERS2 SAR Wave Mode Data is not delivered as a image product by the ESA. The SAR Wave Mode data used in this study were processed to obtain single look complex images using the German Aerospace Centre processor BSAR [Breit et al. 1997] in the framework of the WAVEATLAS project. More technical details about the reprocessing of the data can be found in [Lehner et al., 1998]. In total more than 800000 Wave Mode images were processed, covering the period from January 1999 to December 2000.

After processing the Wave Mode data have been calibrated to NRCS values using the procedure developed by [Horstmann et al., 2003], as explained in chapter 4.

8.1.1 Inhomogeneity test

Several ocean features such as internal waves, wind streaks, surface slicks and eddies became visible in SAR images because they modulate the surface roughness induced by the wind and thus the backscattered radar power.

To exclude imagettes that contain features that could have a negative effect on the subsequent processing a homogeneity test is applied. The test used has been introduced in [Schulz-Stellenfleth and Lehner, 2004] and is based on statistical properties of periodograms, which are commonly used for spectral estimation. The homogeneity parameter ζ is close to 1 for homogeneous images.

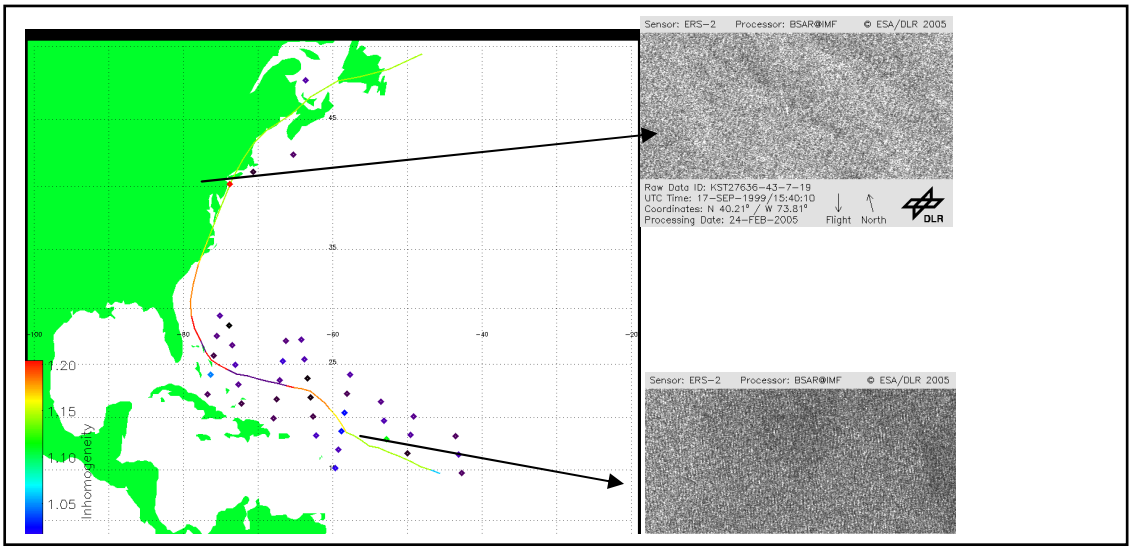

Fig. 8-2: Imagette Inhomogeneity along the hurricane Floyd path.

For inhomogeneous images it can significantly exceed 1. A threshold of 1.05 is used to separate homogeneous and inhomogeneous cases.

Most of the imagettes acquired near the hurricanes show homogeneous wave fields, which are suitable for subsequent wave parameter extraction. Only few images are inhomogeneous. Such images are located near the centre of the hurricane showing structures of the eye wall or rain cells, as shown in Fig. 8-2 where the diamond representing the Wave Mode data are coloured according the inhomogeneity value ζ. In total only 5% of the imagettes acquired near the hurricane were found to be inhomogeneous.

8.2 Ocean waves and wind speed analysis

In this section, two different case studies are considered. The first study concerns the hurricane Gert; an analysis of the ocean wave spectrum and NRCS of the Wave Mode data is summarized.

The second case study considers the hurricane Floyd. A technique that is able to retrieve information on significant wave height and wind speed from Wave Mode data using the empirical CWAVE-1 algorithm [Schulz-Stellenfleth, 2007] is shown.

8.2.1 Hurricane Gert

It has been demonstrated that SAR data can be used to estimate the 2D ocean wave spectra [Hasselmann and Hasselmann, 1991], [Schulz-Stellenfleth et al., 2005], [Schulz-Stellenfleth and Lehner, 2004].

	CMOD5	**Scatterometer**	**Holland**
Imagette lower	57.0 m/s	20.3 m/s	57.6 m/s
Imagette upper	14.5 m/s	16.3 m/s	37.5 m/s

Tab. 8-2: Imagette retrieved wind speed compared with scatterometer and simulated wind speed.

Using a technique based on cross-spectrum analysis [Engen and Johnson, 1995] it is possible to retrieve the direction of the wave systems imaged by SAR images. As an example 2D spectra retrieved from two SAR Wave Mode images acquired in proximity of the eye of hurricane Gert on Sep 19, 1999 are shown in Fig. 8-3 (right-hand side).

In particular the spectrum retrieved from the upper image, in Fig. 8-3, shows two wave systems. The first one is a wind sea, with a wavelength of about 125 *m*, which is due to the local wind field and aligned with wind direction. The second longer swell system has a wavelength of about 500 *m*. Analysis of the imaginary part of the cross spectrum revealed that these waves are traveling in southerly direction, thus in a direction opposite with respect to the hurricane heading.

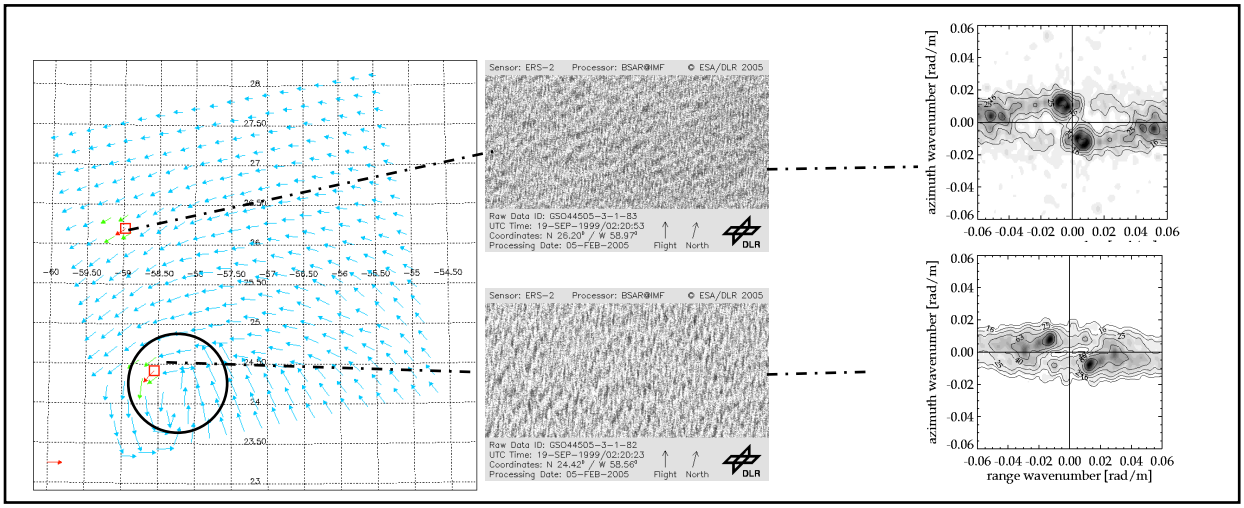

Fig. 8-3: Scatterometer wind field (left) with collocated imagettes (centre) and ocean 2D wave spectrum (right) acquired over the hurricane Gert on Sep 19, 1999.

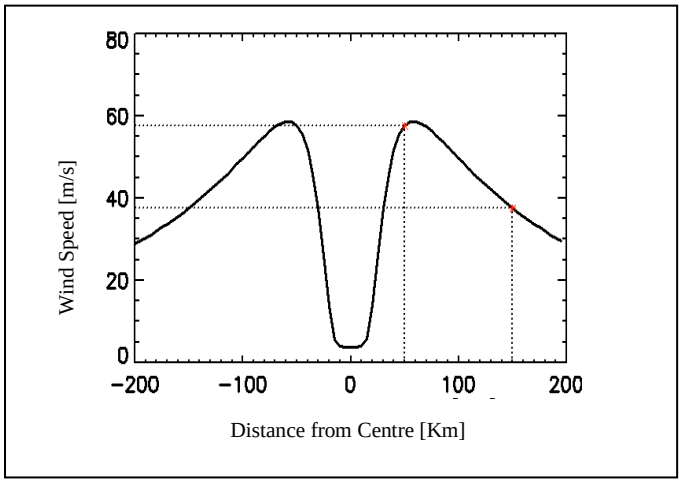

Fig. 8-4: Wind speed profile of hurricane Gert using Holland Model, the asterisk represent the position of imagettes in Fig. 8-23.

A possible explanation is that the swell system was generated by the hurricane Floyd which in that period was located about 1000 kilometres to the north of hurricane Gert.

After radiometric calibration and power loss correction, which is particularly significant in case of high wind speed, the two imagettes of Fig. 8-3 have been used to estimate the wind speed using the geophysical model function CMOD5, and compared with the scatterometer wind speed and the wind speed simulated using the analytical Holland model [Holland, 1981] (see Tab. 8-2).

Fig. 8-4 shows a wind speed profile generated using the Holland model with the position and the relative value of speed in correspondence of the two imagettes. The value of speed retrieved from the lower image is in agreement with the simulated speed and higher than the scatterometer speed, while for the upper image the retrieved value and the scatterometer value are comparable and both lower than the simulated wind speed.

In a following step a comparison with a parametric model presented in [Ross, 1976] is carried out in order to check whether the spectral parameters are consistent with other wave observations made in hurricane conditions. In this model the peak wave period T_p is expressed as a function of the dimensional radial distance

$$\overline{X}_r = X_r g / U^2 \tag{8.1}$$

and wind speed U as

$$T_p = \frac{1}{0.97} \overline{X}_r^{0.21} \tag{8.2}$$

where X_r is the distance to the hurricane centre. Using the above values for wind speed derived from CMOD5 and radial distance we get T_p=10.0 *s* for the Wave Mode image at the boundary and T_p=17.2 *s* for the Wave Mode image closer to the hurricane centre. This is in reasonable agreement with the observed wavelength of 418 *m* and 125 *m*, which correspond to 16.4 *s* and 9.0 *s*, respectively, assuming deep water.

8.2.2 Hurricane Floyd

The CWAVE-1 algorithm [Schulz-Stellenfleth 2007] used for wave parameter extraction is based on an empirical SAR imaging model and requires as unique input the calibrated Wave Mode data. Using a training data set of imagettes collocated with ocean wave spectra and wind speed computed with the numerical model WAM, run at the European Centre for Medium-Range Weather Forecast (ECMWF), a linear model is fitted. It takes as input variable the NRCS, the image variance and a number of additional spectral parameters.

In this study the CWAVE-1 method has been used to retrieve the significant wave height H_s from Wave Mode data acquired under tropical cyclone conditions. Due to the difficulties encountered to obtain in situ measurements of sea state parameter, numerical simulations carried out at the University of Miami [Tenerelli and Chen, 2001], [http://www.orca.rsmas.miami.edu/floyd] for validation purposes have been used. Fig. 8-5 shows an example of H_s estimation for the hurricane Floyd on 12 Sep. 1999. The H_s retrieved from the imagettes, represented by triangles and coded according to the vertical colour-bar (located in the figure right-hand side), is superimposed on the simulated H_s field, with colours referring to the horizontal colour-bar. The agreement between the retrieved and the simulated H_s is reasonable.

In a second step the CWAVE-1 algorithm has been used to retrieve the wind speed in 10 *m* height from imagettes. On average the agreement with ECMWF wind data is reasonable with an RMS error of 1.76 *m/s* that is below the standard used to measure the scatterometer performances.

Fig. 8-7 shows a scatterometer wind field, as color-coded background, and the wind speed retrieved from the imagettes as colour-coded triangles. Even in this particular case the agreement is reasonable and it has to be pointed out that in the wind speed retrieval using the CWAVE-1 algorithm no external information on wind direction was used.

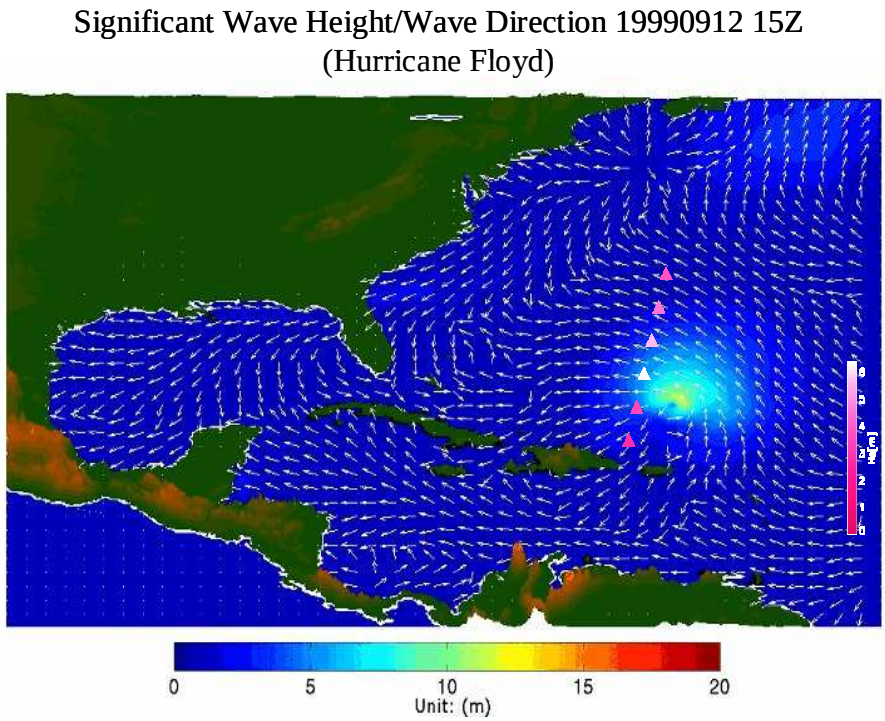

Fig. 8-5: Mean wave heights retrieved from imagettes (triangles with pink colorbar associated) compared with numerical simulation for hurricane Floyd (background with rainbow colorbar associated).

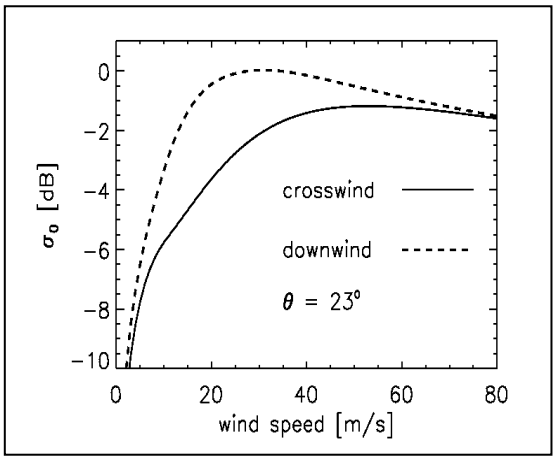

Fig. 8-6: Simulated CMOD5 NRCS as function of wind speed for downwind and crosswind case at fixed incidence angle of 23°.

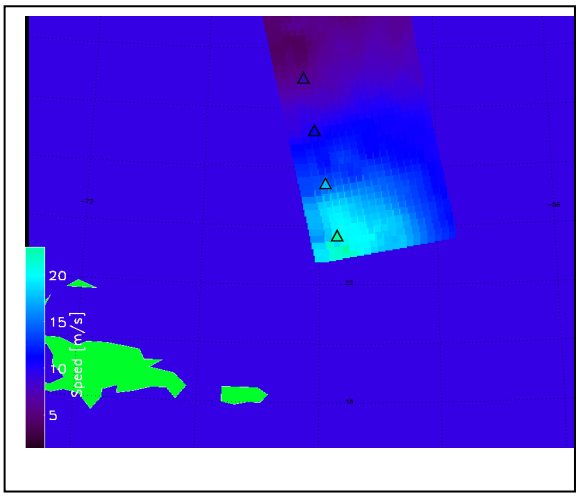

Fig. 8-7: SCAT wind speed and CWAVE-1 derived wind speed superimposed (triangles).

8.3 References

Breit H., Schattler B., and Steinbrecher U. , 1997, A high precision workstation-based chirp scaling SAR processor. In *Proceedings of the International Geosc. and Rem. Sens. Sym*. 1997, Singapore.

Engen G. and Johnson H., 2004, SAR-ocean wave inversion using image cross spectra. *IEEE Trans. Geosci. Remote Sensing*, vol. 33, pp. 1047–1056, 1995.

Kataros K.B. et al, 1993, Surface Fluxes and their Relation to Plabetary Boundary Layer Structure. *In Proc. The Air-Sea Interface Radio and Acustic Sensing, Turbulence and Wave Dynamics*, Marseilles, France.

Hasselmann K. and Hasselmann S.,1991, On the nonlinear Mapping of an Ocean Wave Spectrum Into Synthetic Aperture Radar Image Spectrum. *Journal of Geophys. Res*., vol. 96, pp 10713-10729.

Hasselmann K. et al., 1985, Theory of Synthetic Aperture Radar Ocean Imaging: A MARSEN View. *Journal of Geophys. Res.*, vol. 90, pp 4659-4686.

Hengen G. and Johnson H.,1995, SAR Ocean Wave Inversion Using Image Crosss Spectra. *IEEE Trans. Geosci. Remote Sensing*, vol. 33, pp. 1047-1056.

Holland G.J., 1980, An Analitical Model of the Wind and Pressure Profiles in Hurricanes. *Monthly weather review*, vol.108, pp.1212-1218.

Horstmann J., Schiller H., Schultz-Stellenfleth J. and Lehner S., 2003, "Global Wind Speed Retrieval From SAR", *IEEE Trans. Geosci. Remote Sensing*, vol. 41, no. 10.

Kerabaol V. and Chapron B., 1998, Analysis of ERS-1/2 Synthatic Aperture Radar Wave Mode Imagettes. *J. Geophys. Res.*, vol. 103, pp 7833-7846.

Lehner S. et al., 2000, Wind and Wave Measurement Using Complex ERS-2 Wave Mode Data. *IEEE Trans. Geosci. Remote Sensing*, vol. 38, no. 5.

Lehner S., Schattler B., Schulz-Stellenfleth J., and Breit H., 1998, Processing and calibration of ERS SAR single look complex imagettes – Extraction of wind and sea state parameters. *In Proceedings of the CEOS SAR Calibration and Validation Workshop* '98, Noordwijk, The Netherlands.

Off line Wind Scatterometer ERS Product User Manual (V2.1), 1999, CERSAT-IFREMER.

Ross D.B., 1976, Observing and Predicting hurricane wind and wave conditions, Atlantic Oceanographic Meteoro. Lab NOAAA, *Collected Reprints*, pp. 549-567.

Song G., 2009, Statistical analysis of global ocean wave and wind parameters retrieved with empirical SAR algorithms. Hamburg, Univ., Diss.

Schulz-Stellenfleth, J., S. Lehner, and D. Hoja, 2005, A parametric scheme for the retrieval of two-dimensional ocean wave spectra from synthetic aperture radar look cross spectra, *Journal of Geophys. Res.*, 110, C05004.

Schulz-Stellenfleth J. and Lehner S. Measurement of 2-D Sea Surface Elevation Fields using Complex Synthetic Aperture Radar Data, *IEEE Trans. Geosci. Remote Sensing*, Vol. 42, No 6, pp 1149-1160.

Schulz-Stellenfleth J. and Lehner S., 2004, Measurement of 2D Sea Surface Elevation Fields Using Complex Synthetic Aperture Radar Data. *IEEE Trans. Geosci. Remote Sensing*, vol. 42, no. 6, Jun.

Schulz-Stellenfleth J., König T. and Lehner S., 2007, An empirical approach for the retrieval of integral ocean wave parameters from synthetic aperture radar data, *Journal of Geophysical Research*, 112.

Tenerelli J., Chen S.S., 2001, High-resolution Simulation of hurricane Floyd using MM5 Coupled with a wave model. *In Tenth PSU/NCAR Mesoscale Model User's Workshoop*.

http://www.orca.rsmas.miami.edu/floyd

9 General Conclusions

This PhD focused on the use of Synthetic Aperture Radar (SAR) data for the retrieval of tropical cyclone characteristics. It was part of the EXTROP project (Investigation of Tropical and Extratropical Cyclones using Satellite data), which concentrated also on the study of the evolution of tropical cyclones and on their transition to extratropical storms that can affect Europe. Six PhD candidates have been funded by the EXTROP project; two focusing on numerical modelling of cyclones, two investigating the cyclones' characterization using passive remote sensing. The two last PhD topics considered the use of active remote sensing (radar, altimeters) for wind field retrieval; the present work was dedicated to the development of techniques for tropical cyclone analysis using SAR (Synthetic Aperture Radar) data.

The first part of this report consisted in an overview of the state of the art in the field of tropical cyclone characterization. An extensive bibliographic study has been performed in order to reassess the basic principles of the SAR imaging of sea surfaces and to highlight the advantages and drawbacks of the methodologies and techniques applied for tropical cyclone analysis.

In the second chapter, the basic SAR imaging mechanism and the main processing steps have been reviewed. The theory of the imaging of ocean surfaces and wave imaging mechanisms was particularly considered. Based on the analysis of the surface roughness, the SAR signal can indeed be used to characterize the sea state in terms of waves and wind field.

Tropical cyclone characterization and numerical modelling techniques were investigated in the third chapter. The prediction of intensity and track of tropical cyclones, which are characterized by intense and fast varying winds are an issue for the forecasting and scientific community. The parametric model of Holland extensively used in the study has been presented. This model has been selected and used as reference due to its analytical nature. It was optimized and used together with SAR wind field measurements to improve the wind field retrieval in areas where the SAR saturates.

The different techniques used for the retrieval of wind field from SAR image were reviewed in the chapter four. Classical methods based on the inversion of a geophysical model function were first described. The image calibration was discussed in detail for the different types of SAR images, as it constitutes the basis for a correct retrieval of the SAR wind speed. Different algorithms used for the wind field retrieval under tropical cyclone conditions, were then enumerated and investigated. Advantages and drawbacks of each method were highlighted and analysed in order to stress the need for improving the existing models, especially in case of tropical cyclones where the saturation of the backscattered signal is the principal reason for the often strong underestimation of the actual wind speed.

The second part of the report was then dedicated to the presentation of the algorithms developed in the framework of the PhD for the retrieval of tropical cyclone intensity, based on the use of SAR image intensity and of a numerical model.

In chapter five the SAR datasets used for the study were described. Those data sets come from different sources. A detailed introduction to ENVISAT ASAR Wide Swath mode (ScanSAR) data, RADARSAT Wide Swath mode data and ERS-2 wave mode data was presented. Then a description of ERS-2 scatterometer and altimeter data, used to validate and compare to SAR measurements, was given. The performance and limitation of each data set used have been assessed.

The sixth chapter was dedicated to the presentation of an analysis of the features that is possible to extract from SAR images of tropical cyclones. The features extraction was based on the use of wavelet transform.

The seventh chapter was dedicated to the description of the modelling and development of a new technique for the estimation of tropical cyclone intensity. In addition the effect of heavy rain on radar backscatter and on the retrieved wind field was investigated theoretically.

Finally in the eighth chapter an analysis of tropical cyclone using a unique dataset ERS Wave Mode data was detailed. The study proved that the data, acquired globally over the ocean, can be used for tracking and sea state analysis of tropical cyclone in open ocean areas especially where no aircraft or buoys measurements are available.

Concerning the perspectives, the overall work has proved that SAR data, due to their all weather capability and wide swath coverage are of particular interest for the study of tropical cyclones. In particular SAR images can be used to infer information on fine scale storm structure, e.g. eye size, radius of maximum wind speed and rain band structure.

Although C-Band is considered robust against atmospheric disturbances, standard wind field retrieval technique using the scatterometer GMF CMOD5 shows an underestimation in the area of tropical cyclone force winds. This could be explained by the rain contamination and additional effects due to severe sea state that produce a strong damping of NRCS. This leads, for wind speed above 20 *m/s*, to an error in the retrieved wind speed that is up to 30 *m/s* for the cases considered in this study. Improvement could be given by the combined use of SAR with other instrument that can measure rain rate on the same platform.

A new technique to derive the maximum wind speed and the tropical cyclone strength from SAR images has been proposed. The problem of saturation in tropical cyclone wind regime is overcome basing the technique on the combined use of SAR measurements for areas of wind speed of 20 *m/s* or less and a parametric model for tropical cyclone wind speed. The radius of maximum wind speed, required as input, is measured from the SAR image using a technique based on wavelet transform. Wind directions have been computed from the SAR image using spectral analysis to detect the area containing features associated with the wind flow and an interpolation technique. The procedure has been applied to five images of tropical cyclones showing agreement with in situ measurements. Maximum wind speed up to70 m/s can be determined with an RMS error of 3.9 *m/s*. More tropical cyclone images would be required for further validation.

Appendix A

A-1 SAR imaging principles

Radar measurements are based on time delays of the sent signal. The objective of a radar imaging system is to generate a two-dimensional reflectivity map of a scene in the microwave region of the electromagnetic spectrum. A typically radar imaging sensor consists of a transmitting and receiving antenna mounted on a moving platform and oriented parallel to the flight direction (Fig. A-1). The antenna emits consecutively electromagnetic pulses of time duration τ_p to the ground, which are backscattered from different targets. The time difference Δt between the emission and the reception of the pulse is a function of the distance R between the antenna and the target:

$$\Delta t = \frac{2R}{c} \tag{A-1}$$

where c is the speed of light and the factor 2 accounts for the round-trip propagation. The sensor range resolution, i.e.. the minimum spacing between two objects that can be individually detected, is:

$$\Delta r = \frac{c\tau}{2} \approx \frac{c}{2\Delta f} \tag{A-2}$$

where $\Delta f \approx 1/\tau$ is approximately the bandwidth of the pulse. To achieve high resolution in range short pulses are necessary. The reduction of the pulse width leads to a high peak power that is difficult to handle in practice. To circumvent this limitation it is possible to substitute the short pulses by modulated long ones (chirp), provided that they are followed by a processing step (pulse compression).

In the flight or azimuth direction the radar resolution is dictated by the size of the antenna footprint. This latter is dependent on the distance R between the sensor and the scene and the angular resolution of the antenna:

$$\alpha_{ra} = \frac{\lambda}{L} \tag{A-3}$$

where λ is the wavelength of the electromagnetic pulse and L the effective antenna length.

The spatial resolution in azimuth is:

$$\Delta x_{ra} = \alpha_{ra} R = R\frac{\lambda}{L} \tag{A-4}$$

For a uniform antenna illumination, L is coincident with its physical length. To achieve high resolution in azimuth large antennas and short object distances are required. As an example for a satellite sensor that flies with an orbital height of 800 *Km* and an antenna length of 15 *m* the resolution is approximately 3 *Km* and this is not acceptable for most applications.

A Synthetic Aperture Radar overcomes these problems by implementing the synthetic antenna concept: a very large antenna is synthesized by moving a real one of limited dimension along a

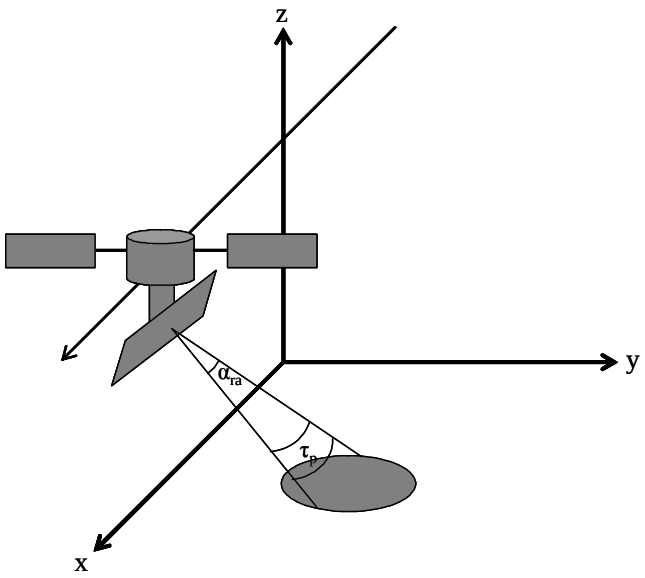

Fig. A-1: SAR acquisition geometry.

reference path. The synthesis is carried out by coherently combining the backscattered echoes received and recorded along the flight path.

The maximum length of the synthesized antenna is equal to the size of the real antenna footprint on the ground at the distance *R*:

$$L_{sa} = \frac{\lambda}{L} R \tag{A-5}$$

The angular resolution of the synthesized antenna is:

$$\alpha_{sa} = \frac{\lambda}{2L_{sa}} \tag{A-6}$$

The azimuth resolution of the synthetic aperture antenna is:

$$\Delta x_{sa} = \alpha_{sa} R = \frac{L}{2} \tag{A-7}$$

The achieved resolution is now completely independent of the range distance and is determined only by the size of the antenna.

A-2 Processing of SAR data

As the imaging processes in the range direction and in the azimuth direction are governed by different time scales, they can in first approximation be treated as independent.

Synthetic aperture radar is of high interest for measuring ocean wave parameters. In principle it is possible to measure ocean wavelength and direction, wave height and near surface wind speed.

Many studies have been conducted on the theory of SAR ocean imaging [Hasselmann et al., 1985] and from all is clear that the radar image is not a direct map of the imaged scene on the ocean surface. The SAR imaging mechanisms is influenced by the modulation of the NRCS and by the wave motions (i.e., by the orbital velocity and acceleration associated with the long waves) [Alpers et al., 1981]. It results in a nonlinear integral transform that describes the mapping of ocean weave spectrum into SAR image variance spectrum, also called Modulation Transfer Function (MTF) [Hasselmann and Hasselmann, 1991]. According to the models described in literature the SAR imaging of ocean waves can be divided in two major processes.

The first one, known as the real aperture radar (RAR) mechanisms, is common to conventional radars which detect the NRCS without synthesized antenna. The second process, that is inherent to only SAR, is known as "Velocity Bouncing". In the following the two processes will be described detailed.

A-2-1 Range processing

Most SAR systems transmit a chirp signal of the form:

$$f_1(t) = exp\left[j\left(\omega t + \frac{\alpha t^2}{2} \right) \right], \quad |t| \le \frac{\tau_p}{2} \tag{A-8}$$

where τ_p is the pulse duration, $\omega = 2\pi f$ is the angular frequency with the carrier frequency f, and α is the chirp rate related to the pulse bandwidth by:

$$\alpha \tau = 2\pi \Delta f \tag{A-9}$$

In Eq. A-8 amplitude is set to 1 as it does not play any role in the subsequent analysis.

The standard reference system used for SAR imaging models is right handed with the platform flying in positive x direction with velocity V (Fig.A-1).

Consider a point target of coordinate $T \equiv (0, y_0, z_0)$; with a distance from the platform equal to R. The signal backscattered by the target and received on board is:

$$f_1(t-\tau) = exp\left[j\,\omega(t-\tau) + j\frac{\alpha}{2}(t-\tau)^2 \right] \tag{A-10}$$

where τ is the time delay between the transmission and the reception of the signal. Assuming that the change of the distance between the target and the antenna is very small (start-stop approximation).

$$\tau = \frac{2R}{c} \tag{A-11}$$

After the baseband conversion we obtain

$$f(t) = exp\left[-j\,\omega\tau + j\frac{\alpha}{2}(t-\tau)^2 \right] \tag{A-12}$$

The subsequent step in the processing of the received signal implies convolution with the (range) reference function:

$$g(t) = exp\left[- j\left(\omega t + \frac{\alpha t^2}{2} \right) \right] \tag{A-13}$$

the impulse response after the convolution is:

$$h(t) \approx \Delta f \exp\left(\frac{4\pi R}{\lambda} \right) \sin c[\pi \Delta f (t - \tau)] \tag{A-14}$$

The last approximation holds near the peak $|t| << \tau_p$ and for large time-bandwidth products ($\Delta f \cdot \tau_p >> 1$).

According to (A-14) a point target is imaged as a distributed object with a range dimension equal to:

$$\Delta r = 0.89 \frac{c}{2\Delta f} \tag{A-15}$$

It corresponds to the distance between the 3 dB points of the impulse response. Δr corresponds to the nominal slant range resolution. Two point target can be resolved only if they are separated by a distance greater than Δr.

A-2-2 Azimuth processing

To investigate the capability of the SAR system to resolve target in the flight direction, let's consider (2N+1) equally spaced positions of the real antenna and a point target $T \equiv (0, y_0, z_0)$, located at the centre of the scene and illuminated by the antenna at positions $S \equiv (x' = n'd, r=0)$ with $n' = -N, \ldots N$ (Fig. A-2). The signal backscattered by the target and received by the antenna at each position $n'd$ is:

$$f(n'd) = \exp\left(- j\omega \frac{2R'}{c} \right) \approx \exp\left[- j\,\omega \frac{2R}{c} - j \frac{2\pi}{\lambda R} (n'd)^2 \right] \tag{A-16}$$

where :

$$R' = \sqrt{R^2 + (n'd)^2} \approx R + \frac{(n'd)^2}{2R} \tag{A-17}$$

The azimuth-dependent part of the return is given by:

$$f(n'd) = \exp\left[- j \frac{2\pi}{\lambda R} (n'd)^2 \right] \tag{A-18}$$

The signal of (A-18) is recorded and then processed to synthesize an antenna of length $2Nd = L_{SA}$.

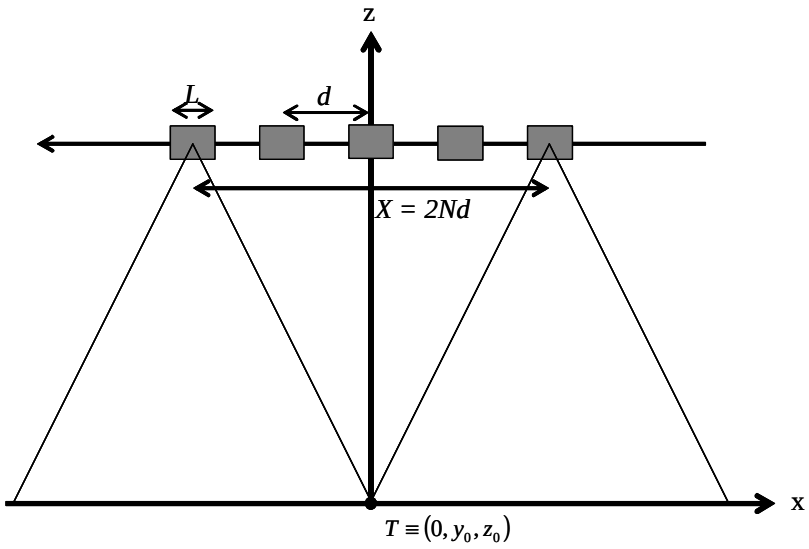

Fig. A-2: Along track acquisition geometry.

The instantaneous frequency of the recorded signal changes linearly as the antenna move along its path. This represents a chirp in the azimuth direction with a negative rate.

The instantaneous Doppler frequency is given by:

$$f(n'd = vt') = \frac{d}{dt'}\left(-\frac{v^2}{\lambda R}t'^2\right) = -\frac{2v^2}{\lambda R}t' \tag{A-19}$$

$$-\frac{\lambda r}{2Lv} \le t' \le \frac{\lambda r}{2Lv}$$

Similar to the range compression step the azimuth processing is done by a discrete correlation with a reference chirp:

$$g\left(n'd\right) = \exp\left[j\frac{2\pi}{\lambda R}\left(n'd\right)^2 \right] \tag{A-20}$$

Considering $n'd << X$ the result after the correlation is:

$$\hat{f}\left(n'd\right) \approx sinc\left(\frac{2\pi}{L}n'd\right) = sinc\left(\frac{\pi}{\Delta x}n'd\right) \tag{A- 21}$$

with

$$\Delta x = \frac{L}{2} \tag{A-22}$$

the synthetic aperture radar azimuth resolution.

A-3 SAR modulation transfer function

In the range of small to moderate incidence angles (between 20° and 60°) the radar backscattered field from the sea surface can be obtained from Kirchhoff's integral by applying the Bragg resonance theory. According to this theory the NRCS of the sea surface is proportional to the sum of the ripple variance spectra at the Bragg wave numbers

$$K_b == \pm K_0 \sin\theta \qquad \text{(A-23)}$$

where K_0 is the wave number.

The modulation of the NRCS by the long ocean waves (longer than twice the SAR resolution cell) is caused by two effects: the tilt modulation and the hydrodynamic modulation.

The tilt modulation can be explained by a geometric effect, i.e. the small scale roughness (Bragg resonant waves) is seen by the radar at different incidence angles depending on the location on the long waves [Alpers et al., 1981].

The non uniform distribution of the short waves with respect to the long ocean waves (Fig. A-4), due to interactions between the short and long waves, is responsible for the hydrodynamic modulation [Hasselmann and Hasselmann, 1991].

In the case of SAR, in addition to the tilt and hydrodynamic modulations of NRCS, the orbital motions of the water particles due to the long ocean surface waves must be accounted. In particular this effect, also known as "Velocity Bunching" can lead to the formation of wave-like patterns in SAR images even for a uniform NRCS.

As SAR finds the location of a target in the azimuth directions using Doppler coordinate; a target with a velocity component in the direction of the radar will introduce a Doppler shift and so a shift of the detected position. The sea surface model used to describe the SAR response is represented by moving facets, having dimensions that are large compared to the radar wavelength but small compared to the radar resolution cell. The motion of these facets is due to the orbital motion associated with the long surface waves. This motion, which is spatially variable, leads to an alternating concentration and spreading of the position of the facets in the image plane, and so to a wavelike pattern in the SAR image.

Fig. A-4 shows the contributions to the modulation transfer function of the three mechanisms described above versus the direction of propagation of the waves respect to the radar.

Velocity bouncing vanishes for range traveling waves. At the same time the tilt modulation and the hydrodynamic modulation are maximum. Range traveling waves are imaged best by SAR. For waves traveling in other direction the influence of velocity bouncing can be strong, leading to severe distortion in the imaged wave field.

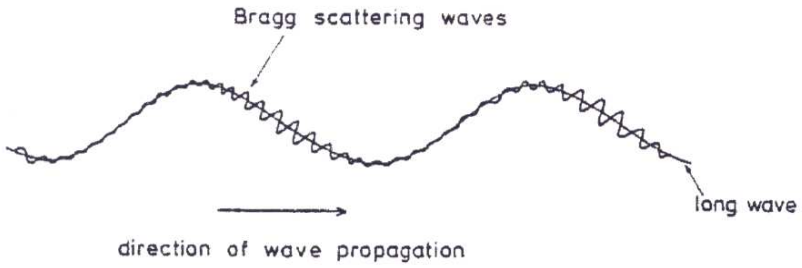

Fig. A-3: Asymmetric distribution of Bragg waves on a long wave due hydrodynamic modulation (adapted from Alpers et al. 1981, Fig.2 pp. 6485).

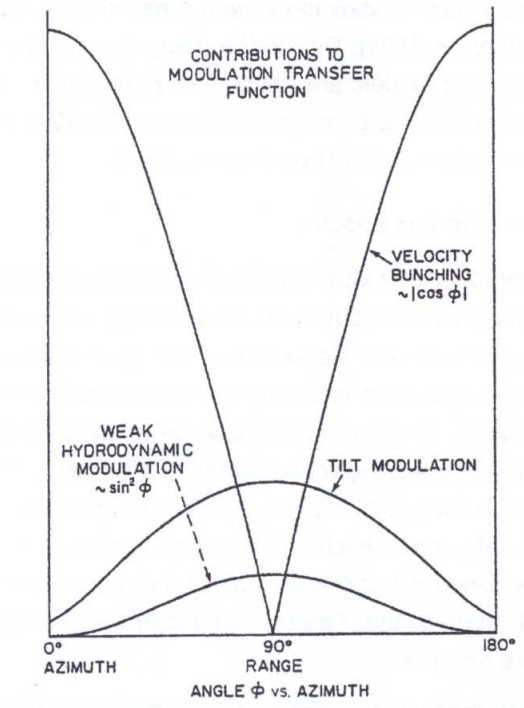

Fig. A-4: Contribution of the tilt modulation, hydrodynamic modulation and velocity bouncing to the SAR modulation transfer function for different wave direction with respect to the antenna (after Alpers et al. 1981, Fig.6 , pp 6489).

References

Alpers W., Ross D.B. and Rufenach C.L., 1981. On the Detectability of Ocean Surface Waves by Real and Synthetic Aperture Radar. *Journal of Geophys. Res*., vol. 86, pp. 648 1-6498.

Franceschetti G., Lanari R., 1999. Synthetic Aperture Radar Processing. *CRC Press*, Boca Raton, Fla.

Hasselmann K., Raney R.K., Plant W.J., Alpers W., Shuchman R.A., Lyzenga D.R., Rufenach C.L., Tucker M.J., 1985. Theory of Synthetic Aperture Radar Ocean Imaging: A MARSEN View. *Journal of Geophys. Res.*, vol. 90, pp. 4659-4685.

Hasselmann K. and Hasselmann S., 1991. On the nonlinear mapping of an ocean wave spectrum into a Synthetic Aperture Radar image spectrum and its inversion. *Journal of Geophys. Res.*, vol. 96, pp. 1071 3- 10729.

Robinson I. S., 2004. Measuring the Oceans from Space: The principles and methods of satellite oceanography. *Springer*.

Ulaby F.T.; Moore R. K., Fung A.K., 1986. Microwave Remote Sensing: Active and Passive, Volume II: Radar Remote Sensing and Surface Scattering and Emission Theory. *Artech House*.

Acknowledgments

I dedicate this thesis to my wife,

Fifame,

For encouraging,

And for supporting me,

I would also like to acknowledge the people contributed to the success of my Ph.D.

I cannot find words to express gratitude to my supervisors Prof. Hartmut Graßl and Dr. Susanne Lehner; this thesis would not have been possible without their help and support. I would like to thank Susanne for welcoming me at German Aerospace Centre (DLR), for her dedicated supervision and guidance during my Ph.D. Thanks to her support, attention to detail, hard work, I learned a lot about the subject.

I would like to express my deep gratitude to Dr. Johannes Shulz-Stellenfleth whose advices and insight was invaluable to me. His knowledge of the SAR technologies and our discussions have been a great source of inspiration.

The four years spent at DLR has been the occasion to meet marvelous people. I would like to thank and express my friendship to my colleagues Stephan Brusch, Xiao Ming Li and to the whole Marine Remote Sensing group of DLR for all the help and discussions.

It is a pleasure to thank Dr. Chan-Su Yang and the Korea Ocean Research & Development Institute for their warm welcoming, our collaboration had added value to my studies. The month I have spent in Korea in their Department have been a great experience.

I would also like to express my deepest gratitude to Mrs. Christine Fluche; her help for solving all administrative issues has also made this thesis possible.

Last but not least, I would like to thank my parents for their unconditional support.

The last lines go to all the people, who one way or another contributed to the success of this work….